UiO : Department of Physics
University of Oslo

Structural- and Compositional Investigations of Grain Boundaries in Y-Doped $BaZrO_3$

A proton-conducting electrolyte for electrochemical applications

Adrian Lervik

Master's Thesis, Spring 2016

Acknowledgements

This thesis is submitted as part of the master's degree in Materials Science and Nanotechnology. The experimental work has been performed in the two research groups: Structure Physics (Strukturfysikk) and Solid State Electrochemistry (FAstStoff Elektrokjemi (FASE)) from August 2014 to May 2016.
I would like to give thanks to my three supervisors: Anette E. Gunnæs, Reidar Haugsrud and Spyros Diplas for their guidance and motivation through the years and for all their help at the very end. Furthermore, Phuong D.Nguyen, Tor S. Bjørheim, Nahum M. Carcases, Øystein Prytz, Sandeep Gorantla and Truls Norby are thanked for all their teaching, and for all the helpful discussions. I am grateful to all the other members associated with the two groups for showing interest in my thesis and providing the best possible environment; both scientifically and socially.
A special thank is attributed to Akihide Kuwabara whom helped me out during my stay at Japan Fine Ceramics Center (JFCC) in Nagoya, Japan. The Scandinavia-Japan Sasakawa Foundation (SJSF) and FASE are gratefully acknowledged for their financial support for this trip; a trip not realizable without.
I would not have been in the position to write this had it not been for the fantastic people I started studying with 5 years ago. MENA gang of 2011: it has been an absolute pleasure.
A special thank is given to Simen N. H. Eliassen and Sebastian Gutterød for being my regular coffee mates nearly every single day for the last two years.
Thanks to my parents; Angenie and Øystein, and my brother Kevin, for their motivation and support in every decision I have ever made.
Last, but not least: to my dear Athenna for her everlasting support.

Adrian Lervik
15. May 2016
University of Oslo

Abstract

Proton-conducting electrolytes are candidates for a range of electrochemical applications. The search for one which may operate in the intermediate temperature range of 400-800 °C has been ongoing for a while, and Yttrium-doped $BaZrO_3$ (BZY) have been established as one of the most promising materials. Unfortunately, its highly refractory nature makes processing difficult, and generally results in a small grained polycrystalline material with high areas of highly resistive grain boundaries. The cause of resistive grain boundaries is attributed to the formation of space-charge layers, where negatively charged defects segregate close to the grain boundaries in order to compensate the positively charged grain boundary core.

A sample prepared unconventionally using extreme temperatures of 2200 °C overcame the grain boundary problem, but an unanswered question is: *what did occur during the high temperature treatment*?

In this thesis, conventional samples were prepared by the Solid State Reaction (SSR) method and characterised by a range of methods. X-Ray Diffraction (XRD) indicates the presence of two cubic phases with slightly different lattice parameters, and X-ray Photoelectron Spectorscopy (XPS) shows Y situated two different chemical states with a seperation of $\sim$2.6 eV. Energy Dispersive Spectroscopy (EDS) performed in the Transmission Electron Microscope (TEM) shows an enrichment of Y and depletion of Ba at the grain boundaries. These are strong indications that Y also substitutes on Ba site in the structure. The microstructure has grains of $\sim$600 nm and the grain boundaries mostly adapt random configurations. Conductivity measurements by impedance spectroscopy indicates the presence of highly resistive grain boundaries, as the conductivity of grain boundaries is three orders of magnitude lower than that of bulk (10^{-3} vs. 10^{-6} Scm^{-1} at 400 °C in wet O_2). In the high temperature sample the same degree of Ba depletion is not observed, but Y also segregates to the grain boundaries. The grain boundaries are also more frequently near a Coincident Site Lattice (CSL) type grain boundary; an indication of grain boundary migration during the high temperature treatment.

Furthermore, two samples prepared through the Solid State Reactive Sintering (SSRS) method, with Ba non-stoichiometry ($x = \pm 0.02$, in $Ba_xY_{0.15}Zr_{0.75}O_{3-\delta}$), have been stud-

ied by TEM. The goal was to gain more understanding on how the addition of small amounts of NiO assists in the sintering stage, and how it is distributed in the resulting sample. The results shows that Ni rich phase(s) are present at the grain boundaries and triple points in the Ba rich sample. In the Ba deficient sample no secondary phases are observed, but the Ni content is found to be twice as high at the grain boundaries as in the grain interior (bulk).

Acronyms

ABF Annular Bright Field.

ADF Annular Dark Field.

BZY Yttrium-doped $BaZrO_3$.

CCD Charge Coupled Device.

CPE Constant Phase Element.

CSL Coincident Site Lattice.

CTE Coefficient of Thermal Expansion.

DFT Density Functional Theory.

DOS Density Of States.

EBSD Electron Backscatter Diffraction.

EDS Energy-Dispersive Spectroscopy.

EELS Electron Energy-Loss Spectroscopy.

ELNES Electron Energy-Loss Near-Edge Structure.

EXAFS X-ray Absorption Fine Structure.

FFT Fast Fourier Transform.

GB Grain Boundary.

GBCD Grain Boundary Character Distribution.

GGA Generalized-Gradient Approximation.

GPA Geometric Phase Analysis.

HAADF High-Angle Annular Dark Field.

HRTEM High-Resolution TEM.

IMFP Inelastic Mean Free Path.

MCFC Molten Carbonate Fuel Cells.

OECD Organisation for Economic Co-operation and Development.

OLM Orientation Imaging Microscopy™.

PAW Projector-Augmented Wave.

PC-SOFC Proton-Conducting Solid Oxide Fuel Cells.

PCFC Proton-Conducting Fuel Cell.

PEMFC Polymer Electrolyte Membrane Fuel Cell.

SAD Selected Area Diffraction.

SADP Selected Area Diffraction Pattern.

SEM Scanning Electron Microscopy.

SOFC Solid Oxide Fuel Cell.

SPS Spark Plasma Sintering.

SSR Solid State Reaction.

SSRS Solid State Reactive Sintering.

STEM Scanning Transmission Electron Microscopy.

TEM Transmission Electron Microscopy.

VASP Vienna Ab-initio Simulation Package.

VBM Valence Band Maximum.

XPS X-ray Photoelectron Spectroscopy.

XRD X-Ray Diffraction.

ZA Zone Axis.

Contents

Acknowledgements **i**

Abstract **iv**

Acronyms **v**

1 Introduction **1**
1.1 Fuel cells 1
1.1.1 Types of fuel cells 3
1.1.2 Electrolyte properties 3
1.2 Protons in solid oxides 4
1.3 Master thesis' aim and focus 4

2 Theory **5**
2.1 Crystallography 5
2.1.1 Reciprocal space 5
2.1.2 Planes and directions 6
2.1.3 Perovskites 6
2.1.4 Grain boundaries 8
2.2 Scattering and diffraction 10
2.2.1 Laue conditions and Bragg's law 10
2.2.2 Dynamic and kinematic conditions 11
2.2.3 Structure factor 12
2.3 Defect chemistry 12
2.3.1 Defects in $BaZrO_3$ 13
2.3.2 Defect concentration as function of partial pressures 15
2.4 Space-charge 17
2.4.1 Electrochemical potential 18
2.5 Electrical conductivity 20

2.5.1 Transport in electrical fields . . . 20
2.5.2 Mobility of protonic defects . . . 21
2.6 Impedance spectroscopy . . . 22
2.6.1 Alternating current and impedance . . . 22
2.6.2 Passive circuit elements . . . 22
2.6.3 Impedance sweeps . . . 24
2.6.4 Brick-layer model . . . 24
2.7 Quantum mechanical modelling . . . 26
2.7.1 The many-particle problem . . . 26
2.7.2 Density functional theory . . . 27
2.8 Transmission Electron Microscopy (TEM) . . . 29
2.8.1 Instrument . . . 30
2.8.2 Interactions . . . 31
2.8.3 Experimental techniques . . . 31

3 Literature **35**
3.1 Background . . . 35
3.2 Synthesis . . . 36
3.2.1 Different methods and sintering conditions . . . 36
3.2.2 The effect of sintering aids . . . 38
3.3 Grain boundaries . . . 39
3.3.1 Measurements . . . 39
3.3.2 Transmission Electron Microscopy (TEM) . . . 42
3.4 Computational results . . . 42

4 Experimental methods **45**
4.1 Samples . . . 45
4.1.1 Preparation of BZY10 . . . 45
4.2 X-Ray Diffraction (XRD) . . . 46
4.3 Scanning Electron Microscopy (SEM) . . . 46
4.3.1 Electron Backscatter Diffraction (EBSD) . . . 47
4.3.2 Density and grain size evaluation . . . 47
4.4 Transmission Electron Microscopy (TEM) . . . 48
4.4.1 Sample preparation . . . 48
4.4.2 Goniometer tilt angle . . . 48
4.4.3 Energy-Dispersive Spectroscopy (EDS) . . . 49
4.5 Electrical measurements . . . 49
4.5.1 Setup . . . 49

4.5.2 Sample preparation 50
4.5.3 Experimental 50
4.5.4 Data normalization 51
4.6 X-ray Photoelectron Spectroscopy (XPS) 51
4.6.1 Sample preparation 51
4.6.2 Peak fitting 51
4.7 Systematic errors 52

5 Computational method **53**
5.1 Modelling of defects in solid materials 54
5.1.1 Errors and limitations 55

6 Results **57**
6.1 Phase analysis 57
6.2 Morphology and microstructure 60
6.2.1 Grain characteristics 60
6.2.2 Grain orientation 62
6.3 Analytical TEM investigation of grain boundaries 63
6.3.1 BZY10-2 64
6.3.2 BZY10-HT 70
6.3.3 BZY15+NiO 71
6.4 Compositional study by XPS 74
6.5 Conductivity 77
6.5.1 Space-charge calculations 78
6.6 Computational results 80
6.6.1 Defects in $BaZrO_3$ 80
6.6.2 The grain boundary 82

7 Discussion **87**
7.1 Samples prepared by SSR 87
7.2 Comparison between low- and high temperature treatment 90
7.2.1 Composition 90
7.2.2 Microstructure 90
7.2.3 Orientation of grain boundary's influence on core potentials . . 92
7.2.4 Validity of the Mott-Schottky approximation 92
7.3 Samples prepared with NiO additive 94
7.4 Further work 95

7.4.1 Electron Energy Loss Spectroscopy (EELS) 95
7.4.2 Electron holography 95
7.4.3 Enviromental TEM experiments 96

8 Conclusion **97**

List of References **99**

A Brouwer diagrams **109**
A.1 Defect concentration vs. pO_2 109
A.2 Defect concentration vs pH_2O 112

B EDS quantification **113**

C Rietveld refinement **115**

D EELS spectra **117**

E Initial impedance results **119**

Chapter 1

Introduction

In our modern society, a vast amount of energy is used every day to make our life more convenient. Most of this energy stems from carbon-intensive fossil fuels, which are prime sources of global warming. At the same time the world's energy consumption is rising exponentially, and has done so for the last half a century. The industrial and economic growth of countries outside Organisation for Economic Co-operation and Development (OECD), such as China and India among others, has a higher increase in energy consumption than the OECD countries [1, 2]. This, together with the ever increasing world population, has presented a major challenge to mankind: to produce sufficient amounts of energy without the emission of greenhouse gasses. Much research is thus turned towards renewable energy systems in which hydrogen serves as the energy carrier. In this "hydrogen society" energy harnessed from photovoltaic elements, or other sources of renewable energy, is utilized in *electrolysis* to split water into oxygen and hydrogen. The hydrogen can be stored, and may later be fed to a fuel cell which turns the chemical energy back into electrical energy. All stages have their challenges and are today subject to extensive research.

1.1 Fuel cells

A fuel cell is a device in which chemical energy from a fuel is converted into electrical energy. In comparison to common combustion engines, where the chemical energy is released as heat to cause a gas to expand, fuel cells converts chemical energy directly to electrical energy. This section will present the basic concept of a fuel cell by describing the case where hydrogen is used as fuel. A schematic model is shown in figure 1.1, where the following equations relates to the Proton-Conducting Fuel Cell (PCFC) and Polymer Electrolyte Membrane Fuel Cell (PEMFC). Hydrogen gas is the fuel and is

supplied at the anode where it is oxidized according to:

$$\mathrm{H_2(g)} \longrightarrow 2\mathrm{H^+} + 2\mathrm{e^-}. \tag{1.1}$$

The electrons generated in this reaction flow through an outer electrical circuit, through a load, and then to the cathode. Here oxygen is supplied and reduced to oxide ions according to:

$$\frac{1}{2}\,\mathrm{O_2(g)} + 2\,\mathrm{e^-} \longrightarrow \mathrm{O^{2-}}. \tag{1.2}$$

When the protons from equation (1.1) permeate the electrolyte and reach the cathode, a water forming reaction takes place:

$$2\,\mathrm{H^+} + \mathrm{O^{2-}} \longrightarrow \mathrm{H_2O(g)}. \tag{1.3}$$

Electrical energy has been produced by the chemical energy of hydrogen. The "waste" in this fuel cell is water.

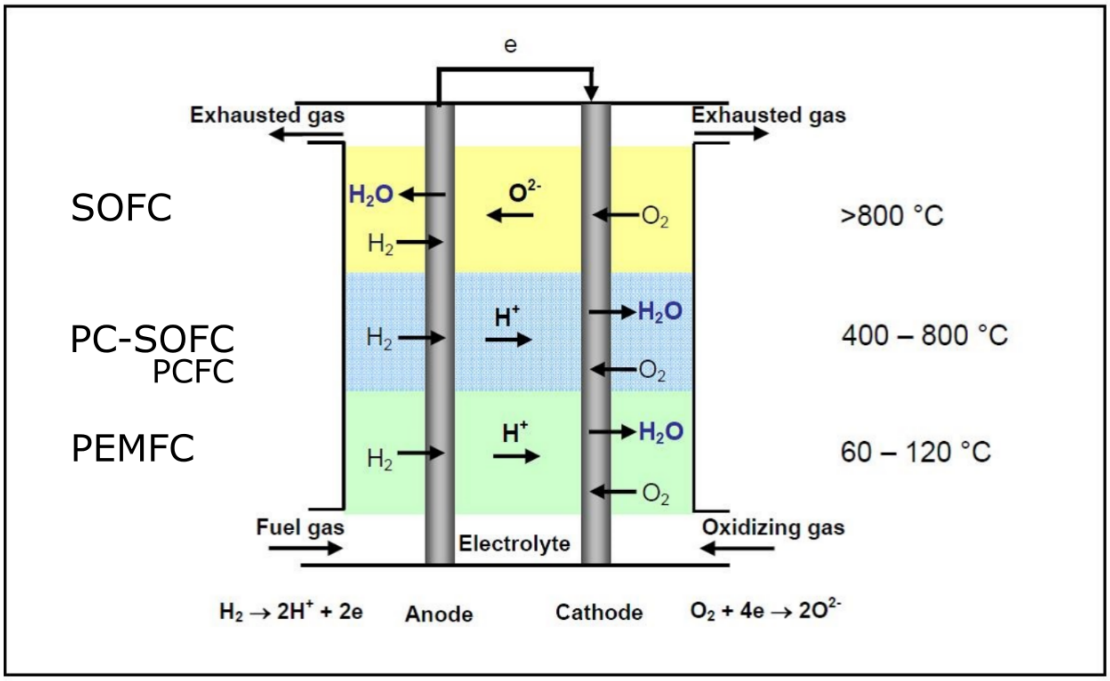

Figure 1.1: Comparison between the operational principles of SOFC, PCFC and PEMFC. The figure is modified from [3].

1.1.1 Types of fuel cells

A common way to classify fuel cells is based on their operating temperatures. The low-temperature fuel cells are typically in the range of 50-200 °C and here the PEMFC and fuel cells in which the electrolyte is a liquid solution of alkaline salts or phosphoric acid are found. Low-temperature fuel cells has the advantage in start-up times and are of interest for portable power generation. However, at these temperatures the kinetics of the reactions taking place at the electrodes are limited, and thus requires the use of catalytic materials such as platinum. High-temperature fuel cells do not require the same amount of catalytic assistance, but at temperatures above 800 °C, the limitations are bound by the materials. Differences in the Coefficient of Thermal Expansion (CTE) may cause damage to the cell when the temperature is changed. Other issues are long start-up times and risk of reaction between component materials [4]. In this region the Solid Oxide Fuel Cell (SOFC), in which the electrolyte is a solid oxide material, and the Molten Carbonate Fuel Cells (MCFC) are found.
Due to the limitations of high- and low-temperature fuel cells, there is, and has been for a while, an ongoing search for fuel cells which can operate in the intermediate temperature region of 400-800 °C. Proton-Conducting Solid Oxide Fuel Cells (PC-SOFC), also referred to as PCFC, show great promise here, but now the total ionic conduction is dominated by protons and not oxide ions as in the high-temperature case. An advantage of this is that water vapour, which threatens the stability of the anode and dilutes the fuel, is not formed on the anode side. This may be seen from figure 1.1. For PCFC, the water is formed on the cathode, and swept away by a high air flow [5]. Many promising electrolytes for PCFC have been reported in literature and often taking the *perovskite* type structure. One of them is Barium Zirconate ($BaZrO_3$), the material of interest in this study.

1.1.2 Electrolyte properties

The electrolyte has a large impact on the fuel cell's overall performance and therefore has some required properties. Firstly, it must be dense enough to prevent reactant diffusion. Its total ionic transport number should be 0.99, meaning that 99% charge carriers are ionic species, which prevents electron migration and short circuiting. The total ionic conductivity under operating conditions should be higher than 10^{-2} Scm^{-1} [4, 6]. Furthermore, the electrolyte must be chemically, thermodynamically and mechanically stable in both oxidizing and reducing conditions. Solid oxide materials often exhibit high ionic conductivity, high chemical stability and have low electronic conductivity [7].

1.2 Protons in solid oxides

In the 1980s, Iwahara and co-workers first observed and reported proton conductivity in: Strontium Cerate ($SrCeO_3$) and Barium Cerate ($BaCeO_3$), after acceptor doping and exposing the material to a hydrogen containing atmosphere [8]. They also prepared and studied zirconates based on $CaZrO_3$ and $SrZrO_3$. After more than 30 years, acceptor doped cerates and zirconates have become well established as proton conductors. Today, $BaCeO_3$ and $BaZrO_3$ remain as two state-of-the-art materials since they exhibit high values of total proton conductivity. However, the experimentally achieved values are lower than what earlier theory predicted [9]. The main reason for this is high Grain Boundary (GB) resistance in acceptor doped $BaZrO_3$ compounds, which is associated with the formation of *space-charge* layers at the very first nanometeters surrounding the grain boundary core. Only one reported sample has overcome the high grain boundary resistance and was prepared by Sophie Duval [10]. The nature of why this sample has different functional properties than conventionally prepared samples remains unknown, but has been attributed to changes at the very interface of the grain boundaries after the extreme temperature treatment at 2200 °C.

1.3 Master thesis' aim and focus

In this thesis the unconventionally prepared sample by Sophie Duval will be compared with samples by more conventional routes, in order to gain more understanding of what occurred at the grain boundaries during the extreme temperature treatment. Samples are to be prepared in-house, characterised using X-Ray Diffraction (XRD) and the proton conductivity measured by electrochemical impedance spectroscopy. Microstructural properties will be studied using analytic Transmission Electron Microscopy (TEM), in combination with X-ray Photoelectron Spectroscopy (XPS) and first-principle calculations. The goal is to find systematic differences in structure and composition in grain boundaries and in their vicinity. The use of microscopic and spectroscopic techniques will yield quantitative information on what is accumulating in, and close to, the grain boundaries. Furthermore, two samples prepared using a slightly different synthesis route with NiO as sintering aid will be studied using TEM with the aim to understand how Ni assist in sintering and how it distributes within the samples.

Chapter 2

Theory

This section is dedicated to establishing the theoretical background and the notation used in this thesis.

2.1 Crystallography

In a crystalline material the *crystal basis* defines its long range order. The basis is connected to lattice points in an array of discrete, but infinite, regular arrangement of points in a vector space. A crystal is described by one of the 14 *Bravais lattices*, which together with the basis defines what is called the *unit cell*. This represents the smallest "building block" of the crystal. A lattice vector is described as:

$$\mathbf{R} = n_1\mathbf{a_1} + n_2\mathbf{a_2} + n_3\mathbf{a_3}, \tag{2.1}$$

where n_i are integers and $\mathbf{a}, \mathbf{b}$ and $\mathbf{c}$ are lattice vectors.
The symmetry properties of a crystal are described through inversion, mirror plane, rotation, screw axis and glide plane, where the two latter include translation. These five symmetry operations combined with the Bravais lattices, generates the 230 crystallographic space groups.

2.1.1 Reciprocal space

When working with diffraction and quantum mechanical modelling, it is common to utilize the concept of the reciprocal lattice. This is a mathematical construction of the real crystal in the reciprocal space. The reciprocal lattice vector is defined from the following relation:

$$\mathrm{e}^{i\mathbf{R}\cdot\mathbf{g}} = 1, \tag{2.2}$$

where **g** is the reciprocal lattice vector, given as:

$$\mathbf{g} = h\mathbf{b_1} + k\mathbf{b_2} + l\mathbf{b_3}. \tag{2.3}$$

Here *h*, *k* and *l* are integers called *Miller Indices*. The reciprocal vectors are defined from the real space vectors by:

$$\mathbf{b}_1 = 2\pi\frac{\mathbf{a_2} \times \mathbf{a_3}}{\Omega}, \qquad \mathbf{b}_2 = 2\pi\frac{\mathbf{a_3} \times \mathbf{a_1}}{\Omega}, \qquad \mathbf{b}_3 = 2\pi\frac{\mathbf{a_1} \times \mathbf{a_2}}{\Omega}, \tag{2.4}$$

where Ω is the volume of the unit cell, given as: $\Omega = \mathbf{a}_1 \cdot (\mathbf{a}_2 \times \mathbf{a}_3)$. In crystallography the reciprocal vectors are commonly labelled as $\mathbf{a_i^\star}$, whilst here the solid state physics notation is used.
Furthermore, the following relation between the vectors exist:

$$\mathbf{a}_i \cdot \mathbf{b}_j = 2\pi\delta_{ij}. \tag{2.5}$$

Here δ_{ij} is the Kronecker delta which is 1 if $i = j$, and 0 otherwise.
In quantum mechanical modelling, the reciprocal vector is viewed upon as wave vectors that yield plane waves with the periodicity of the Bravais lattice. This is written as:

$$\mathrm{e}^{i\mathbf{g}\cdot\mathbf{r}} = \mathrm{e}^{i\mathbf{g}\cdot\mathbf{r}}\mathrm{e}^{\mathrm{i}\mathbf{g}\cdot\mathbf{R}} = \mathrm{e}^{i\mathbf{g}\cdot(\mathbf{r}+\mathbf{R})}, \tag{2.6}$$

where **r** is the position vector of an atom in the unit cell.

2.1.2 Planes and directions

Miller indices represent lattice points in the reciprocal lattice, which corresponds to a plane in real space. A real space lattice plane is written as (*hkl*) where *h*, *k* and *l* corresponds to the intersect with the unit cell axis **a**, **b** and **c** at positions 1/*h*, 1/*k* and 1/*l* respectively. If a plane does not intersect with the axis, it is labelled "0". Sets of equivalent planes is written as {*hkl*}. Similarly, a direction in a crystal is written as [*uvw*] and equivalent directions as ⟨uvw⟩. The direction which is orthogonal to the normal of all the planes is termed the Zone Axis (ZA).

2.1.3 Perovskites

Ideal perovskite structures have the general formula ABO_3. It may be described by a 12 coordinated A-site cation, surrounded by corner sharing BO_6 octahedrons. A schematic view is given by figure 2.1. The A-site cation generally has a larger ionic radius than

the B-site cation, and has a +2 valence. The B-site cation is usually a transition metal or rare earth metal with a +4 valence. Many minerals take the perovskite structure due to its tolerance for different sizes of A and B cations. In its ideal form, perovskites are cubic and described with the $Pm\bar{3}m$ (221) space group. If the BO_6 octahedral is rotated, the cubic symmetry is reduced to trigonal or orthorhombic with space groups Pnma (62) and $R\bar{3}c$ (167), respectively.

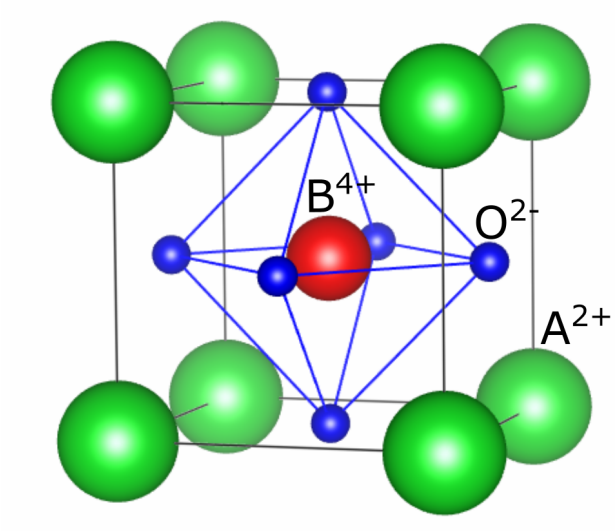

Figure 2.1: Unit cell of the cubic Perovskite (ABO_3) structure. Green, red and blue corresponds to the A-site cations, B-site cation and oxygen ions, respectively. This figure, and all other atomic visualisations are made using [11].

The *Goldsmith tolerance factor* is used to predict lattice distortion in perovskites by considering the symmetry of the crystal with respect to the ionic radii. The following equation is applied:

$$t = \frac{r_a + r_X}{\sqrt{2}(r_b + r_X)}, \tag{2.7}$$

where r_A, r_B and r_X are the ionic radii of atom A, B and X in an ABX_3 structure. Stable perovskite type structures are usually obtained when the tolerance factor ranges between 0.75 and 1.0. Cubic symmetry is observed for $0.90 < t < 1.04$, while structures with tolerance factor within 0.75-0.90 usually adapt an orthorhombic symmetry [4]. In $BaCeO_3$ the tolerance factor is t = 0.94, and the unit cell is orthorhombic. Undoped $BaZrO_3$, has t = 1.004 and is cubic, indicating a good match between Zr^{4+} and Ba^{2+}. However, introducing various amounts of Y^{3+} with an effective ionic radii 0.9 Å vs. 0.72 Å for Zr, will introduce lattice distortion to some extent, and often towards a slight tetragonal behaviour as observed through high-resolution XRD and X-ray Absorption Fine Structure (EXAFS) [12].

2.1.4 Grain boundaries

A grain boundary in a crystalline material is a region separating two crystals (grains) which differ in mutual orientations. The grain boundary represents a transition region in which atoms may be displaced relative to their regular sites. A grain boundary between materials of the same phase is referred to as a *homophase* boundary, whilst a boundary between different phases is simply called a *phase-*, *interphase-* or *heterophase* boundary. These interfaces represent a crystallographic and/or chemical discontinuity with a width of less than two atomic diameters, but may in some cases extend to several atomic diameters [13].
Generally a grain boundary may be defined by three macroscopic- and two microscopic degrees of freedom. The macroscopic ones specify the mutual misorientation of the adjoining grains A and B, represented by the rotation required to bring both grains into a perfect match. By separating them based on their relationship among individual degrees of freedom, e.g. the relationship between the rotation axis and the grain boundary normal, as shown schematically in figure 2.2, one gets the two definitions:

1. *Tilt boundaries*: where ($\boldsymbol{o} \perp \boldsymbol{n}$)
2. *Twist boundaries*: where ($\boldsymbol{o} \parallel \boldsymbol{n}$)

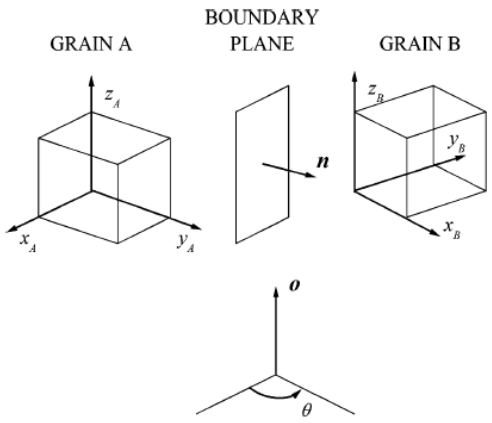

Figure 2.2: Variables defining the GB. x_i, y_i and z_i are the axes parallel to the crystallographic direction in grains *A* and *B*. *o* is the rotation axis and θ is the tilt angle required to bring the grains into identical positions. *n* determines the orientation of the grain boundary plane. Figure reproduces from [13].

This was summarized by Wolf & Lutsko, by considering the relationship between the Miller indices of both contacting planes in a bicrystal and the twist angle, φ [14].

Table 2.1: Categorization of grain boundaries as proposed by Wolf & and Lutsko. $(h_i k_i l_i)$ is the contacting plane in grains 1 and 2, and φ is the twist angle.

Symmetric tilt grain boundary	$\{h_1k_1l_1\} = \{h_2k_2l_2\}$ & $\varphi = 0$
Asymmetric tilt grain boundary	$\{h_1k_1l_1\} \neq \{h_2k_2l_2\}$ & $\varphi = 0$
Twist grain boundary	$\{h_1k_1l_1\} = \{h_2k_2l_2\}$ & $\varphi \neq 0$
Random (mixed) grain boundary	$\{h_1k_1l_1\} \neq \{h_2k_2l_2\}$ & $\varphi \neq 0$

If the boundary plane represents the plane of the mirror symmetry of the crystal lattices of two grains, it is described by the same Miller indices from the point of view of both grains. This is then a *symmetric* boundary and if not; it is called *asymmetric*. The orientation of the grain boundary between the misoriented grains is described by the normal $\boldsymbol{n}$ to the grain boundary plane. This gives the following notation for the case of tilt boundaries:

$$\theta^{\circ}[h_o k_o l_o], (h_{nA} k_{nA} l_{nA})/(h_{nB} k_{nB} l_{nB}). \tag{2.8}$$

If the grain boundary does not fit to any of these, it belongs to a class called *random* or *mixed* boundaries, in which one has to find the tilt and twist components individually.
The two microscopic degrees of freedom describes the rigid body translation, $\mathbf{T}$, of the grains relative to each other, both parallel and perpendicular. The latter is then naturally the volume expansion. However, this vector is independent of the macroscopic degrees of freedom and is affected of equilibrium structure under external conditions such as temperature, pressure and chemical compositions and thus not considered as independent degrees of freedom.

Crystallography of grain boundaries

The preceding section explained the grain relation to one another, but gave no indication of how atoms are situated in the grain boundary core. In earlier models, it was assumed that the grain boundary was amorphous regions. However, today's models describe grain boundaries as crystal-like structures. It is normal to distinguish between *low-angle* and *high-angle* grain boundaries, where the primer has a low misorientation angle θ (< 15°) and usually exhibits dislocations.

The coincident site lattice

There are many ways to describe high-angle grain boundaries, but most commonly the Coincident Site Lattice (CSL) is applied, as proposed by Kronberg & Wilson in 1949 [15]. The assumption is that the grain boundary energy is lowest when the degree of coinciding atom positions in both grains is high, since the minimum in Gibbs energy

corresponds to a state of perfect arrangement. Thus a high number of coinciding sites should be more thermodynamically stable than grain boundaries with perturbed structural configurations.
Assuming two grains are misoriented by an angle θ around the axis $\boldsymbol{o}$, the superposition of atoms from both grains are the *coincidence sites*, defined as:

$$\Sigma = \frac{\text{number of coincidence sites in an elementary cell}}{\text{total number of all lattice sites in an elementary cell}}. \tag{2.9}$$

In cubic systems this may be determined directly from the Miller indices of the symmetrical tilt boundary plane as:

$$\Sigma = \delta(h^2 + k^2 + l^2), \tag{2.10}$$

where δ is either 1 or $1/2$ if $(h^2 + k^2 + l^2)$ is odd or even, respectively. This since in cubic systems all Σ values are odd.

2.2 Scattering and diffraction

Most of this section is from references [16, 17]. The reader is encouraged to read these books for a full understanding, since only the essential (and most basic) concepts are presented here.
Scattering is the process where an electron interacts with matter and deviates from its original trajectory. The scattering process may occur either elastically (no transfer of energy) or inelastically (transfer of energy). *Diffraction* is the term given to the case of coherent scattering by groups of atoms. For diffraction the phase relation between each scattered wavelet causes either constructive or destructive interference at specific angles.

2.2.1 Laue conditions and Bragg's law

In 1912, Max von Laue discovered that diffraction from crystals may only occur under a set of conditions called the *Laue conditions*. It states that diffraction may occur when $\Delta\mathbf{k}$ is equal to a vector in the reciprocal lattice.

$$\Delta\mathbf{k} = \mathbf{g} \tag{2.11}$$

Here $\mathbf{g}$ is an an arbitrary reciprocal lattice vector, as defined by equation (2.3), and $\Delta\mathbf{k} = \mathbf{k}_\mathrm{f} - \mathbf{k}_\mathrm{i}$ is the wavevector transfer from the incoming and final wavevector $\mathbf{k}_\mathrm{i}$ and $\mathbf{k}_\mathrm{f}$, respectively.

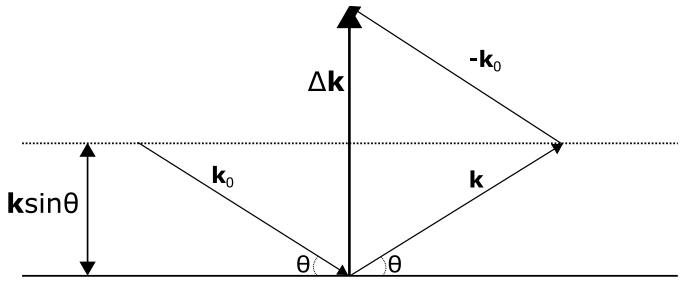

Figure 2.3: Relationship between $\Delta\mathbf{k}$ and θ for elastic scattering. $\mathbf{k}_0$ and $\mathbf{k}$ represents the incoming- and final wavevector. The product $\mathbf{k}\sin\theta$ is the spacing between two planes.

Bragg's law may be described from the Laue condition by simple vector geometry. From figure 2.3 one may see that:

$$\Delta\mathbf{k} = 2\mathbf{k}\sin\theta = 2\frac{1}{\lambda}\sin\theta. \tag{2.12}$$

The distance between two planes is given as:

$$d_{hkl} = \frac{1}{\mathbf{g}_{hkl}}. \tag{2.13}$$

Inserting this into the Laue condition one may obtain Bragg's law.

$$2d\sin\theta = \lambda \tag{2.14}$$

In the case of electrons, the wavelength is given by the relativistic de Broglie wavelength.

$$\lambda = \frac{h}{\sqrt{2\mathrm{m_e}eU(1+\frac{eU}{2\mathrm{m_e}c^2})}} \tag{2.15}$$

Here h is the Planck's constant, $\mathrm{m_e}$ the rest mass of an electron, e the elementary charge, U the acceleration potential and c the speed of light.

2.2.2 Dynamic and kinematic conditions

As the electron permeates the matter it may scatter one, two or multiple times. One scattering event is referred to as *kinematic condition*, and to work under these conditions the sample has to be sufficiently thin. In practice this means that sample has to be approximately the distance between two scattering events called the *mean free path*, which is typically around 10 nm for electrons. If the sample is thicker, electrons scatter multiple times and one is now working under *dynamical* conditions.

2.2.3 Structure factor

The intensity of each reflection in a diffraction pattern may be found from the structure factor as given in equation (2.16). The equation sums the scattering contributions from all the atoms in the unit cell, and weights them based on their atomic number.

$$I = |F_{hkl}(\theta)|^2 = |\sum_{j}^{\infty} f_j(\theta) \mathrm{e}^{2\pi i(hx_j+ky_j+lz_j)}|^2 \tag{2.16}$$

Here f_j is the atomic form factor, which is dependent on both the atomic number *Z* and the scattering angle θ. hkl represent the plane and x_j, y_j and z_j represents the position of atom j in the unit cell. The equation is only valid under kinematic conditions, and since this is usually not the case some values of the structure factor may be non-zero when they in theory should be. This means that in diffraction experiments planes which should be non-observable becomes observable.

2.3 Defect chemistry

This chapter is mainly adapted from lecture notes in "Defects and Reaction" by Truls Norby [18].
Solid materials can be either crystalline or amorphous. In crystalline materials, atoms sit on specific lattice points which are periodically repeated in every direction. At temperatures above 0 K, the structure will always differ from its perfect structure. These differences are called *structural defects* and have major influence on a material's functional- and mechanical properties. A perfect crystal has no long-range transport, since the species are restricted to a lattice site. Defects are necessary for transport of atoms, ions and in some cases electrons. Thus, understanding and controlling defects are essential for synthesizing, fabricating, and the use of materials. Defects are categorized based on their dimension:

- Zero-dimension: vacancies, interstitials, substitutions and electronic defects, all limited to one lattice point. These are called point defects.
- One-dimensional: dislocations.
- Two-dimensional: surfaces, grain boundaries and stacking faults.
- Three-dimensional: foreign inclusion, cracks and precipitates. Often referred to as bulk- or volume defects.

In principle, all types of defects may form in a material if the three following criteria are maintained: i) conservation of mass, ii) conservation of charge and iii) conservation of structure. The latter means that if a new anion lattice site is formed, a new cation lattice site must also be formed. This makes sure that the number of lattice sites in a ABO_3 structure always has a ratio of 1:1:3, even though the number of atoms deviates from 1:1:3 [18].

Kröger-Vink notation

A general notation for describing defects was developed by Kröger & Vink in 1956 [19]. The notation is A_s^q, where A is the chemical species (v is used for a vacancy), s is the lattice site (i is used for an interstitial) and q is the effective charge, defined as the real charge of the defect minus the charge the same position would have in a perfect structure. Positive defects are indicated with "•", negative with "′" and neutral with "x".

2.3.1 Defects in $BaZrO_3$

In this section the defects related to Yttrium-doped $BaZrO_3$ (BZY) and the necessary equations and equilibriums to prepare the *Brouwer diagrams* are presented. Some of the central defects in this thesis are presented in table 2.2.
In equilibrium with oxygen gas, oxygen vacancies may be formed under low partial pressures and cations vacancies under high partial pressures according to equations (2.17) and (2.18). In equation (2.18), $\nu''_{Ba} + \nu''''_{Zr} = 2\nu'''_{M}$ is used to make the derivation of Brouwer diagrams easier.

$$O_O^x = \nu_O^{\bullet\bullet} + 2e' + \frac{1}{2}O_{2(g)} \tag{2.17}$$

$$\frac{3}{2}O_{2(g)} = \nu''_{Ba} + \nu''''_{Zr} + 3O_O^x + 6h^\bullet = 2\nu'''_M + 3O_O^x + 6h^\bullet \tag{2.18}$$

Table 2.2: Defects in $BaZr_{1-x}Y_xO_{3-\delta}$ represented in Kröger-vink notation.

Defect	Notation
Oxygen vacancy	$\nu_O^{\bullet\bullet}$
Hydroxide ion on oxygen site	$OH_O^\bullet$
Yttrium on zirconium site	Y'_{Zr}
Electron hole	$h^\bullet$
Electron	e'

Doping

In this thesis acceptor doped $BaZrO_3$ is studied, which relies on substituting Zr with Y. This may be compensated by either oxygen vacancies or electron holes under dry conditions, i.e. non-water containing atmospheres.

$$2BaO + Y_2O_3 = 2Ba_{Ba}^{x} + 2Y_{Zr}' + 5O_O^x + \nu_O^{\bullet\bullet} \tag{2.19}$$

$$2BaO + Y_2O_3 + \frac{1}{2}O_{2(g)} = 2Ba_{Ba}^{x} + 2Y_{Zr}' + 6O_O^x + 2h^{\bullet} \tag{2.20}$$

Hydration

As hydrogen enters the oxide it donates its electron to the more electronegative oxygen, and takes place in the structure as a hydroxide group. This may occur through water vapour or from hydrogen gas.

$$H_2O_{(g)} + 2O_O^x = 2OH_O^{\bullet} + 2e' + \frac{1}{2}O_{2(g)} \tag{2.21}$$

$$H_{2(g)} + 2O_O^x = 2OH_O^{\bullet} + 2e' \tag{2.22}$$

However, it is most common to represent hydration of proton conducting materials by the dissociative uptake from water according to reaction (2.23). Here it becomes clear, if the material is successfully acceptor doped with oxygen vacancies as the compensating charge; the vacancies are a necessity for further hydration. Also, if there is no water vapour present, the material will exhibit oxygen ion conductivity. The reaction enthalpy, ΔH_{hyd}°, for reaction (2.23) is negative and thus exothermic. This makes protonic defects dominate at low temperatures and oxygen vacancies at higher temperatures.

$$H_2O_{(g)} + \nu_O^{\bullet\bullet} + O_O^x = 2OH_O^{\bullet} \tag{2.23}$$

Electroneutrality condition

The full electroneutrality condition for the doped system thus becomes:

$$p + 2[\nu_O^{\bullet\bullet}] + OH_O^{\bullet} = n + 3[\nu_M'''] + Y_{Zr}', \tag{2.24}$$

and this will be used further.

Other defect equations

There are scenarios which may influence the material's properties. One is: the evaporation Ba, which may occur according to reactions (2.25) or (2.26) during synthesis [20, 21].

$$\mathrm{Ba}_{\mathrm{Ba}}^{x} + \mathrm{O}_{\mathrm{O}}^{x} = \nu_{\mathrm{Ba}}'' + \nu_{\mathrm{O}}^{\bullet\bullet} + \mathrm{BaO} \tag{2.25}$$

$$2\mathrm{Ba}_{\mathrm{Ba}}^{x} + \nu_{\mathrm{O}}^{\bullet\bullet} + \mathrm{Y_2O_3} = 2\mathrm{Y}_{\mathrm{Ba}}^{\bullet} + \mathrm{O}_{\mathrm{O}}^{x} + \mathrm{BaO} \tag{2.26}$$

This indicates a possibility of forming less oxygen vacancies, which again will lead to less proton uptake. Since the sintering conditions often are under high temperatures, equation (2.26) might occur unintentionally. Consequently, the formation of a secondary phase such as $\mathrm{Y_2O_3}$ and/or YSZ ($\mathrm{Zr_{0.72}Y_{0.28}O_{1.862}}$) may occur [22, 23].

2.3.2 Defect concentration as function of partial pressures

In order to determine the defects' dependencies on the oxygen partial pressure, reaction (2.17) is used. At higher partial pressures, it is assumed that metal vacancies form according to equation (2.18). The equilibrium reactions for the two reactions and for dissociative water uptake equation (2.23), are given in equations (2.27), (2.28) and (2.29), respectively. Reaction (2.30) is the intrinsic ionization and equation (2.31) is its corresponding equilibrium equation.

$$K_{\nu_{\mathrm{O}}^{\bullet\bullet}} = \frac{[\nu_{\mathrm{O}}^{\bullet\bullet}]\mathrm{n}^2 p_{\mathrm{O_2}}^{1/2}}{[\mathrm{O}_{\mathrm{O}}^{x}]} \tag{2.27}$$

$$K_{\nu_{\mathrm{M}}'''} = \frac{[\nu_{\mathrm{Ba}}''][\nu_{\mathrm{Zr}}'''']\mathrm{p}^6[\mathrm{O}_{\mathrm{O}}^{x}]^3}{p_{\mathrm{O_2}}^{3/2}} = \frac{[\nu_{\mathrm{M}}''']^2\mathrm{p}^6[\mathrm{O}_{\mathrm{O}}^{x}]^3}{p_{\mathrm{O_2}}^{3/2}} \tag{2.28}$$

$$K_{\mathrm{hyd}} = \frac{[\mathrm{OH}_{\mathrm{O}}^{\bullet}]^2}{[\nu_{\mathrm{O}}^{\bullet\bullet}][\mathrm{O}_{\mathrm{O}}^{x}]p_{\mathrm{H_2O}}} \tag{2.29}$$

$$0 = \mathrm{e}' + \mathrm{h}^{\bullet} \tag{2.30}$$

$$K_{\mathrm{i}} = \mathrm{np} \tag{2.31}$$

These equations enable the determination of the defects dependencies on the oxygen- and water partial pressure under different boundary conditions. The oxygen gas is assumed *dry*, meaning protons are a minority defect over the whole pressure range. The corresponding Brouwer diagrams are presented in figures 2.4a and 2.4b. A full derivation of the Brouwer diagrams may be found in Appendix A.

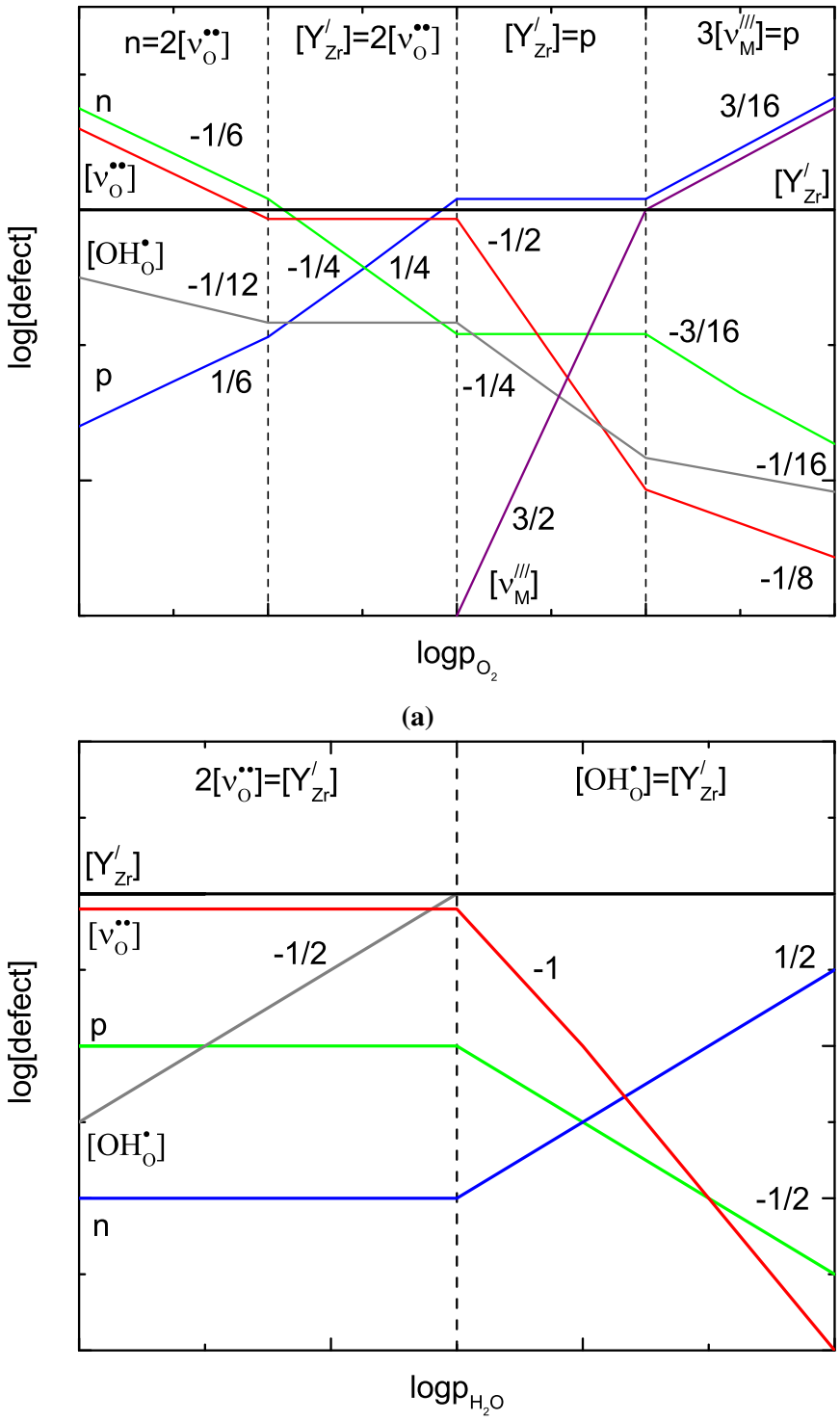

Figure 2.4: Brouwer diagrams for Y-doped $BaZrO_3$. (a) shows the defect dependencies on oxygen partial pressure, while (b) for water vapour partial pressure. The dotted lines separates areas of different dominating defects.

2.4 Space-charge

This section is mainly adapted from Kjølseth *et al*. [24]. A more theoretical and detailed description may be found in [25–27].
When the periodicity of a bulk structure is disrupted by two-dimensional defects, such as grain boundaries and surfaces, a space-charge layer is formed. The origin of space-charge is accumulation of charged defects in the grain boundary core and in the adjacent space-charge regions. Occurrence of these defects is related to the difference in Gibbs energy of formation in the bulk and in the grain boundary. Due to the electroneutrality principle an opposite charge of what is in the core is formed in the surrounding layers, which generates a difference in the electrostatic potential between the grain interior and the grain boundary core. This difference is denoted the Schottky barrier height, $\Delta\phi(0)$. A high barrier means a higher concentration of opposite charged defects. A schematic representation of the space-charge model is given in figure 2.5 and here $\lambda^{\star}$ is the effective space-charge layer width.

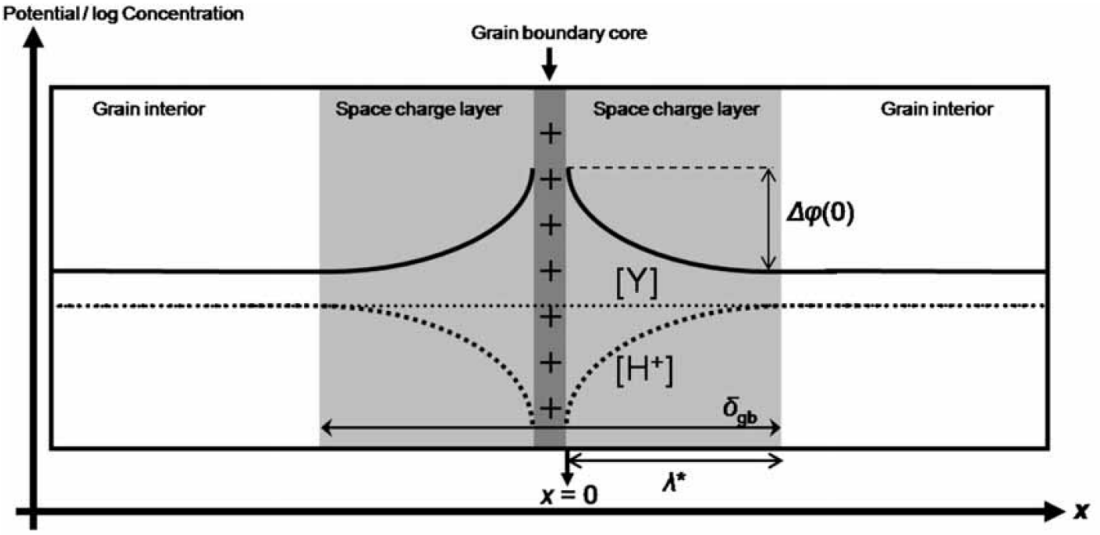

Figure 2.5: Schematic overview of a positively charged grain boundary core, compensated by two surrounding space-charge layers. The x is defined such as $x = 0$ is the interface between grain boundary core and space-charge layer, while $= \infty$ is the grain interior. The dotted lines represent concentration profiles for protons and the acceptor dopant under the Mott-Schottky approximation. The drawn line represents the potential profile. The figure reproduced from [24].

2.4.1 Electrochemical potential

The electrochemical potential for a mobile charge carrier *j* in the bulk region is given by:

$$\eta_j(\infty) = \mu_j^\circ + \mathrm{k_B}T \ln c_j(\infty) + z_j \mathrm{e}\phi(\infty). \tag{2.32}$$

Here μ_j° is the standard chemical potential for specie *j*, $c_j(\infty)$ is the concentration in the bulk and $\phi(\infty)$ is the electrostatic potential in the bulk. The rest of the symbols have their usual meanings.
The electrochemical potential of a mobile charge carrier as a function of distance x from the grain boundary core interface at x = 0 is defined as:

$$\eta_j(x) = \mu_j^\circ + \mathrm{k_B}T \ln c_j(x) + z_j \mathrm{e}\phi(x). \tag{2.33}$$

At equilibrium, when $\eta_j(\infty) = \eta_j(x)$, the difference in the electrostatic potential can be expressed as:

$$\Delta\phi(x) = \phi(x) - \phi(\infty) = -\frac{\mathrm{k_B}T}{z_j \mathrm{e}} \ln \frac{c_j(x)}{c_j(\infty)}. \tag{2.34}$$

This can be rewritten as:

$$\frac{c_j(x)}{c_j(\infty)} = \exp\left(-\frac{z_j e \Delta\phi(x)}{\mathrm{k_B}T}\right), \tag{2.35}$$

and now relates the concentration of defects to the potential difference. In accordance with the *Poisson's equation*, this potential is dependent on the charge density Q(*x*) in the space-charge layer:

$$\frac{\mathrm{d}^2\Delta\phi(x)}{\mathrm{d}x^2} = -\frac{1}{\varepsilon_0\varepsilon_r}\mathrm{Q}(x). \tag{2.36}$$

Further it is assumed that temperatures and water vapour pressure are fixed so that protons are the dominating positive charge compensating defect, and thus strongly depleted in the space-charge layers. The net charge density Q(*x*) is then governed by the acceptor dopant concentration. The next approximation is the *Mott-Schottky* approximation, which is valid for temperatures where the cations are considered to be "frozen in". It states that the concentration is constant up to the grain boundary core, as seen in figure 2.5. Following this, the charge density in the grain boundary is given by the concentration of the acceptor dopant. If the cations are mobile, usually at high temperatures above 1000 °C, *Gouy-Chapman* approximation needs to be considered instead.

The *Debye length* is defined as:

$$L_{\mathrm{D}} = \left(\frac{\mathrm{k_B} T \varepsilon_0 \varepsilon_r}{2\mathrm{e}^2 c_j(\infty)} \right)^{1/2}. \tag{2.37}$$

Furthermore, the potential between the core and the space-charge layer, i.e. Schottky barrier height, is defined as: $\Delta\phi(0)$ = $\phi(0)$ - $\phi(\infty)$. The effective space-charge layer width, $\lambda^\star$, is defined as:

$$\lambda^\star = 2L_{\mathrm{D}} \left(\frac{\mathrm{e}\Delta\phi(0)}{\mathrm{k_B} T} \right)^{1/2} = \left(\frac{2\varepsilon_0 \varepsilon_r \Delta\phi(0)}{\mathrm{e} c_j(\infty)} \right)^{1/2}. \tag{2.38}$$

One may now derive an expression for proton concentration in terms of potential barrier at the boundary by applying semi-infinite boundary conditions and neglecting the depleted defects in the space-charge layers. The analytic result is given in terms of proton concentration in equation (2.39).

$$\frac{c_{\mathrm{H^+}}(x)}{c_{\mathrm{H^+}}(\infty)} = \exp\left[-\frac{1}{4} \left(\frac{x - \lambda^\star}{L_{\mathrm{D}}} \right)^2 \right] \tag{2.39}$$

One may see that for $x > \lambda^\star$, i.e. outside the space-charge zone, the solution is 1.
The Schottky barrier height may be obtained by knowing the ratio between the specific bulk conductivity $\sigma^{\mathrm{sp}}_{\mathrm{bulk}}$ and grain boundary conductivity $\sigma^{\mathrm{sp}}_{\mathrm{GB}}$. The grain boundary conductivity depends on the distance from the core, and is therefore an effective property of the entire boundary, which may be obtained from integrating the resistance over the thickness of the boundary. To do this one assumes that the proton mobility is equal in bulk and grain boundaries, and that equation (2.35) can be expressed through specific conductivities by substituting the concentration with $\sigma_{\mathrm{H^+}} = \mathrm{e} c_{\mathrm{H^+}} \mu_{\mathrm{H^+}}$. The following equation is obtained when inverting the grain boundary conductivity into resistivity:

$$\frac{c_{H^+}(x)}{c_{H^+}(\infty)} = \frac{\sigma^{\mathrm{sp}}_{\mathrm{bulk}}}{\sigma(x)} = \sigma^{\mathrm{sp}}_{\mathrm{bulk}} \rho(x) = \exp\left(\frac{e\Delta\phi(x)}{\mathrm{k_B} T} \right). \tag{2.40}$$

Here $\sigma(x)$ and $\rho(x)$ are the proton conductivity and resistivity respectively, at a position *x* in the space-charge layer. The effective specific resistivity in the space-charge layer thickness is obtained by integrating and dividing by the thickness:

$$\frac{\sigma^{\mathrm{sp}}_{\mathrm{bulk}}}{\sigma^{\mathrm{sp}}_{\mathrm{GB}}} = \sigma^{\mathrm{sp}}_{\mathrm{bulk}} \rho^{\mathrm{sp}}_{\mathrm{GB}} = \frac{1}{\lambda^\star} \int_0^{\lambda^\star} \exp\left(\frac{e\Delta\phi(x)}{\mathrm{k_B} T} \right) \mathrm{d}x. \tag{2.41}$$

The integral is solved by changing the variable from x to $\Delta(\phi)$ and integrating as done in [25]. The solution in terms of proton conductivity is given as:

$$\frac{\sigma_{\text{bulk}}^{\text{sp}}}{\sigma_{\text{GB}}^{\text{sp}}} \approx \frac{\exp\left(\frac{\mathrm{e}\Delta\phi(0)}{\mathrm{k_B}T}\right)}{\frac{2\mathrm{e}\Delta\phi(0)}{\mathrm{k_B}T}}. \tag{2.42}$$

2.5 Electrical conductivity

2.5.1 Transport in electrical fields

When charge carriers with charge z_je are subjected to an electric field, *E*, the carriers are affected by a force proportional to the electrical field and concentration c_j. This force give rise to a current:

$$i_j = \sigma_j E = z_j \mathrm{e} c_j u_j E, \tag{2.43}$$

where σ_j is the partial conductivity of specie *j*, and u_j is the corresponding mobility. The total conductivity is the sum of all the partial conductivities.

$$\sigma_{\text{tot}} = \sum_j \sigma_j \tag{2.44}$$

An important parameter is the transport number, t_j, which indicates how much of the total conductivity that stems from a specific charge carrier *j*.

$$t_j = \frac{\sigma_j}{\sigma_{\text{tot}}} \tag{2.45}$$

In materials, where the transport follows an activated jump mechanism, one may relate mobility to diffusion through the Nernst-Einstein equation:

$$D_j = u_j \frac{\mathrm{k_B}T}{z_j \mathrm{e}} = \sigma_j \frac{\mathrm{k_B}T}{c_j z_j^2 \mathrm{e}^2}. \tag{2.46}$$

Evaluating equation (2.46) in an *Arrhenius* type plot gives the activation energy.

$$\sigma_j = \frac{\sigma_0}{T} \exp\left(-\frac{\Delta E_a}{\mathrm{k_B}T}\right) = (z_j \mathrm{e} c_j u_{j,0}) \frac{1}{T} \exp\left(-\frac{\Delta E_a}{\mathrm{k_B}T}\right) \tag{2.47}$$

Here σ_0 is the pre-exponential factor, which consists of the entropy of formation and entropy of mobility. The activation energy is similarly a sum of the enthalpy of formation and mobility. A plot of $\ln(\sigma T)$ vs. $1/(\mathrm{k_B}T)$ can be constructed to determine the values.

2.5.2 Mobility of protonic defects

The proton mobility in perovskites oxides occurs by proton hopping between adjacent oxygen ions at standard lattice sites through the *Grotthuss* mechanism. This occurs by rotational diffusion of the proton around an oxygen ion, followed by proton transfer towards a neighbouring oxide ion as shown schematically in figure 2.6. When the bond between the red sphere cation and the oxygen ions A and B is bent, the energy barrier for proton transfer is lowered, enabling bond formation between the proton and the B oxygen ion. The proton will then rotate around the B oxygen ion until a new possibility for proton transfer occurs.

If the oxygen-hydrogen-oxygen bond had been linear, thermodynamics provide an activation enthalpy of this long-range proton diffusion of no more than 0.15 eV, and at separation less than 250 pm the barrier vanishes completely. However, in cubic perovskites the activation enthalpy for the mobility is in the order of $0.4-0.6$ eV [4, 7]. Deviation from an ideal perovskite structure also influences the activation energy for the proton conduction. This is common in the perovskites $BaCeO_3$ and $SrCeO_3$, where the barrier is higher for the latter. Local chemical perturbation due to cation doping can also influence the proton mobility.

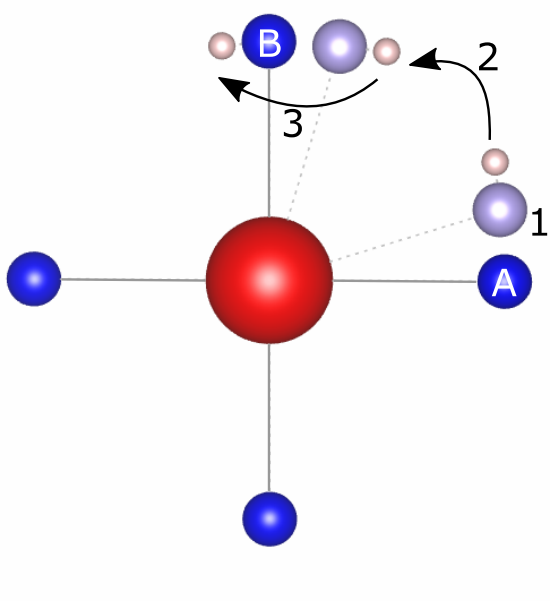

Figure 2.6: Possible proton transfer mechanism from an oxygen ion A to oxygen ion B. Both oxygen ions vibrate (1) until the proton may form a bond with B (2). The proton then rotates around B (3) and the mechanism is restarted.

2.6 Impedance spectroscopy

A measurement technique frequently applied in order to study the electrical properties of ceramic materials is impedance spectroscopy. The sample is subjected to an alternating externally applied potential, which polarizes different components in the material, e.g. grain boundaries, bulk and electrode processes [28]. These components respond to different frequencies, and thus enables their separation. The measurements are usually conducted over a range of atmospheres and temperatures.

2.6.1 Alternating current and impedance

An alternating voltage can be described through a sinusoidal function:

$$U = U_0 \sin(\omega t). \tag{2.48}$$

Here U_0 is the amplitude and ω is the angular frequency, related to the frequency by $\omega = 2\pi f$. The product ωt is called the phase angle. As an alternating voltage is applied to a sample, an alternating current in the sample will respond, but out of phase due to induction and capacitances within the sample. The current is then described as:

$$I = I_0 \sin(\omega t + \theta), \tag{2.49}$$

where θ is the phase offset. The current is a product of two components: one real in phase, and one imaginary 90° out of phase. These are called resistance, R, and reactance, X. The general term of resistance including both components is the *impedance*, Z. The total impedance is then represented in the complex plane as:

$$Z^* = Z_{\text{re}} + iZ_{\text{im}} = R + iX. \tag{2.50}$$

The inverse property of impedance is the *admittance* and has a real and imaginary part called conductance and susceptance given as:

$$Y^* = \frac{1}{Z} = G + iB. \tag{2.51}$$

2.6.2 Passive circuit elements

The dielectric response in a polycrystalline material may be fitted using equivalent circuits consisting of both active and passive elements. In this thesis only passive circuit elements are used.

Resistor

A resistor reduces the current flow and lowers the voltage in the circuit. The resistance is given as:

$$R = \frac{U}{I} = \frac{U_0 \sin(\omega t)}{I_0 \sin(\omega t)} = \frac{U_0}{I_0} \tag{2.52}$$

As may be seen, the resistor is the same for an alternating- and direct current, since it is independent of ω. The resistor will thus only contribute to the real part of the impedance. It has the unit Ohm, Ω.

Capacitor

A capacitor is an ideal insulator sandwiched between two conductors and often represented as two parallel plates separated by a vacuum or dielectric material. An applied voltage will induce charging at the plates, giving them a net charge. Capacitance is defined as: $C = Q/U$ and has the unit of Farad, F.
If the separating medium is polarizable, the dipole will be directed according to the electrical field in the capacitor and counteract the field by reducing the voltage. This will change the value of the capacitance and the difference between this capacitance and the initial is called the relative permittivity, ε_r. The general formulation for a capacitor is:

$$C = \varepsilon_0 \varepsilon_r \frac{A}{d}. \tag{2.53}$$

When operating with AC the current has a phase offset of 90° with respect to the voltage, and will thus only contribute to the imaginary part of the impedance.

$$Z_{\text{cap}} = -i \left(\frac{1}{\omega C} \right) \tag{2.54}$$

Inductor

Opposite to the capacitor, an inductor is an ideal conductor. In an alternating field it will induce current, which generates a magnetic field. According to *Lenz's law* the direction of the induced electro-magnetic force (emf) is such that it opposes the change in current that created it. The current then has a phase offset of 90° with respect to the voltage, and contributes to the imaginary part of the impedance:

$$Z_{\text{ind}} = i\omega L \tag{2.55}$$

Here L is the inductance with the unit Henry, H.

2.6.3 Impedance sweeps

In an impedance sweep, the complex impedance of a system is measured over a large frequency range (often from 1 MHz to 0.1 Hz). The negative reactance is plotted against the resistance at the same frequency in what is called a *Nyquist plot*. In a polycrystalline material this may result in a plot consisting of 3-4 semicircles; each corresponding to a distinct part of the system, which may be fitted accordingly using an equivalent circuit. The response is attributed to the components difference in relaxation frequency in a material with a given dielectric constant.
The frequency in the circle's apex is the characteristic angular frequency, where the resistor and the capacitor equally contribute to the conductivity. The relation between characteristic angular frequency, conductivity and dielectric is given as [29]:

$$\omega_0 = \frac{1}{RC} = \frac{1}{(\frac{L}{\sigma A})(\frac{\varepsilon_0 \varepsilon_r A}{L})} = \frac{\sigma}{\varepsilon_0 \varepsilon_r}, \tag{2.56}$$

and is independent of geometry. This equation shows that when the dielectric constant for bulk and grain boundaries is somewhat similar, the difference in the frequency must be attributed to different values of conductivity.
Real measurements often give depressed semicircles, resulting from grain geometry and orientation with respect to the applied field. The equivalent circuit is then described using a Constant Phase Element (CPE), Q, which has an impedance:

$$Z^* = (Y_0(i\omega)^n)^{-1} = \left(Y_0(\omega)^n \cos(\frac{n\pi}{2}) + i(Y_0(\omega)^n \sin(\frac{n\pi}{2}))\right)^{-1}. \tag{2.57}$$

Bulk- and grain boundary semicircles are thus explained as an Resistance-CPE (RQ) circuit, where the characteristic angular frequency is given by equation (2.58) and the corresponding capacitance by equation (2.59).

$$\omega_0 = \left(\frac{1}{Y_0 R}\right)^{1/n} \tag{2.58}$$

$$C = \frac{1}{R\omega_0} = Y_0^{1/n} R^{1/n-1} \tag{2.59}$$

2.6.4 Brick-layer model

The theory behind this section is modified from [29].
The brick-layer model is a simplified way to describe polycrystalline material's geometry and relate it to an equivalent circuit. The idea is to restrict the microstructure to a

matrix of cubical grains, separated by flat grain boundaries oriented parallel and serial to the direction of the current. Figure 2.7 shows a schematic model in which L is the sample's length, A is the cross section area, G is the grain length and g is the thickness of the grain boundaries.

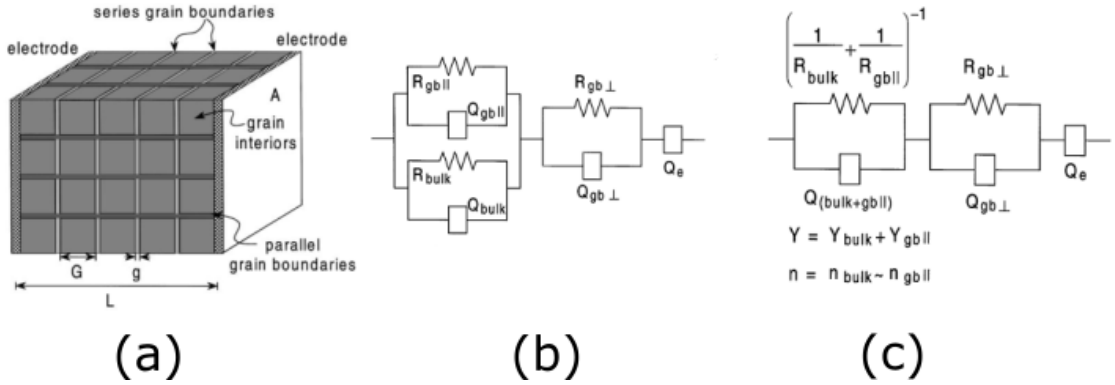

Figure 2.7: Brick-Layer model of a polycrystalline material in (a), with corresponding equivalent circuit (b) and reduced circuit (c). Here R and Q denotes a resistor and a constant phase element, respectively. Figure is modified from [29].

Assuming that bulk and the two grain boundaries may be described by a (RQ) circuit element, the equivalent circuit in figure 2.7(b) is obtained. This may further be reduced to (c). By defining $\sigma_j = L/(AR_j)$ the following expressions for the conductivity may be obtained:

$$\frac{1}{R_1} = \sigma_1 = \frac{2g}{G}\sigma_{\text{GB}} + \sigma_{\text{bulk}} \tag{2.60}$$

$$\frac{1}{R_2} = \sigma_2 = \frac{G}{g}\sigma_{\text{GB}}. \tag{2.61}$$

These equations may be evaluated in terms of three limiting conditions:
i) $\sigma_{\text{bulk}} > \sigma_{\text{GB}}$, ii) $\sigma_{\text{bulk}} < \sigma_{\text{GB}}$ and iii) $\sigma_{\text{GB}} \approx \sigma_{\text{bulk}}$. Assuming the case of i), the angular frequency in equation (2.56) will be higher for bulk and parallel grain boundaries, than for serial grain boundaries. If the resistance does not differ by more than 2-3 orders of magnitude the two semicircles will be observed in the spectrum, wherein the first one represents bulk + parallel grain boundaries, and the other the serial grain boundaries. In materials with normal microstructure ($g << G$), the parallel grain boundary will not contribute much to the capacitance or conductivity. This assumption reduces equation (2.60) to $\sigma_1 = \sigma_{\text{bulk}}$. Furthermore, one may write the capacitances as:

$$C_1 \approx C_{\text{bulk}} = \frac{A}{L}\varepsilon_{\text{bulk}}\varepsilon_0 \tag{2.62}$$

$$C_2 \approx C_{\mathrm{GB}} = \frac{A}{L}\frac{G}{g}\varepsilon_{\mathrm{GB}}\varepsilon_0. \tag{2.63}$$

Under the assumption that the dielectric constant of bulk and grain boundaries do not differ much, one may relate the capacitances through the following equation:

$$\frac{C_1}{C_2} = \frac{g}{G}, \tag{2.64}$$

and is used when reporting the specific grain boundary conductivity.

2.7 Quantum mechanical modelling

Modelling materials from first principles has become an important tool for the understanding of solids. In this thesis, the Density Functional Theory (DFT) is utilized, as implemented in the Vienna Ab-initio Simulation Package (VASP) package [30, 31]. This chapter presents basic concepts of DFT, as more comprehensive descriptions may be found elsewhere [32–34].

2.7.1 The many-particle problem

The interaction between atoms may be described through the non-relativistic Schrödinger's equation:

$$\hat{H}\Psi_i(\mathbf{r}_i, \mathbf{R}_\alpha) = E_i\Psi_i(\mathbf{r}_i, \mathbf{R}_\alpha) \tag{2.65}$$

where $i = 1, 2, ..., N$ and the Hamiltonian, $\hat{H}$, is given by:

$$\begin{aligned}\hat{H} = &-\sum_{j=1}^{N_\mathrm{e}} \frac{\hbar^2\nabla_j^2}{2\mathrm{m_e}} - \sum_{\alpha=1}^{N_\mathrm{n}} \frac{\hbar^2\nabla_\alpha^2}{2m_\alpha} + \sum_{j<j'}^{N_\mathrm{e}} \frac{\mathrm{e}^2}{|\mathbf{r_j} - \mathbf{r'_j}|} \\ &+ \sum_{\alpha<\alpha'}^{N_\mathrm{n}} \frac{\mathrm{e}^2 Z_\alpha^2 Z_{\alpha'}^2}{|\mathbf{R}_\alpha - \mathbf{R}'_\alpha|} - \sum_{j=1}^{N_\mathrm{e}}\sum_{\alpha=1}^{N_\mathrm{e}} \frac{\mathrm{e}^2 Z_\alpha}{|\mathbf{r_j} - \mathbf{R}_\alpha|}.\end{aligned} \tag{2.66}$$

The two first terms represent the kinetic energy of electrons and nuclei, respectively. The three latter terms describe electrostatic interactions between electrons, nuclei, and between nuclei and electrons. Solving this is a huge numerical problem as 1 cm^3 of matter contains roughly 10^{22} nuclei and 10^{23} electrons, resulting in a sum of $\sim 10^{40}$ terms for the two-particle operators. Thus, olving real systems require simplifications which do not alter the physical properties. As a first approximation, the *Born-Oppenheimer approximation* is applied. This separates equation (2.66) into an electron- and a nuclei wavefunction, under the assumption that the nuclei are stationary compared to the

electrons due to their mass difference. The Hamiltonian is then reduced to:

$$\hat{H} = -\sum_{j=1}^{N_e} \frac{\hbar^2 \nabla_j^2}{2\mathrm{m_e}} + \sum_{j<j'}^{N_e} \frac{\mathrm{e}^2}{|\mathbf{r_j} - \mathbf{r'_j}|} - \sum_{j=1}^{N_e} \sum_{\alpha=1}^{N_n} \frac{\mathrm{e}^2 Z_\alpha}{|\mathbf{r_j} - \mathbf{R}_\alpha|}. \tag{2.67}$$

This reduces the number of interactions, but is still only feasible to solve for small systems. Approaches for solving the electron part have been developed, and DFT is one such method.

2.7.2 Density functional theory

The DFT is an *ab initio* approach to solve the many-particle problem and is based on the theorems by Hohenberg & Kohn [35].
The first theorem states that an external potential, $V_{\text{ext}}(\mathbf{r})$, for any systems of electrons is determined uniquely by the ground state density, $n_0(\mathbf{r})$. Knowing $n_0(\mathbf{r})$ gives $V_{\text{ext}}(\mathbf{r})$, which again results in an exact $\hat{H}$. The ground state density thus determines all the ground state properties. The second theorem states that there exist an universal functional of the electron density, $F_{\text{HK}}\,[n(\mathbf{r})]$, and the exact ground-state is the global minimum of this functional. The total energy functional is written as:

$$E[n(\mathbf{r})] = T[n(\mathbf{r})] + U_{\text{ee}}[n(\mathbf{r})] + U_{\text{en}}[n(\mathbf{r})], \tag{2.68}$$

where the terms are functionals of $n(\mathbf{r})$ representing the kinetic energy, electron-electron and electron-nuclei interactions, respectively. The latter may be defined according to equation (2.69).

$$U_{en}[n(\mathbf{r})] = \int V_{\text{ext}}(r) n(\mathbf{r}) d\mathbf{r} \tag{2.69}$$

Defining the Hohenberg-Kohn functional as: $F_{\text{HK}}[n(\mathbf{r})] = T[n(\mathbf{r})] + U_{\text{ee}}[n(\mathbf{r})]$, one may see that it does not depend on the external potential, i.e. it has the same form for all systems of electrons. One may further split electron-electron functional into the Hartree term (classical Coulomb repulsion) and the exchange-correlation term, denoted $E^{\text{H}}[n(\mathbf{r})]$ and $E_{\text{xc}}[n(\mathbf{r})]$, respectively.
Practical implementation of density functional was proposed by Kohn & Sham in 1965 [36]. They showed that finding the correct electron density can be done through solving a set of independent single-electron wavefunctions. The Kohn-Sham equations have the form:

$$\left\{ \frac{-\hbar^2 \nabla_j^2}{2\mathrm{m_e}} + V_{\text{eff}} \right\} \psi_j^{\text{KS}}(\mathbf{r}) = \epsilon_j^{\text{KS}} \psi_j^{\text{KS}}, \tag{2.70}$$

where V_{eff} is defined as:

$$\begin{aligned} V_{\text{eff}} &= V_{\text{ext}}(\mathbf{r}) + \frac{\delta E^{\text{H}}[n(\mathbf{r})]}{\delta n(\mathbf{r})} + \frac{\delta E_{\text{xc}}[n(\mathbf{r})]}{\delta n(\mathbf{r})} \\ &= V_{\text{ext}}(\mathbf{r}) + V_{\text{H}}[n(\mathbf{r})] + V_{\text{xc}}[n(\mathbf{r})]. \end{aligned} \tag{2.71}$$

Solving for the density is done iteratively by a self-consistent field calculation, beginning with an initial guess of the density. The KS equations are then solved and a new density is then obtained from:

$$n(\mathbf{r}) = \sum_{j=1}^{N_{\text{e}}} |\psi_j^{\text{KS}}(\mathbf{r})|^2, \tag{2.72}$$

and repeated until the ground state is obtained.
In principle, the method is exact if one is able to determine the $E_{\text{xc}}[n(\mathbf{r})]$ term. Today approximations are used, but the development of modern DFT mainly focuses on developing this term.

Exchange-correlation approximations

The simplest approximation was suggested by Kohn & Sham and is the Local Density Approxiamtion (LDA). The contribution is thought to be similar to that of a uniform electron gas with similar electron density and energy $\epsilon_{\text{xc}}^{\text{gas}}$. The local density is thus homogeneous throughout the system and is given by:

$$E_{\text{xc}}^{\text{LDA}}[n(\mathbf{r})] = \int n(\mathbf{r}) \epsilon_{\text{xc}}^{\text{gas}}[n(\mathbf{r})] d\mathbf{r}. \tag{2.73}$$

The approximation works well for systems with little local variation in the electron density, but is not well suited for other system. A common drawback of LDA is the underestimation of the lattice parameters due to overestimation in bond strengths. Another approximation is to make us of the gradient of the electron density which is the idea behind the Generalized-Gradient Approximation (GGA). This takes the form:

$$E_{\text{xc}}^{\text{GGA}}[n(\mathbf{r})] = \int n(\mathbf{r}) \epsilon_{\text{xc}}^{\text{gas}} d\mathbf{r}[n((\mathbf{r}), \nabla n(\mathbf{r}))] d\mathbf{r}. \tag{2.74}$$

Many versions of the GGA exist, and in this thesis the GGA by Perdew, Burke and Ernzerhof (PBE) has been used as the exchange-correlation functional [37].

Plane waves

In section 2.1, crystals were described as 3d-periodic through equation (2.1). Solving the wavefunction can be simplified by representing the system in a periodic unit cell. One may now apply *Bloch's theorem* which states that the eigenfunctions of the wave equation for a periodic potential are the product of a plane wave $\mathrm{e}^{i(\mathbf{k}\cdot\mathbf{r})}$ times a function $u_k(\mathbf{r})$, which is the periodicity of the crystal structure.

$$\psi_k(\mathbf{r}) = \mathrm{e}^{i(\mathbf{k}\cdot\mathbf{r})} u_k(\mathbf{r}) \tag{2.75}$$

Here $u_k(\mathbf{r}) = u_k(\mathbf{r}+\mathbf{R})$. The periodic part may further be written as a Fourier series by using the reciprocal lattice vector $\mathbf{g}$.

$$u_k(\mathbf{r}) = \sum_{\mathbf{g}} c_{k,\mathbf{g}} \mathrm{e}^{i(\mathbf{g}\cdot\mathbf{r})} \tag{2.76}$$

The full wavefunction can thus be expressed as:

$$\psi_k(\mathbf{r}) = \sum_{\mathbf{g}} c_{k,\mathbf{g}} \mathrm{e}^{[i(\mathbf{g}+\mathbf{k})\mathbf{r}]}, \tag{2.77}$$

where the sum is over all reciprocal lattice vectors. This is valid for systems where the electrons have crystal periodicity, i.e. not free electrons. At this point we are left with an infinite sum, but this is solved by truncating the infinite sum to only include terms with kinetic energies less than some value, since the terms with lower energy have more physical meaning than those of higher energies. This process is further referred to as the *energy cutoff*.

$$E_{\text{cut}} = \frac{\hbar^2}{2\mathrm{m_e}} g_{\text{cut}}^2 \tag{2.78}$$

The total energy of the system will converge towards some value when increasing E_{cut}. Choosing a sufficient number of ***k**-points* is a difficult task since this determines the accuracy of the integrals solved over the Brillouine Zone. An effective way is to make use of the symmetry of a crystal and then only need to account for $\mathbf{k}$-points in the irreducible Brillouin Zone. The total energy will vary and converge in a similar manner as for E_{cut}.

2.8 Transmission Electron Microscopy (TEM)

Since the major part of the experimental work in this thesis is by TEM, a section is dedicated to the concepts of the instrument.

Ever since its discovery by Max Knoll & Ernst Ruska in 1931, the TEM has been in constant development in order to obtain a higher resolution. Today, TEM is an absolutely essential tool for fundamental and applied study of materials in a range of disciplines, and is not limited only to imaging, but is also coupled with various diffraction- and spectroscopic techniques. The instrument enables simultaneous imaging, diffraction and spectroscopy from smaller regions than any other techniques. In some cases: even all the way down to single atomic columns.

2.8.1 Instrument

TEM utilizes electrons instead of visible light to illuminate a sample. These electrons are generated from a filament or from a field emission source by applying a voltage over a thin needle. They are accelerated by a potential (usually $60-300$ kV) and guided by a set of electrical fields, magnetic lenses and apertures before reaching the sample. Images are viewed either on a fluorescence screen or on a computer display, where signals are acquired through a Charge Coupled Device (CCD). Detectors for Energy-Dispersive Spectroscopy (EDS) are located slightly above the sample, while the Electron Energy-Loss Spectroscopy (EELS) signals are gathered after the viewing screen. A schematic representation is given in figure 2.8.

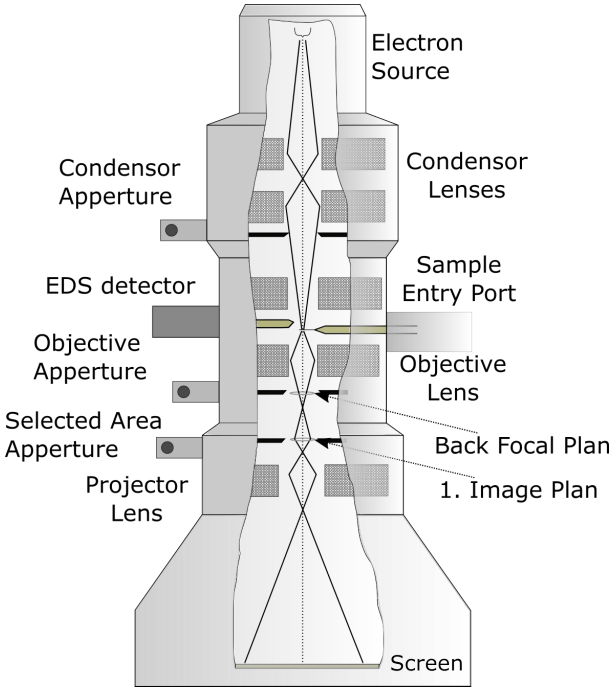

Figure 2.8: Schematic view of a TEM instrument showing some of its components and their location with respect to the optical axis.

2.8.2 Interactions

As the high energy electrons traverse the material, they will interact with the nucleus and electron cloud of the atoms. These interactions generate signals, which upon detection may be used for imaging and chemical analysis. A summary of these signals is given in figure 2.9. Apart from the characteristic X-rays used for EDS, the TEM utilises the forward scattered electron: elastically- and inelastically scattered electrons and the direct beam.

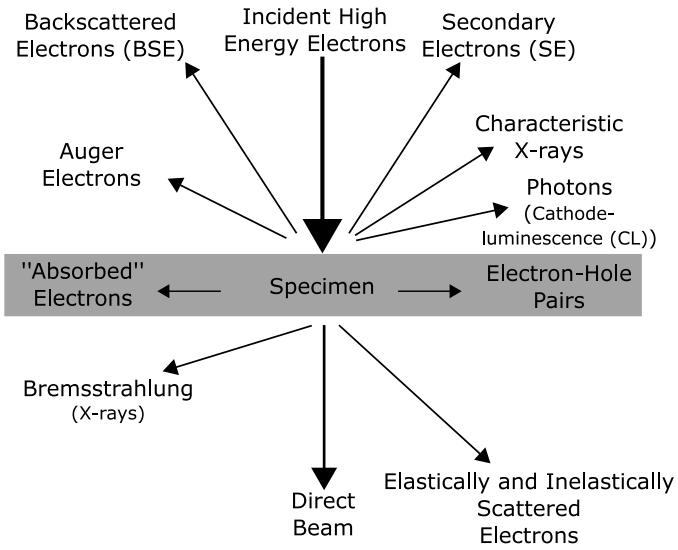

Figure 2.9: A schematic figure representing the signals generated from a thin specimen when high energy electrons interacts with it.

2.8.3 Experimental techniques

It is normal to distinguish between TEM- and Scanning Transmission Electron Microscopy (STEM) mode. In TEM, an area of the specimen is illuminated by a parallel incoming beam, whilst in STEM mode the beam is converged to a well defined beam and scanned over the specimen. This is illustrated in figure 2.10. In the proceeding sub-chapters the experimental techniques which have been utilised will be described

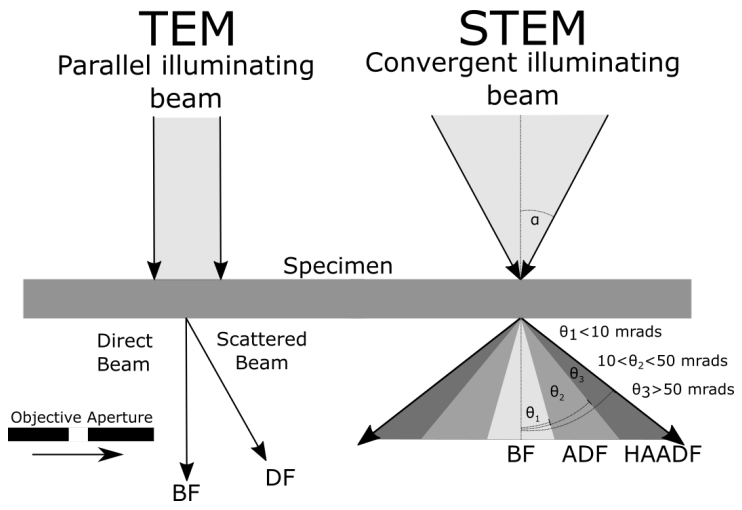

Figure 2.10: In TEM, the specimen is illuminated by a parallel beam, whilst in STEM a convergent beam with a convergence semi-angle, α, is used. In TEM, the objective aperture is inserted in the back-focal plane to filter out contrast forming electrons, whilst in STEM annular detectors are situated at different scattering angles, θ, from the optical axis.

High-resolution TEM (HRTEM)

As the electron waves scatters from a specimen the phase of the wave changes. An image is then formed by the interference between the diffracted beam and the direct beam. If the resolution of the microscope is sufficient, and the sample area is oriented along a low-index zone axis, High-Resolution TEM (HRTEM) images may be obtained, usually showing the atomic structure. The contrast mechanism behind HRTEM is thus referred to as "phase contrast".

It may be shown that the scattered wavefunction, ψ_{sc}, is a sum of individual spherical wavelets as following:

$$\psi_{\text{sc}}(\mathbf{r}) = -\frac{UV\text{m}_\text{e}}{2\pi N\hbar^2}\sum_{\mathbf{r}_j}^{N}\psi_{\text{in}}(\mathbf{r}_j)\frac{\text{e}^{ik|\mathbf{r}-\mathbf{r}_j|}}{|\mathbf{r}-\mathbf{r}_j|}, \tag{2.79}$$

where U is the potential of the medium with volume V. N is the number of uniformly spaced scattering points with coordinate $\mathbf{r}_j$. The last term represents the individual wavefronts emanating from each point [16]. However, it should be emphasised that HRTEM does not directly reveal atomic columns; it reveals the intensity maxima and minima from the resulting interference pattern, and is labelled *lattice fringes*.

Another pattern which may arise due to phase contrast is the *Moiré Patterns*. These stem from interference between lattice fringes of overlapping crystals, and appear coarser

with larger spacing. An example showing both may be seen in figure 2.11. The general formula to calculate the spacing between the Moiré fringes is:

$$d_{\mathrm{gm}} = \frac{d_{\mathrm{A}} d_{\mathrm{B}}}{((d_{\mathrm{A}} - d_{\mathrm{B}})^2 + d_{\mathrm{A}} d_{\mathrm{B}} \beta^2)}, \tag{2.80}$$

where d_{A} and d_{B} is the spacing in grain A and B, and β the tilt angle required to bring A into the same orientation as B.

Selected Area Diffraction (SAD)

A diffraction technique frequently used in TEM is Selected Area Diffraction (SAD). This is performed by inserting a selected-area aperture in the first image plane, limiting the diffraction pattern to a confine an area of typically $1-10\ \mu$m. The intermediate lenses are adjusted so that the back focal plane is in focus rather than the imaging plane. Each diffraction spot corresponds to a plane in the real crystal and the interplanar spacing may be obtained according to:

$$d = \frac{\lambda L}{R}, \tag{2.81}$$

where the product λL is called the camera constant and R is the measured distance between the central beam spot and the diffracted beam. One may then index the diffraction pattern with their corresponding **g** vector according to the d-values, and after two have

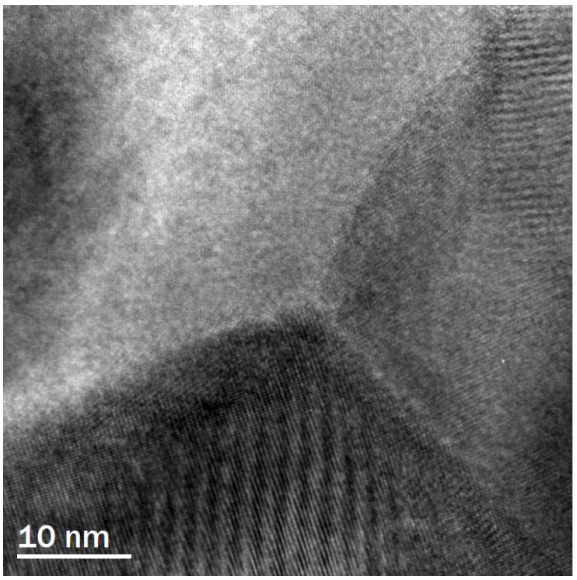

Figure 2.11: HRTEM micrograph of a triple point in BZY10, revealing both lattice fringes and Moiré patterns.

been indexed the rest may be obtained using simple vector addition. The zone axis, as mentioned earlier, is then determined from the cross product of two **g** vectors.

$$\mathrm{ZA} = \mathbf{g}_1 \times \mathbf{g}_2 = \begin{vmatrix} U & V & W \\ h_1 & k_1 & l_1 \\ h_2 & k_2 & l_2 \end{vmatrix} \tag{2.82}$$

Scanning Transmission Electron (STEM)

In STEM mode the sample is illuminated by a well converged electron beam, which scans the area pixel by pixel. The signals are detected by annular detectors situated below the sample at different angles from the optical axis. Unscattered electrons, and in some cases signals from atoms scattering to low angles from the optical axis, are detected by the Annular Bright Field (ABF) detector. Electrons scattered further away from the optical axis is detected by the Annular Dark Field (ADF) and the High-Angle Annular Dark Field (HAADF) detectors. The contrast mechanism in HAADF micrographs is primarily due to mass-thickness (Z-contrast), but a combination of this and diffraction contrast may occur in the ADF, depending on the experimental parameters.

Spectroscopic techniques

In addition to the imaging techniques described above, one may perform spectroscopic experiments to gain chemical information of the material. There are two main techniques used in a TEM:

1. In EDS a X-ray spectrum is acquired from a region limited by the probe size. Each chemical element has characteristic X-rays corresponding to transition between discrete atomic energy levels. These are used to determine the chemical composition of the area. In STEM mode one may create chemical maps from the X-ray spectrum obtained from each pixel.

2. In EELS the energy loss of electrons which have been forward scattered is measured. The inelastic interactions may be due to plasmon excitation, inter- and intraband transitions and core electron ionization. It may be used to determine the chemical composition in an area, but also to obtain information on the local bonding environment, dielectric properties, bandgap properties and more.

There are still many other techniques one may utilize in the TEM which are not mentioned here. Even today, the instrument is still being developed for new techniques and this is one of the reasons the TEM is one of the most interesting instruments of our century.

Chapter 3

Literature

Since their discovery by Iwahara *et al.* in the early 1980s, solid oxide proton-conductors have been among the most studied materials for electrochemical applications such as fuel cells, sensors and electrochemical reactors [7, 8]. This section summarizes some the research conducted in the last two decades with respect to BZY.

3.1 Background

Even though there has been some research on other proton conducting materials such as rare earth ortho-niobates and ortho-tantalates [38], and in more complex perovskite structures such as $(La_{0.5}Sr_{0.5})(Mg_{0.5+y}Nb_{0.5-y})O_3$ [39], most studies have been towards the perovskites: $BaZrO_3$ and $BaCeO_3$. This due to their high proton conductivity peaking above 10^{-2} Scm^{-1} [7, 40]. In a study conducted by Norby & Larring, proton conductivity was calculated based on proton concentration and mobilities. This indicated that 10 mol% Y-doped $BaZrO_3$ (BZY10) has higher proton conductivity than BCY10, as shown in figure 3.1 [9]. Generally $BaCeO_3$ and $BaZrO_3$ based materials exhibit larger proton conductivity than $SrCeO_3$ based materials. This may be since $BaCeO_3$ has the largest lattice parameter and the smallest distortion from the ideal perovskite structure; two important parameters for proton conductivity [7].
A drawback with $SrCeO_3$and $BaCeO_3$ is their low chemical stability due to degradation when exposed to acidic CO_3 and water vapour, making them unattractive for use in fuel cells in which the fuel is hydrocarbons [7, 41–43]. On the other hand, BZY shows excellent chemical stability, but its total proton conductivity is generally about 1 order of magnitude lower than that of $BaCeO_3$ (10^{-2} Scm^{-1} vs. 10^{-1} Scm^{-1}) at 600 °C [7]. This is attributed to the materials poor ability to sinter, yielding small average grain size and thus high areas of highly resistive grain boundaries. Nonetheless, since BZY in

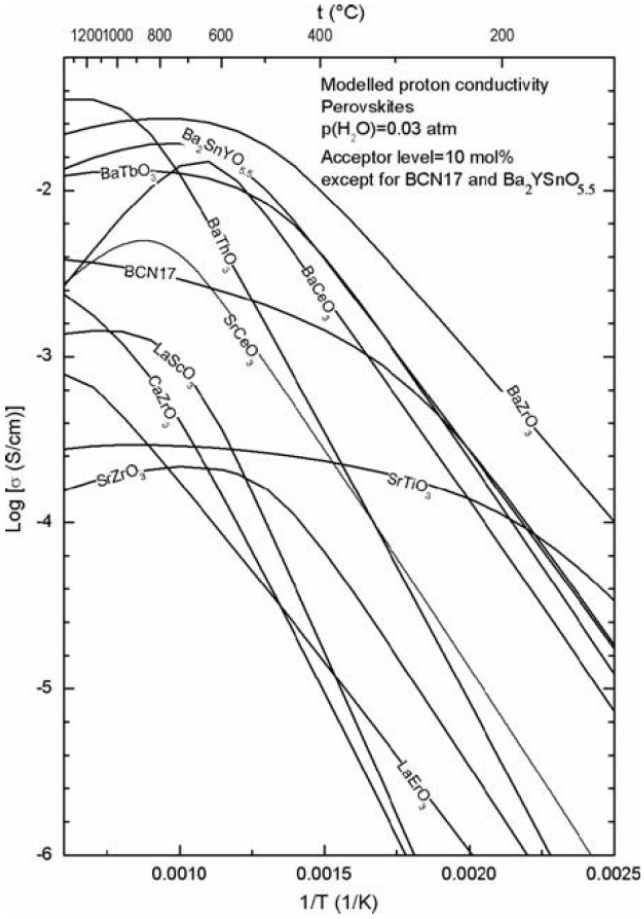

Figure 3.1: Partial proton conductivity (bulk) of various oxides calculated on basis of proton mobility and parameters from hydration thermodynamics [9]. Figure is reproduced from [5].

theory has higher bulk conductivity than BCY, a lot of research effort is directed towards establishing new synthesis routes and doping strategies to increase the grain boundary conductivity by enhancing the grain growth and thus lowering the overall grain boundary volume.

3.2 Synthesis

3.2.1 Different methods and sintering conditions

The most common method for synthesizing BZY is through the Solid State Reaction (SSR) method. Starting materials are usually high purity $BaCO_3$, Y_2O_3 and ZrO_2, which are measured out in stoichiometric values, followed by several steps of milling and cal-

cination [3]. High temperature annealing at temperatures above 1400 °C leads to the formation of the single phase perovskite.

This straightforward method has some major drawbacks. High temperature annealing usually leads to powders with large particle sizes and a wide spread in particle sizes. These conditions give powders which are difficult to sinter, resulting in low-densities and wide spread in the grain size distribution. A highly dense material is a required property of electrolyte membranes. In practice, high sintering temperatures, usually above 1700 °C, are required to obtain dense pellets. The effect of even higher annealing temperatures has been studied by Duval *et al.*, where they showed that the grain boundary conductivity could be increased by up to 2 orders of magnitude for a sample annealed at 2200 °C, as compared to a sample sintered at 1720 °C. The bulk conductivity, however, remained the same. This result reveals that high temperature sintering helps BZY grain growth and also improves the grain conductivity [10].

It has been shown that prolonged annealing results in BaO evaporation. Iguchi *et al.* demonstrated effects of this by sintering two BZY5 samples at 1800 °C; one for 20 h and the other for 200 h [44]. After sintering, the outer surface appeared dark green and was a Ba poor region which was mechanically removed. The pellets were further subjected to electrical measurement tests where it was shown that the sample annealed for 20 h had higher bulk- and grain boundary conductivity than the 200 h one, as shown in figure 3.2. This result was surprising since there were no differences in the grain microstructure and grain boundary characteristics of the two pellets, and that the average grain size was larger for the 200 h sample (1.61 μm against 0.67 μm). This result show that sintering parameters such as temperature and time have a strong influence on the conductivity properties. The effect of Ba deficiency during sintering was further studied by Babilo *et al.*, where a BZY20 pellet was surrounded by a mixture of BZY20 and $BaCO_3$ during the sintering step, and one without as reference [23]. Their results showed that highly dense samples with high conductivity values could be obtained if the particle size of the starting powder was less than 100 nm. However, the pellet sintered without coverage resulted in Ba deficiency and a reduction by 2 orders of magnitude in the total conductivity, as compared to the other pellet. The uncovered sample also displayed an Y_2O_3 like precipitate, which was also observed by Magrez & Schober [22].

Dahl *et al.* showed that sintering BZY10 under pressure (hot-pressing), yield densities up to $\sim$98% when sintered at 1700 °C under a pressure of 50 MPa [45]. Sintering at 1500 °C under 25 MPa for 1 h yielded $\sim$89% density, while sintering at 6 h under no pressure at 1600 °C yielded $\sim$74%. Hot pressing thus increased the densification rate and resulted in a homogenous microstructure.

Wet chemical synthesis routes have also been studied. This usually consist of mixing metal precursors in a solvent, yielding a uniform particle size of the powder, making it

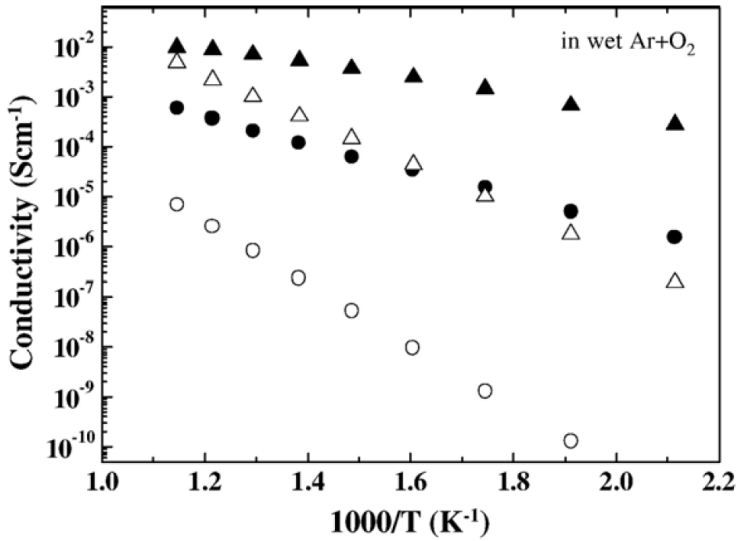

Figure 3.2: Proton conductivity for BZY5 samples in wet air + Ar with partial pressure of P_{H_2O} = 2.3 kPa. The triangles, ▲, and circles, ●, represents samples sintered for 20 and 200 hours, respectively. Open symbols indicate grain boundary conduction. Figure reproduced from [44].

easier to sinter at lower temperatures [42]. There are of course many different ways of conducting a wet chemical synthesis method for BZY, but these will not be discussed further here.

A synthesis route fairly similar to SSR is Solid State Reactive Sintering (SSRS), in which all is similar up to the calcination. Instead of performing one or more steps of calcination, SSRS consists of a one-time temperature treatment technique [46, 47]. This was studied by Ricote *et al.*, and compared to other synthesis routes [48]. Their results showed that the sample prepared by SSRS at 1550 °C had the highest total conductivity. Thus, this method may be the quickest and most effective for preparing dense samples at present.

3.2.2 The effect of sintering aids

Improved sintering, by the addition of small amounts of metal ions called sintering aids, occurs when: i) the additive reacts with the material and forms a liquid phase, or ii) becomes soluble in the material in different extents. The first is called a liquid phase sintering, whilst the latter is the solid solution approach. Some sintering aids have shown to give highly dense samples under significantly lower sintering temperatures (1300 °C) than what is typically obtained without sintering aids. However, it has some major drawbacks; the total conductivity is often reduced to their non-additive counterparts,

and formation of secondary phases and cation accumulation in the grain boundaries has been observed [42, 49].
Duval *et al.* tested how TiO_2, MgO, Mo, Al_2O_3 and Bi_2O_3 additives influenced the microstructure and conductivity properties of [50]. These additives had no effect on the sintering properties and mostly resulted in less dense samples. The lattice parameter was in most cases also reduced, and the conductivity reduced by up to 3 orders of magnitude for 1 mol% TiO_2. The conclusion was that these additives are not suitable for BZY and that the lattice parameter is closely correlated to activation energy and conduction, where a larger lattice parameter gives lower activation energy and higher total conductivity.
The effect of using transition metals as additives was studied by Babilo & Haile [51]. They showed that only Ni, Cu and Zn had a positive effect on the densification of BZY. ZnO was further studied and showed enhanced grain growth resulting in dense samples (93%) at only 1300 °C. However, the bulk conductivity was lower than for their Zn-free counterparts and Zn was found to accumulate in the grain boundaries, but seemed to have no effect on the grain boundary conductivity. The low conductivity in the grain interior was attributed to proton trapping around Zn''_{Zr} defects formed during sintering.
A study of using $LiNO_3$ was conducted by Sun *et al.* [52], and resulted in a higher total conductivity ($4.45{\cdot}10^{-3}$ Scm^{-1} at 600 °C) than what was reported for ZnO and CuO for a BZY20 compound. These improved characteristics were the result of a complete evaporation of the Li additive during sintering, and thus Li clean grain boundaries and grain interiors.

3.3 Grain boundaries

3.3.1 Measurements

Space-charge theory has been studied in oxide ion conductors before, by e.g. Guo & Waser [53], who studied yttrium-doped zirconia and ceria. Their conclusion was that oxygen vacancies are enriched in the grain boundary core: yielding a net positive charge. Acceptor dopant accumulation in the adjacent space-charge regions compensates this positive charge. The use of Auger Electron Spectroscopy (AES), EELS, EDS and XPS has shown that the cation accumulation usually occurs within 2-4 nm from the grain boundary core in ZrO_2 [54–57].
The studies conducted on grain boundaries in BZY by Iguchi *et al.*, show that proton migration across the grain boundaries is sensitive to the concentration of the charged defects in the space-charge area [44, 58, 59]. Proton conductivity was measured for BZY doped with 5 to 15 mol% prepared at various temperatures, and their microstructural differences studied. Grain boundary conductivity increased with increasing yttrium content

and the activation energy decreased similarly. This could not be explained in terms of average grain size diameter, the grain boundary characteristics or the formation of secondary phases. This indicated that the grain boundary conduction is dependent on the presence of charged defects, such as barium vacancies ($v_{Ba}^{\bullet\bullet}$) and Y substituted on Zr site (Y'_{Zr}). The contribution by Iguchi *et al.* are the first reports introducing an electrically charged grain boundary in BZY.

Another observation by Iguchi *et al.* is on the grain structure and its influence on the conductivity. They found that the grain boundaries mostly adapts random orientations, determined by Electron Backscatter Diffraction (EBSD) in a Scanning Electron Microscopy (SEM) [44, 59]. They used the CSL scheme and the tolerance for low-angle grain boundaries was defined by the *Brandon criterion*. The results are shown in figure 3.3.

Space-charge theory was applied to BZY10 by Kjølseth *et al.* [24]. Specific grain boundary conductivities were obtained from two samples: one made by hot-pressing and one by spark-plasma sintering. Higher proton conductivities were measured in grain interior than in grain boundaries. EDS analysis in TEM with a 5 nm spot showed a higher Y to Zr ratio in the grain boundary areas, indicating that Y segregates close to the grain boundaries. A similar behaviour was observed by Dahl *et al.* [45]. The negatively charged defect Y'_{Zr} fits with the overall picture that the space-charge region is compensated by negatively charged defects, making accumulation of yttrium in this zone likely. By calculating the Schottky barrier height it was shown that a higher doping concentra-

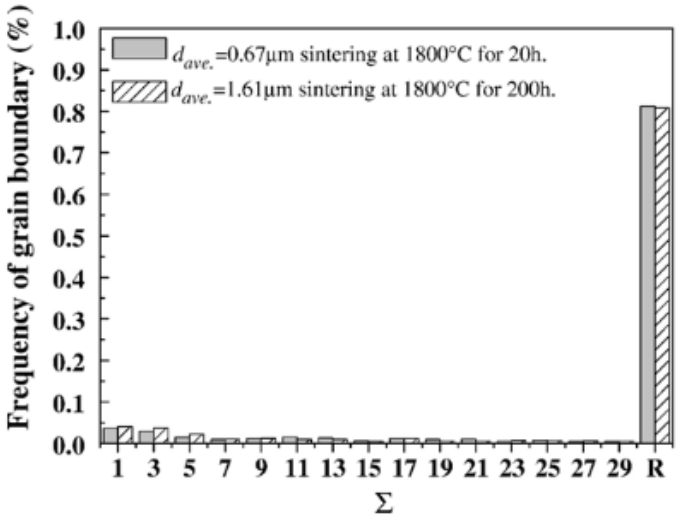

Figure 3.3: Grain boundary character distribution, as obtained from EBSD. The CSL number is counted to 29, and everything above is summed as random, R. Figure reproduced from [44].

tion of Y would lead to a lower barrier, which in turn would mean that a higher doping concentration should yield higher grain boundary conductivity. The BZY20 sample prepared by Babilo *et al.*, and the results by Iguchi *et al.*, supports this; as it has a higher grain boundary conductivity than the two samples in the paper by Kjølseth [23, 59]. However, the high temperature sample prepared by Duval *et al.* has even higher grain boundary conductivity than the BZY20 sample. The conclusion they drew from this was that the high temperature annealing lead to structural- and/or compositional changes in the grain boundaries. This would change the nature of the space-charge region and also the proton concentration and conductivity. The potential of the core was thought to have levelled out with respect to the grain interior potential due to cation and dopant redistribution at high temperatures. A comparison of the conductivities is shown in figure 3.4. The overall conclusion from this section is that a space-charge layer exists and strongly influences the grain boundary resistance in $BaZrO_3$.

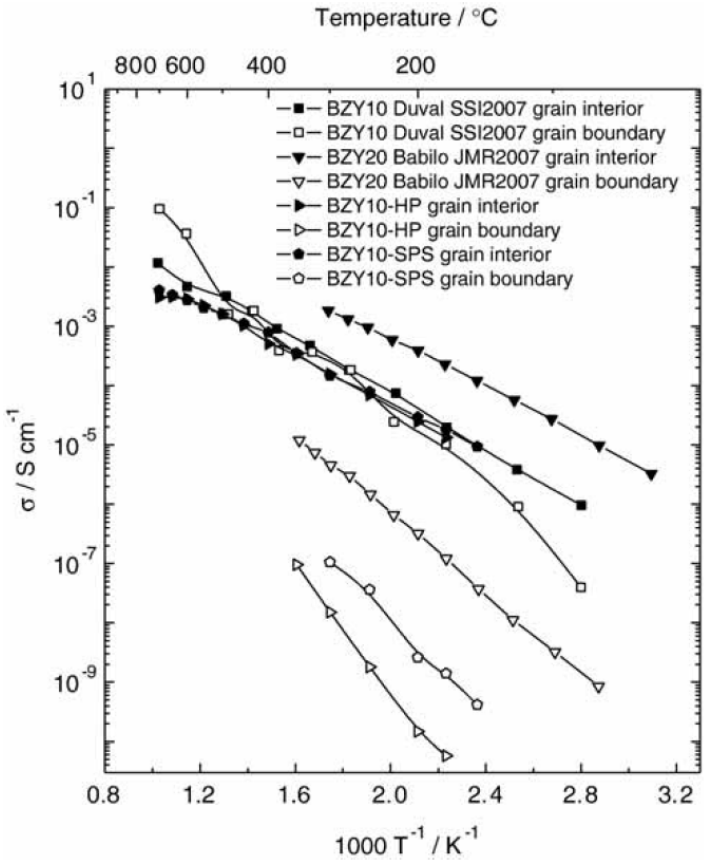

Figure 3.4: Specific grain interior and grain boundary conductivity plotted vs. the inverse temperature. Figure is from [24] and the HP and SPS data are from this paper. BZY10 by Duval *et al.* is annealed at 2220 °C [10]. BZY20 data is from Babilo *et al.* [23].

3.3.2 Transmission Electron Microscopy (TEM)

There is, to the author's knowledge, a limited amounted of literature specific to BZY, in which extensive TEM work has been performed. Generally, TEM images have been added to other papers to show the grain microstructure, indicate interfaces free of secondary phases or show composition from EDS measurements. However, Shirpour *et al*. published a paper in which cation concentration and space-charge effects of Y- and Sc-doped $BaZrO_3$ were discussed [60]. The effect of cation accumulation after annealing a sample prepared by Spark Plasma Sintering (SPS) was studied, by combining TEM and impedance spectroscopy. Annealing for 20 h at 1700 °C gave no change in grain size and bulk conductivity, but for the GB it increased significantly. Accumulation of Y (and Sc) was observed by performing TEM-EDS before and after annealing. Averaging 15 sites made the GB mean value of [Y]/([Y]+[Zr]) ratio increase from 0.068 to 0.187 while the bulk value remained the same. The correlation between the electrical properties of GBs and their chemical composition is compatible with the discussion of space-charge theory. A similar behaviour was also observed in Sc-doped $BaZrO_3$, and also from EELS experiments [61].

3.4 Computational results

Due to the difficulties with the material on a microstructural level a significant amount of calculations have been performed in order to understand the defect segregation effect, as well as fundamental thermodynamics.

$BaZrO_3$

The thermodynamics of doping and oxygen vacancy formation in $BaZrO_3$ was studied by Sundell *et al*. [62]. By combining DFT calculations and thermodynamic modelling the formation energies for acceptor dopants Ga, Gd, In, Nd, Sc and Y were reported for different charge states and under different environmental conditions. Most dopants would occupy Zr site, except for the larger ones such as Gd and Nd, which may partly occupy the Ba site. Furthermore, dopant-dopant interaction was found to be repulsive and with strength following the ionic size of the dopant, whilst the dopant-oxygen vacancy was found to be attractive. The oxygen vacancies were found not to be thermodynamically stable at low temperatures and thus become a charge compensating defect at elevated temperatures and low p_{O_2}. The reported formation energies, ΔE^{f}, for $\nu_O^{\bullet\bullet}$ is 1.21 eV using a 3×3×3 supercell.
The proton migration properties were further studied by the same group in [63, 64]. In

the first paper the proton migration pathway is analysed when the Zr site is substituted by Ga, Sc, In, Y and Gd. In all cases the interaction was found positive and increasing with lower dopant radius, since the smaller dopants allow for larger OH tilting and the shortest O-H bonds. Far from the defect, the activation energy was found to be 0.2 eV, about half the value of experimental values. Close to the dopant the values increased by more than 0.15 eV, suggesting that these act as trapping centres. The larger dopants also influence protons situated at the next neighbouring O atoms.

Grain boundaries

The group of Göran Wahnström has studied the segregation and space-charge behaviour for a range of grain boundaries [65–68]. Helgee studied three tilt boundaries: 70.53°(112)[$\bar{1}$10], 109.47°(111)[$\bar{1}$10] and 53.24°(210)[001], and reported that both $\nu_O^{\bullet\bullet}$ and $OH_O^{\bullet}$ segregate to the core. The proton's stability increases on sites where vacancies also were more stable, in the two latter grain boundaries. The minimum $\nu_O^{\bullet\bullet}$ segregation energy was found to be -1.5 eV for the first boundary and -0.5 eV for the two latter. For all three, the minimum proton segregation energy was approximately -0.8 eV. Space-charge modelling showed that all GBs become hydrated at lower temperatures, and for the two latter GBs protons gave the dominant contribution to the core charge in the temperature range 300 to 1800 K, while $\nu_O^{\bullet\bullet}$ dominated in the (112) GB above 800 K. Under dry and wet conditions the barriers remain the same in (112), while in the two other the barrier is around 0.4 eV lower under wet conditions.
Lindman studied $\nu_O^{\bullet\bullet}$ segregation in (11k)[$\bar{1}$10] where k = 1,..., 8, using interatomic pair potentials [67]. The segregation energies were slightly larger for the same boundaries as Helgee studied. In (111) and (112), all vacancy sites that favoured segregation corresponded to the site of minimum segregation energy; whilst it for all others existed a range of possible sites with different segregation energies. This is illustrated in figure 3.5.
Polfus *et al*. studied the Σ3(111)[$\bar{1}$10] grain boundary and reported segregation energies of -0.81, -0.65 and 0.11 eV for $OH_O^{\bullet}$, $\nu_O^{\bullet\bullet}$ and Y'_{Zr}, respectively [69]. Schottky barriers of 0.51 V and 0.28 V were obtained for fully hydrated and dehydrated core at 573 K. Helgee reported $\sim$0.6 V for the same hydrated grain boundary at 600 K. The energy barrier for proton migration across the same boundary was studied by Yang *et al*. using climbing image nudged elastic band (CL-NEB) as implemented in VASP [70]. The value for bulk energy migration barrier was reported to 0.18-0.25 eV, while the grain boundary had 0.71-0.95 eV and 0.88-1.08 eV for one and three protons respectively.

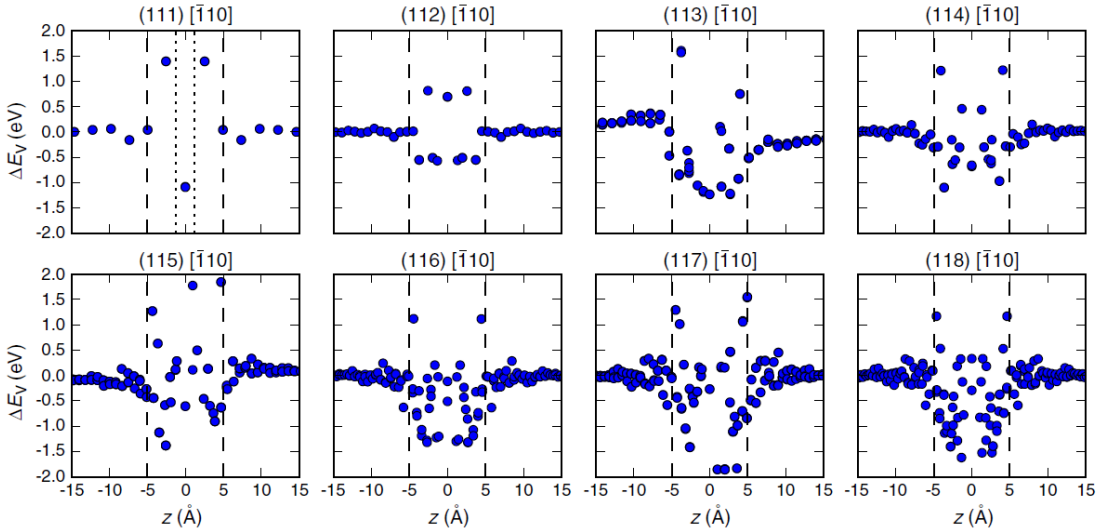

Figure 3.5: Oxygen vacancy segregation energies for all sites within 15 Å from the core. Dashed lines marks a core width of 10 Å, whilst the dotted line in (111) represents a width of 2.5 Å. Figure reproduced from [67].

Chapter 4

Experimental methods

4.1 Samples

A piece of the BZY10 sample made by Sophie Duval at 2200 °C was obtained and is further referred to as BZY10-HT [10]. Samples for comparison were prepared through the SSR method in-house. Three batches were sintered separately and is further referred to as BZY10-1, BZY10-2 and BZY10-3-1/2. In the last batch two samples were sintered simultaneously.
Furthermore, two BZY15 samples were prepared by Nahum M. Carcases through the SSRS method from $BaCO_3$ and Y_2O_3, with 1 wt.% NiO [71]. These are further referred to as BZY15-BaEx and BZY15-BaDef, as they were prepared with a non-stoichiometry of Ba of 1.02 and 0.98, respectively.

4.1.1 Preparation of BZY10

BZY10 was prepared from the starting materials listed in table 4.1 and processed in the following manner.

1. Powders were dried for 2 hours at 200 °C before stoichiometric amounts of each precursor were weighted out and mixed in a rotary ball mill with isopropanol and Calcia-Stabilized Zirconia (CSZ) balls of 1 cm diameter, for 3 hours.

2. The powder was dried at 120 °C until all isopropanol had evaporated, thereafter mixed in an agate mortar along with a binder (B60+B72 acryloids dissolved in etylacetat) and uniaxially pressed into two 20 mm discs at 125 MPa. The pellets were placed in an alumina crucible and calcined at 1200 °C for 10 hours with ramp rates of 5 °C/min.

3. The pellets were again crushed and milled in the rotary mill with *no medium* for 2 days. Isopropanol was used to remove the powder from the balls and the tube walls. Thereafter, the powder was again dried, pressed into 20 mm discs under 125 MPa and calcined at 1400 °C for 10 hours.

4. Lastly, the pellets were crushed and ball milled in a planetary ball mill for 3 hours at 200 rpm, using ZrO_2 balls with 3 mm diameter in isopropanol and dried overnight. Pellets were prepared with a 13 mm diameter die under a pressure of 200 MPa, before sintering at 1700 °C for 5 hours in an Al_2O_3 crucible with "sacrificial" BZY10 powder.

Table 4.1: Precursor materials used in the synthesis.

Material	Purity and size	Supplier
Y_2O_3	99.9%, <10 micron powder	Alfa Aesar CAS nr. 1314-36-9
ZrO_2	99.7%, <325 mesh powder	Alfa Aesar CAS nr. 1312-23-4
$BaCO_3$	99.8%, 1 micron powder	Alfa Aesar CAS nr. 513-77-9

4.2 X-Ray Diffraction (XRD)

Phase analysis of powders and pellets were done through XRD on a Siemens Bruker D8 Discover, with Bragg-Brentano geometry and Cu $K_{\alpha,1}$ radiation (λ = 1.5046 Å). Scans were performed in the range $10° \leq 2\theta \leq 120°$ with a step of 0.02 °/s. Diffractograms were processed using DIFFRAC.EVA and Topas, in which they were indexed, refined and compared with the Powder Diffraction File (PDF) database by the International Centre for Diffraction Data (ICDD). A Si standard (NIST 640D) was added to the powder XRD samples.

4.3 Scanning Electron Microscopy (SEM)

The FEI-SEM (FEI quanta 200 FEG-ESEM), with a BSE detector and a Everhart-Thornley (E-T) detector for secondary electrons (SE), has been used. It is coupled with an EDAX Pegasus 2200 EDS detector, a phosphorescence screen for EBSD and has the possibility to perform heating. It was normally operated in high vacuum mode with an

acceleration voltage of 20 kV. This instrument was used when studying the microstructure of all sintered pellets and when performing EBSD. The HR-SEM (HITACHI UHR FE-SEM SU8200) with a cold FE electron source, filtering system, deceleration mode, three SE detectors and one BSE detector was used to resolve the pre-sintered powder only.
All pellets were washed with ethanol and mounted on carbon tape on an Al stub. The powders were simply sprinkled onto the carbon tape.

4.3.1 Electron Backscatter Diffraction (EBSD)

EBSD is a powerful tool used to determine the orientation of individual grains. Diffraction patterns, which emerge as electrons are scattered by the lattice planes in the sampled volume of the specimen, are utilized. For each set of lattice planes electrons are diffracted to the corresponding Bragg angle θ_B, forming pairs of *Kossel-Cones*, since diffraction happens simultaneously in all directions. A phosphorescence screen detects a section of the cone, resulting in nearly parallel lines called *Kikuchi lines*. These lines have an angular distance of $2\theta_B$ and will naturally correspond to different planes. A full description may be found elsewhere [17, 72]. EBSD signals were detected using the Orientation Imaging Microscopy™ (OLM) system, as described by Adams *et al*. [73]. A step size of 0.03 μm was used over an area sufficient to produce enough statistics. The data were analysed in the OLM software which provide statistics on Grain Boundary Character Distribution (GBCD).

4.3.2 Density and grain size evaluation

Bulk densities of pellets were determined from sample geometry through the formula:

$$\rho = \frac{m}{A \cdot h}, \tag{4.1}$$

where A is the surface area of the pellet, h the height and m the mass. The relative density is then found by comparing with a theoretical value obtained through the lattice parameter from XRD.
From SEM micrographs the grain size distribution is analysed using a line intersection method implement in the MATLAB program "Linecut" [74]. The basic principle is to draw a set of lines and indicate the grain boundaries on the line. A proportionality factor describing the shape of grain in a non-textured compacted powder is introduced. As a first: approximation spherical grains are assumed, but may be extended to complex shapes such as tetrakaidecahedrons, as described by Mendelson [75].

4.4 Transmission Electron Microscopy (TEM)

The main instrument used in this study is the JEOL JEM-2100F, equipped with an ultra-high resolution pole piece giving a point resolution of 1.9 Å. It is operated at an acceleration voltage of 200 kV and the gun is a Schottky FEG. EDS spectra were acquired by an Oxford instrument Silicon Drift Detector (SDD) and images captured on a CCD by Gatan.
High resolution STEM images are acquired on a FEI TITAN G2 60-300 instrument. It has an ultra-high brightness XFEG, wien filter monochromator and is quipped with a spherical aberration corrector giving a point resolution of 0.8 Å. The EDS is collected on FEI's chemiSTEM system and EELS on the Gatan Quantum 965 energy filter.

4.4.1 Sample preparation

All TEM samples were prepared as wedges by mechanical grinding. Initially by rough grinding on SiC to obtain a uniform thickness of 150-200 μm. Further thinning was performed on a MultiPrep^{TM}, using diamond lapping films with particle sizes from 30 to 1 μm. The final thinning by ion milling was performed on either Fischione (model 1010) or Gatan PIPS (model 691 or PIPS II), usually with angles 7° (top) and 6° (bottom) at 5 kV and a round with all the previous values one lower. All samples were mounted on Cu O-ring using glue from the Gatan cross-sectional kit (MODEL 601.07).
For STEM experiments the samples were first plasma cleaned using the Fischione model 1010 plasma cleaner.

4.4.2 Goniometer tilt angle

For each grain boundary the diffraction pattern of each adjacent grain is obtained after tilting into the closest Zone Axis (ZA). The net tilt angle ϕ_{net} between the two ZA is then found by the two tilt angles of the goniometer α and β according to:

$$\begin{aligned}\phi_{\text{net}} = \cos^{-1}(&\cos(\beta_1 - \beta_2)\cos(\alpha_2 - \alpha_2) \\ &+ 2\sin\beta_1 \sin\beta_2 \sin^2 1/2\,(\alpha_2 - \alpha_1)),\end{aligned} \tag{4.2}$$

where the subscripts 1 and 2 correspond to the goniometer values before and after tilting [76].

4.4.3 Energy-Dispersive Spectroscopy (EDS)

TEM-EDS was performed with a spotsize of 2 nm. All measurements were taken as close to the edge as possible to neglect thickness effects, such as absorption and overlapping grains. The instrument has been calibrated to theoretical values of Si and the following -factors have been used k_O = 1.999, k_{Ni} = 1.192, k_{Zr} = 3.575, k_Y = 3.086 and k_{Ba} = 2.062. Quantification was performed using O, Ni, Zr and Y *K*-edges and the Ba *L*-edge. A typical EDS spectrum, before and after peak identification and quantification, is presented in appendix B.

4.5 Electrical measurements

4.5.1 Setup

Measurment cell

The measurment cell used was a Probostat^{TM} manufactured by NorECs AS [77]. A sample is sandwiched between two Pt electrodes, supported on an inside, open, alumina tube and positioned by a spring load alumina assembly. A closed outside alumina tube is connected to the stainless steel base and covers the entire setup. Temperature is measured with a S-type thermocouple positioned next to the sample and is connected to a temperature controller regulating the furnace temperature. The ProboStat^{TM} is further placed vertically into a tubular furnace, with the sample located in the centre.

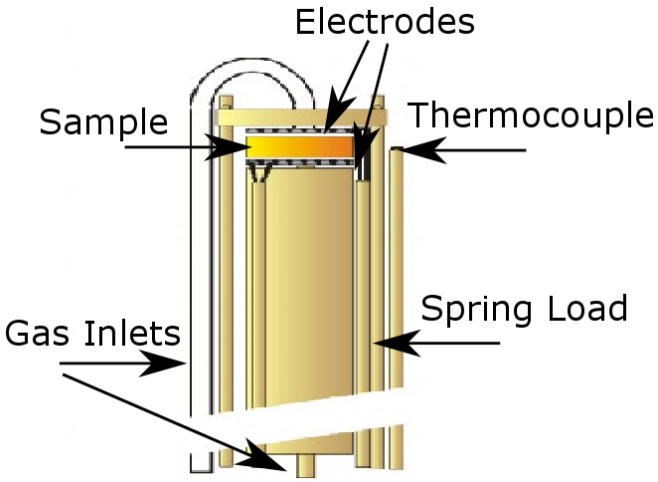

Figure 4.1: Schematic figure of the measurement cell showing how the sample is situated with respect to the other components. Figure modified from NorECs [77].

Gas mixer

A gas mixer was used in order to control the atmosphere surrounding the sample. This allows two gasses (G1, G2) to be mixed by diluting G1 with G2 to form a mix 1 (M1). M1 may then be further diluted with G2 in two more diluting stages. Humidification (wetting) is done with deionized water (or D_2O) and bubbling it through a saturated solution of KBr at room temperature. Parallel to this is a drying stage, in which the gas is passed through phosphorous pentoxide (P_2O_5). This setup allows for the gas to be either wet or dry, or the two can be mixed to regulate the water vapour partial pressure. The gas is then fed into Probostat^{TM} and the flow rate controlled by the flow meters.

4.5.2 Sample preparation

The sample measured has a geometrical shape of $\sim$10 mm diameter and 2.5 mm height. The surface of the pellet was covered in a Pt ink without flux (M-001511, METALOR). Three layers of Pt was painted on both sides, with 15 min drying in-between at 100 °C, before a final annealing at 1000 °C for 2 hours.

4.5.3 Experimental

Impedance measurements were performed on a Novocontrol Alpha-A analyser connected with different test interfaces in a 2-point 4-wire setup. Impedances ranging from 10 mΩ to 100 TΩ may be measured using this setup. The measurements in this thesis have an accuracy of 0.2% to 1% for high frequency measurements, according to the specification chart by the supplier.

Measurements series 1

Measurements were conducted every 50 °C, from 100-900 °C under Air, O2, HArMix (5% H_2 in Ar) and Ar in the frequency range 0.1 Hz to 1 MHz on the POT/GAL test interface.

Measurements series 2

Measurements were conducted every 50 °C from 100-400 °C under the same atmospheres as before in the frequency range 0.1 Hz to 20 MHz, using the ZG4 test interface.

4.5.4 Data normalization

The data were fitted using ZView (version 3.4c, Sribner Associates, Inc.). Specific conductivities are reported using formulas:

$$\sigma_{\text{bulk}} = \frac{L}{A}\frac{1}{R_{\text{bulk}}} \tag{4.3}$$

$$\sigma^{\text{sp}}_{\text{GB}} = \frac{L}{A}\left(\frac{C_{\text{bulk}}}{C_{\text{GB}}}\right)\frac{1}{R_{\text{GB}}}. \tag{4.4}$$

4.6 X-ray Photoelectron Spectroscopy (XPS)

XPS was performed on a KRATOS AXIS ULTRA$^{\text{DLD}}$ with monochromatic Al K_α radiation (hν = 1486.6 eV). Vacuum levels during acquisition were in the range of 10^{-9} Torr. The size of the aperture was 700×300 mm. High resolution spectra were acquired using pass energy of 20 eV, dwell time of 500 ms and step size 100 meV. Survey scans were collected with pass energy of 160 eV, dwell time 300 ms and step size 1000 meV. In all spectra charge neutralisation was activated. Peaks used for HR scans were: Ba ($3d_{5/2}/3d_{3/2}$), O 1*s*, Zr ($3d_{5/2}/3d_{3/2}$ & $3p_{3/2}/3p_{1/2}$), C 1*s*, Y ($3d_{5/2}/3d_{3/2}$).

4.6.1 Sample preparation

Samples BZY10-03-01 and BZY10-03-02 were use for XPS scans. The latter was polished using 200-4000 mesh SiC polishing paper, removing ∼0.1 mm of the surface. Both samples were cleaned for 10 minutes in an Ultrasonic Washer with ethanol before wrapped in aluminium foil and stored in a vacuum desecrater. BZY10-03-01 is further referred to as As-rec (As-received) and BZY10-03-02 Polished and Fractured, where XPS was performed on the polished surface prior to the fractured surface.

4.6.2 Peak fitting

All XPS spectra were fitted using appropriate background models in CasaXPS [78], and the Inelastic Mean Free Path (IMFP) were calculated from QUASES [79]. Spectra were all calibrated using the adventitious C 1*s* peak at 284.8 eV, and the peaks: Ba 3*d*, O 1*s*, Zr 3*p* and Y 3*d* were used in the quantification.

4.7 Systematic errors

There are errors associated with every experimental method presented here. Smaller contaminations may stem from all stages used in the sample preparation method used even after extensively cleaning all pieces of equipment used. In the muffle furnaces used temperature gradients exists, although the effect of this has been reduced by placing the pellets in the centre. No bending of pellets due to gradients has been observed.
In the measurement setup gas leakages may exist even though leak tests were performed. The length of wires between the measurement cell and the analyser, were kept to a minimum in order to reduce the contribution of inductance
If applicable, the formulas for error propagation has been applied. This keeps track of error δ_i associated with a quantity i, as basic mathematics operations are performed. The method is shown for addition/subtraction and multiplication/division in equations (4.5) and (4.6).

$$Q = a + b - c \qquad \delta_{tot} = \sqrt{(\delta_a)^2 + (\delta_b)^2 + (\delta_c)^2} \tag{4.5}$$

$$Q = \frac{a \cdot b}{c} \qquad \frac{\delta_{tot}}{|Q|} = \sqrt{\left(\frac{\delta_a}{a}\right)^2 + \left(\frac{\delta_b}{b}\right)^2 + \left(\frac{\delta_c}{c}\right)^2} \tag{4.6}$$

Chapter 5

Computational method

All DFT calculations were performed using the VASP package [30, 31], with GGA by PBE as the exchange-correlation potential [37].
Bulk calculations were performed in a 4×4×4 supercell containing 320 atoms. The grain boundary model has dimensions $\sqrt{6a_0} \times 2\sqrt{a_0} \times 4\sqrt{3a_0}$, and consists of 240 atoms and two grain boundaries separated by 14.72 Å. The supercells are shown in 5.1.

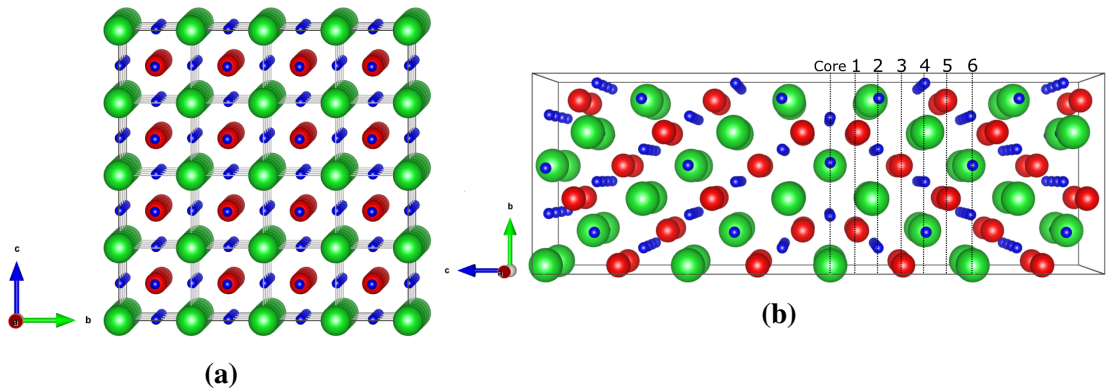

Figure 5.1: Bulk supercell and the grain boundary model in (a) and (b) wherein green, red and blue corresponds to Ba, Zr and O respectively. In (b) the atomic layers from the core is marked 1-6, where the 6th layer marks the half way between the two grain boundaries in the model.

Energy cutoff and k-mesh were set to 500 eV and 1×1×1, i.e. only including the Γ-point, for all calculations, and the energy is converged with an accuracy of 1×10^{-6} eV for the final relaxation. For the oxygen dimer, spin polarization was included in the calculation. Density Of States (DOS) was obtained using a Gaussian function with a smearing width of 0.2 eV. All reported DOS have been adjust so the highest occupied state in the Valence Band Maximum (VBM) is 0 eV.

Potentials

In VASP, the interaction between electrons and nuclei are described either by Psuedopotentials or the Projector-Augmented Wave (PAW) method [32]. Both are "frozen core" approximations as the physical properties of a material is usually determined by the valence electrons. PAW optimises both the computational efficiency of pseudopotential with the accuracy of so called all-electron calculations by reconstructing some of the core electron behaviour [80].

5.1 Modelling of defects in solid materials

The formation energy of an isolated point defect is defined:

$$\Delta E^{\mathrm{f}}_{i,q} = E^{\mathrm{tot}}(\mathrm{def}) - E^{\mathrm{tot}}(\mathrm{perf}) + q(\mu_{\mathrm{e}} + \Delta\nu^{q}) - \sum_{i} \Delta n_i \mu_i, \tag{5.1}$$

where *i* is the defect specie with charge q, $E^{tot}(\mathrm{def})$ and $E^{tot}(\mathrm{perf})$ is the total energy of the system with and without the defect, μ_e is the chemical potential of an electron and $\Delta\nu^q$ is the core alignment term used to compensate for errors associated with charged defects. The last term represents the change in chemical specie Δn_i with corresponding chemical potential μ_i. ϵ_{VBM} is defined as the difference in total energy between a neutral system and a system with charge +1.

$$\epsilon_{\mathrm{VBM}} = E^{\mathrm{tot}}(q=0) - E^{\mathrm{tot}}(q=+1) \tag{5.2}$$

In the grain boundary model the segregation is defined as the difference in formation energy between the "bulk-like" area in layer 6 and a site closer to the core.

$$\Delta E^{\mathrm{seg}}_{i} = \Delta E^{\mathrm{f}}_{i,c} - \Delta E^{\mathrm{f}}_{i,b} \tag{5.3}$$

The chemical potentials are obtained under oxygen rich conditions and for oxygen and water these are:

$$\mu_{\mathrm{O}} = \frac{1}{2} E^{\mathrm{tot}}_{\mathrm{O_2}} \qquad \mu_{\mathrm{H_2O}} = E^{\mathrm{tot}}_{\mathrm{H_2O}}, \tag{5.4}$$

and hydrogen from the equilibrium $\mathrm{H_2} + 1/2\mathrm{O_2} = \mathrm{H_2O}$, as:

$$\mu_{\mathrm{H}} = \frac{1}{2}\mu_{\mathrm{H_2O}} - \mu_{\mathrm{O}}. \tag{5.5}$$

The normalized volumetric chemical expansion coefficient of defect *i* is obtained from:

$$\epsilon_i = \frac{1}{\delta}\left(\frac{V_i}{V_0} - 1\right), \tag{5.6}$$

where V_i and V_0 is the volume between the defective and perfect cell, while δ is the defect concentration in mole fraction [81].
The effective coordination number of an octahedron may be defined as:

$$CN_{\text{eff}} = \sum_i w_i, \tag{5.7}$$

where

$$w_i = \exp\left[1 - \left(\frac{l_{\text{i}}}{l_{\text{av}}}\right)^6\right] \tag{5.8}$$

is the "bond weight" of the i^{th} bond. The weighted average bond l_{av} is defined as:

$$l_{\text{av}} = \frac{\sum_i l_{\text{i}} \exp\left[1 - (l_{\text{i}}/l_{\text{min}})^6\right]}{\sum_i \exp\left[1 - (l_{\text{i}}/l_{\text{min}})^6\right]}, \tag{5.9}$$

where l_{i} is the smallest bond length in the octahedron. This function is implemented in *VESTA* [11].

5.1.1 Errors and limitations

A common drawback of GGA functional is that it underestimates the bandgap. This will result in wrong chemical potential of electrons μ_{e}, which again will result in wrong formation energy for the charge defects. Nevertheless, this error is associated with all the defects calculated and thus the relative difference between defects are comparable. However, the absolute values are, as stated, not correct, but calculated in order to compare with other literature.

Chapter 6

Results

6.1 Phase analysis

Phase analyses have been investigated with both XRD and TEM. All specimens have been investigated with XRD in order to identify phases, determine cell parameters and evaluate phase purity of a large volume with high accuracy. The lattice parameters obtained from XRD and the relative bulk density of all samples are summarised in table 6.1. All the specimens prepared in-house is the same batch up until 1400 °C. After this, pellets were sintered in three different rounds.
During the synthesis described in section 4.1.1, the powders after each calcination temperature and the final pellets were evaluated by XRD. The XRD diffractograms are presented in figure 6.1. Already at 1200 °C peaks corresponding to the BZY10 phase ($Pm\bar{3}m$) are observed. At 1400 °C, shoulders are visible to the left of each peak and after

Table 6.1: A summary of the samples used in this study, with corresponding ID, composition, synthesis method and sintering temperature, density and lattice parameter.

Sample ID	Composition	Synthesis Method	Temperature (°C)	Density (%)	Lattice Parameter (Å)	Comment
BZY10	$BaZr_{0.90}Y_{0.10}O_{3-\delta}$	SSR	1200		4.1880	
BZY10	$BaZr_{0.90}Y_{0.10}O_{3-\delta}$	SSR	1400	67	4.1873/4.2143	
BZY10-1	$BaZr_{0.90}Y_{0.10}O_{3-\delta}$	SSR	1700	89	4.1989/4.2059	
BZY10-2	$BaZr_{0.90}Y_{0.10}O_{3-\delta}$	SSR	1700	n/a	4.2033/4.2181	
BZY10-3-1	$BaZr_{0.90}Y_{0.10}O_{3-\delta}$	SSR	1700	80	4.2012/4.2135	
BZY10-3-2	$BaZr_{0.90}Y_{0.10}O_{3-\delta}$	SSR	1700	81	4.2041/4.2184	
BZY10-HT	$BaZr_{0.90}Y_{0.10}O_{3-\delta}$	SSR + HT annealing	2200	98	4.212	[10]
BZY15-BaEx	$Ba_{1.02}Zr_{0.85}Y_{0.15}O_{3-\delta}$	SSRS	1500	>97	4.210	1 wt.% NiO [71]
BZY15-BaDef	$Ba_{0.98}Zr_{0.85}Y_{0.15}O_{3-\delta}$	SSRS	1500	>97	4.213	1 wt.% NiO [71]

sintering: a similar observation is made on the right side of the BZY10 peak. Indications of one phase with a slight barium deficiency was obtained through *Rietveld refinement* using two cubic phases with space group $Pm\bar{3}m$. Another observation made from XRD on BZY10-1 is that three different lattice parameters are obtained corresponding to the unpolished- and polished surface of the pellet, and the powder after crushing it. Similar broadening/splitting is observed in all sintered pellet diffractograms. The refinement is shown for BZY10-3-2 in appendix C.

In the surface of BZY10-3-1 there are indications of a phase which may correspond to Y_2O_3, marked with black arrows in figure 6.2, but could not be confirmed since not all the peaks corresponding to Y_2O_3 ($Ia\bar{3}$) appeared in the experimental diffractogram. The phase does not appear when performing XRD of the crushed pellet.

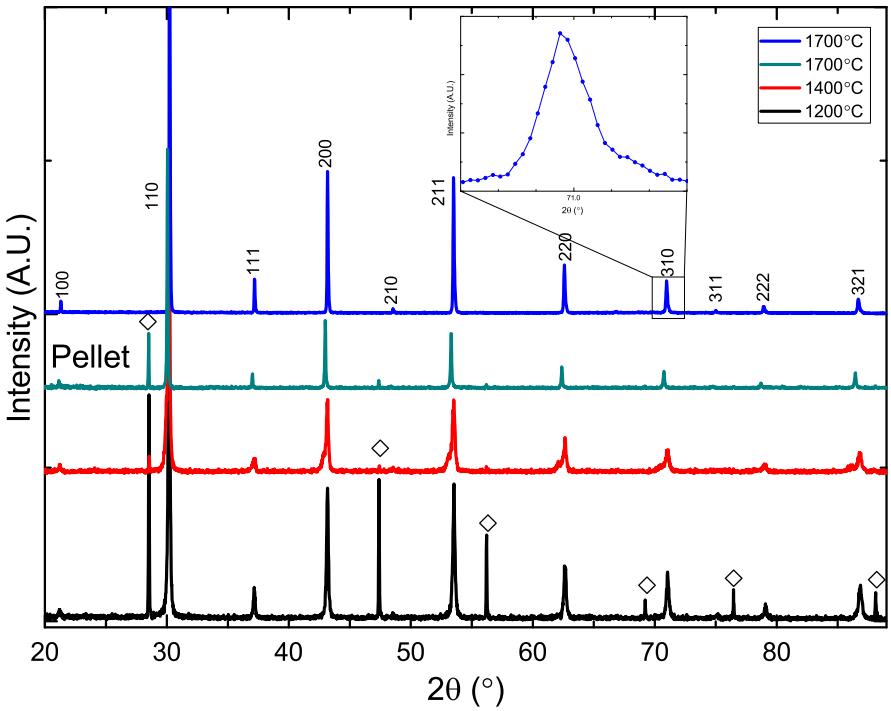

Figure 6.1: XRD diffractograms obtained after heat treating BZY10-1 at 1200, 1400 and 1700 °C. The indexed reflections corresponds to BZY10, while Si reflections are indicated with ◇. The inset figures shows a magnification of the 310 peak; clearly demonstrating a shoulder at the higher angles.

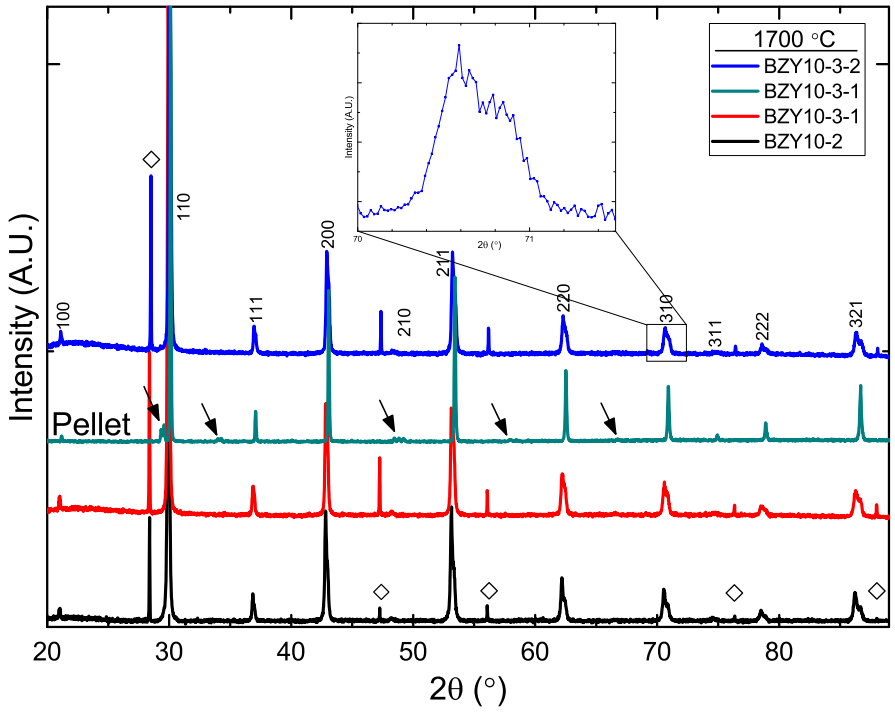

Figure 6.2: Diffractograms for samples BZY10-2 and BZY10-3-1/2. The indexed reflections corresponds to BZY10, while Si reflections are indicated with ◇.

In the TEM, phase analyses on BZY10-2, BZY10-HT and the two BZY15 samples were conducted by SAD and Z-contrast HAADF. All diffraction patterns for these samples fits well with theoretically simulated ones and no discrepancies from the cubic structure, or indications of e.g. superstructures, were observed. Figure 6.3 shows three typical Selected Area Diffraction Pattern (SADP) for low index zone axes.

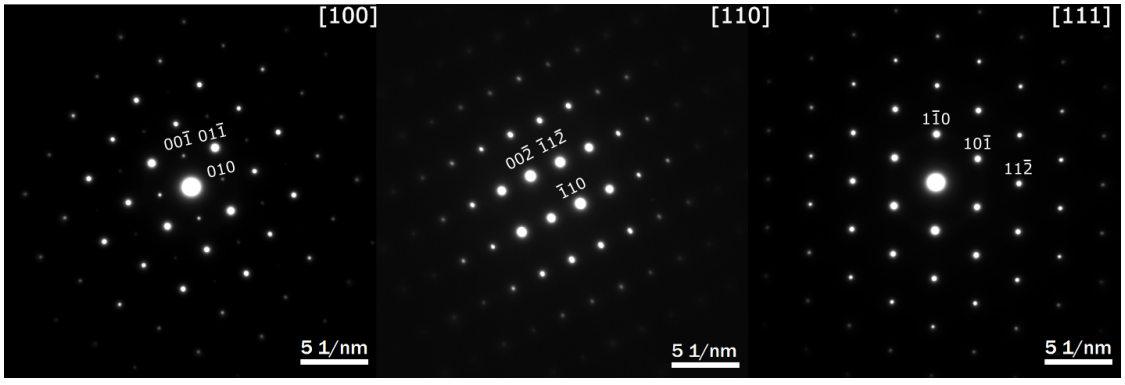

Figure 6.3: SADPs for BZY10-2 oriented along the [100], [110] and [111] zone axis. These are typically the types of SADs obtained for all samples studied by TEM.

No Z-contrast variations were found through HAADF imaging, except for BZY15-BaEx where secondary phase(s) were found to segregate at the grain boundaries and the triple points. This will be presented under the TEM section since the phase(s) are not the size of typical grains.

6.2 Morphology and microstructure

6.2.1 Grain characteristics

SEM was used in order to study the morphology and composition of the samples. Only the HR-SEM was able to resolve the particles of the pre-sintered powder as shown in figure 6.5a. The grains appear smaller than 100 nm after the final calcination step. SEM micrographs of sintered pellets are shown in figure 6.5(c-f). The grain size is significantly larger for BZY-HT than for BZY10-1, as seen in the micrographs and the grain size distribution histogram in figure 6.4.
No secondary phases were observed for BZY10-1, BZY10-2 and BZY10-HT, but appeared in the surface of BZY10-3-1, as was also indicated in the XRD diffractograms. From XRD this was determine to be a Y_2O_3 alike phase, which may have formed due to BaO loss during sintering. The phase was not observed when studying the cross-section as seen in figure 6.6. The latter was done in order to have an idea of what XPS was performed on, as will become apparent in section 6.4.

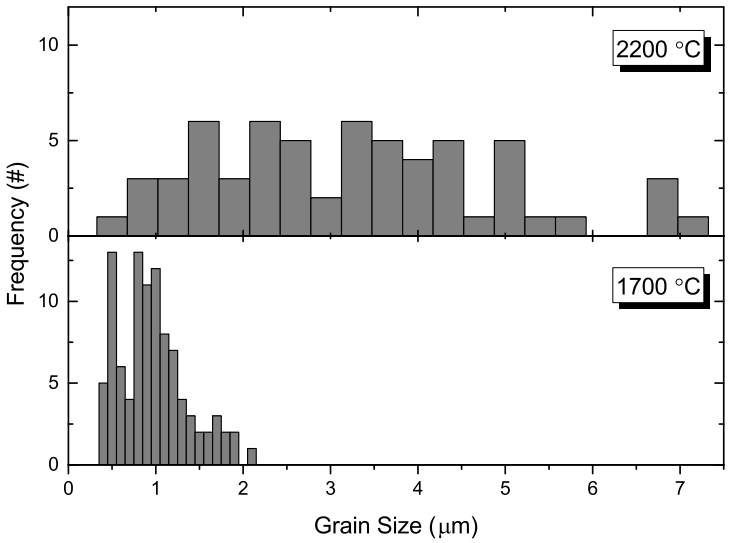

Figure 6.4: Grain size distribution histograms for samples BZY10-HT (above) and BZY10-1 (below), as obtained using the line intersection method on SEM micrographs.

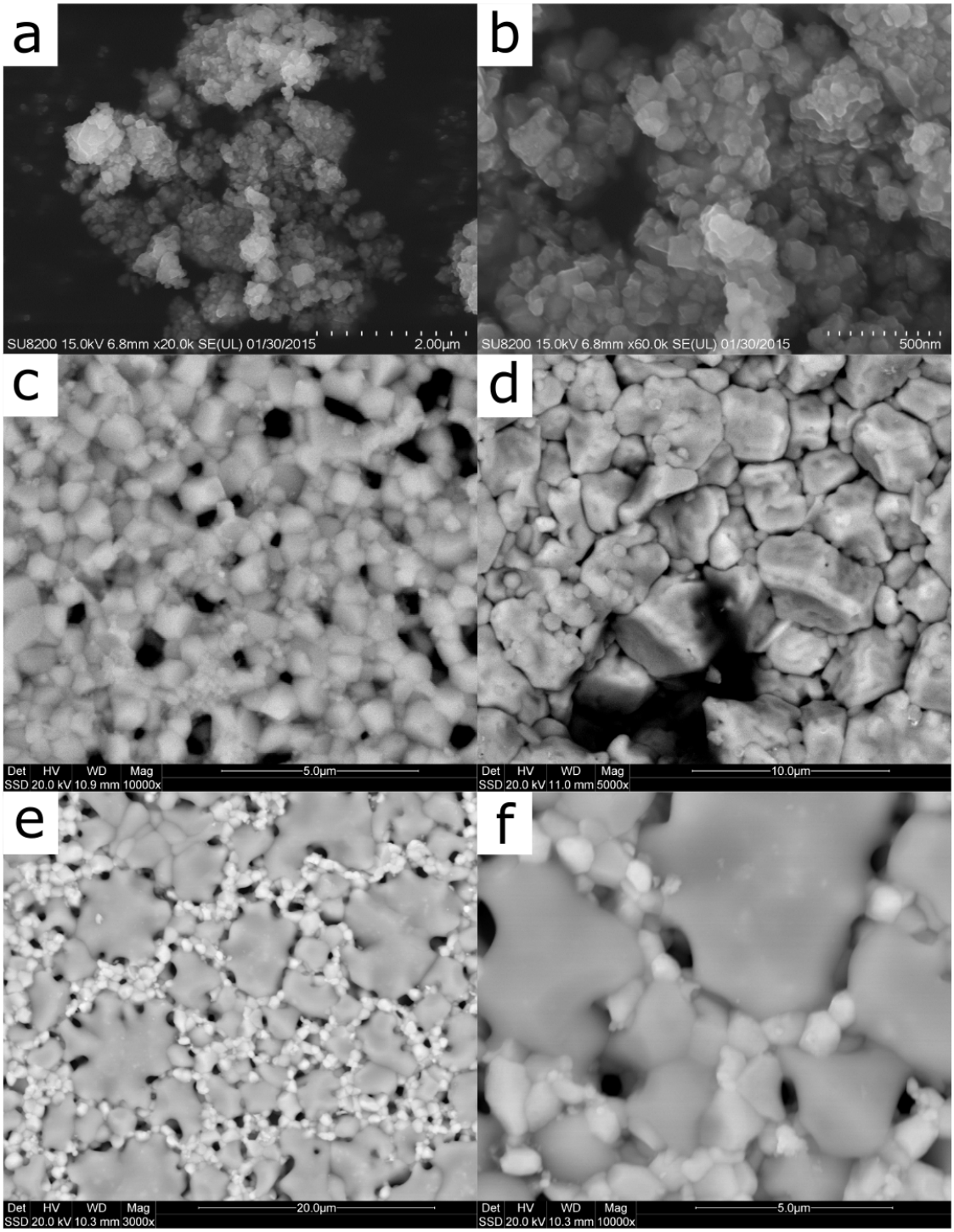

Figure 6.5: (a) and (b) are micrographs of the pre-sintered powder. (c) and (d) are surface micrographs of the BZY10-1 and BZY10-HT pellets, respectively. (e) and (f) is from the surface of BZY10-3-1 showing two phases, where phase with larger grains correspond to a Y-rich phase.

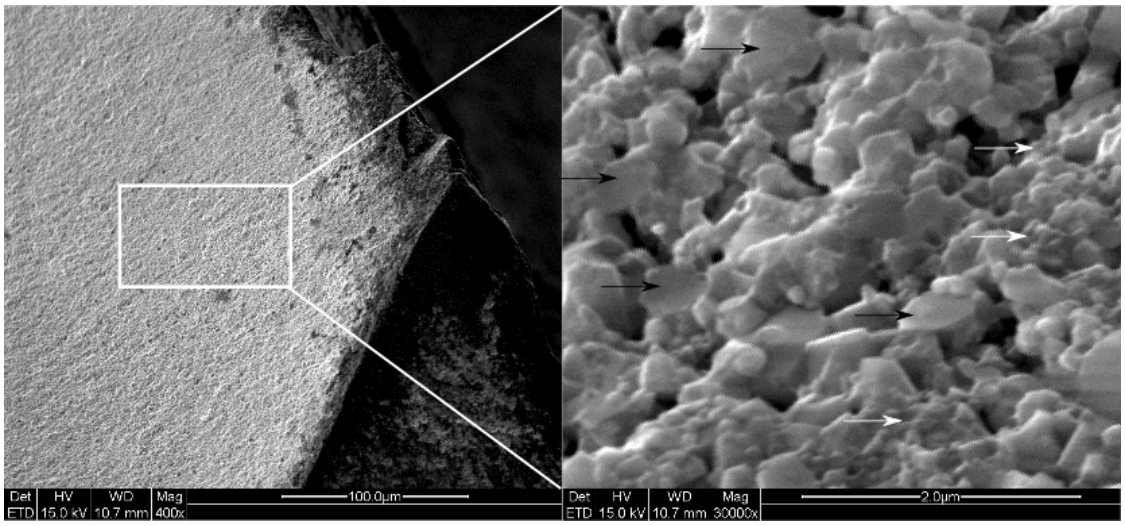

Figure 6.6: SEM micrographs of a fractured surface. The right image gives a magnification of the left image. Here black and white arrows indicate trans- and intergranular fracture surfaces, respectively.

6.2.2 Grain orientation

EBSD was performed on BZY10-HT TEM sample, and the results are shown in figure 6.7. The data was processed using the OLM analysis software to give a GBCD based on the obtained diffraction patterns. Assuming low-angle boundaries have tilt angles <15°, the following result is obtained: ∼11% low-angle, ∼68% high-angle and ∼21% CSL type grain boundaries. The latter may be further classified into the corresponding Σ values, as given in figure 6.8b. Here the sigma values are counted up to 29, and everything above this has been summed as random boundaries, denoted *R*. The fraction of CSL boundaries is similar to what has been reported before for BZY, but an interesting observation here is that the fraction of *R* has decreased whilst the number of CSL i.e. Σ3-29 has increased [44]. Furthermore, the misorientation angle is plotted together with the *Mackenzie distribution*, which describes the distribution of misorientation angles for random untextured materials, in figure 6.8b [82, 83]. For this sample, the distribution maxima is slightly shifted to lower angles, but generally follows the shape of the Mackenzie distribution except for steep increase at the lowest angles.
These results should be interpreted with care, as the cleanup procedures used in OLM may change the outcome. Cleanup here means to fit erroneous data to neighbouring orientations. Furthermore, the software does not distinguish all the individual grains properly, as may be seen in figure 6.7b, thus overestimating the number of grain boundaries.

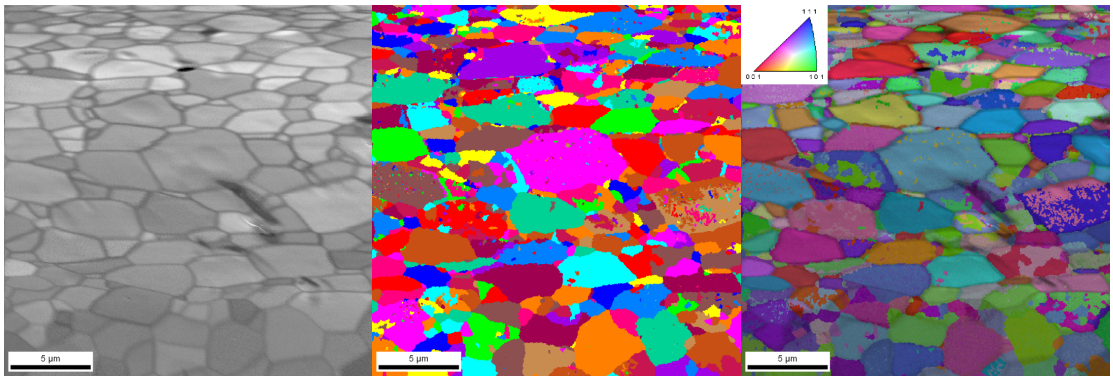

(a) **(b)** **(c)**

Figure 6.7: Results obtained from EBSD. Figures represents the image quality (IQ), individually coloured grains and IQ with orientation as the colour scale in (a), (b) and (c), respectively.

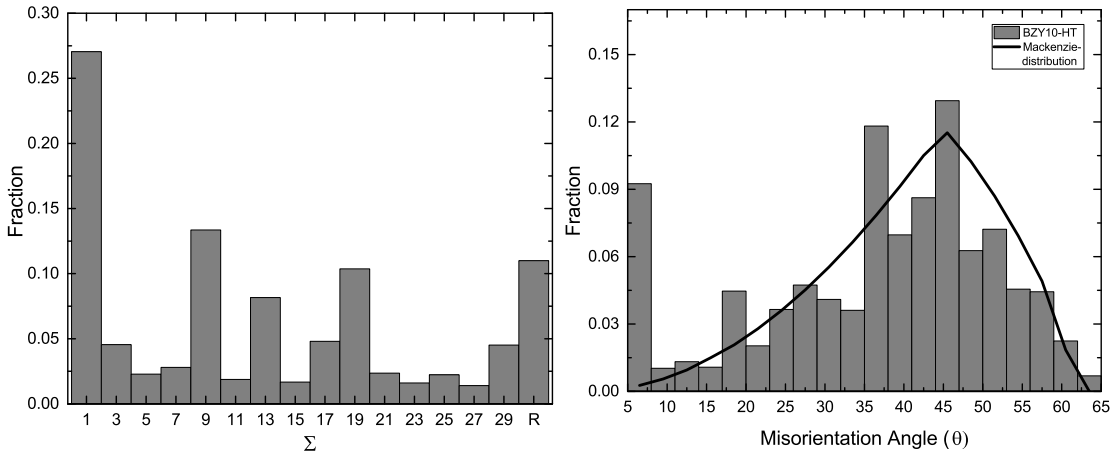

(a) **(b)**

Figure 6.8: EBSD grain boundary distribution histogram of the BZY10-HT sample and the misorientation angle plotted with the Mackenzie distribution in (a) and (b), respectively.

6.3 Analytical TEM investigation of grain boundaries

In the following subchapters, the compositional and structural result related to grain boundaries and triple point for samples BZY10-2, BZY10-HT and the two samples containing Ni, are presented. The term *interfaces* is frequently used when addressing both triple points and grain boundaries at the same time.

6.3.1 BZY10-2

Generally the microstructure consists of a single phase material with no indications of neither amorphous- nor secondary phases at the interfaces. HRTEM only allows resolving grain boundaries in which the misorientation of the two grains has a pure tilt character (no twist component), as may be seen in figures 6.9a and b [84]. It was once found that both grains were simultaneously oriented along a well defined ZA at the same time. This finding enabled direct interpretation the structure at the interface, and is presented under the symmetric tilt boundary subsection. However, the orientation relationship between two grains could be found by obtaining the SADP for each grain and finding the ϕ_{net} needed to tilt each grain into ZA. Table 6.2 gives the characteristics of twelve GBs and according to the scheme given in section 2.1.4: these are of random nature, since they all have a twist component and are not oriented along the same zone axis. Some might be pure twist boundaries if the grain boundary plane is similar in both grains, but this cannot be directly known from the SADPs.

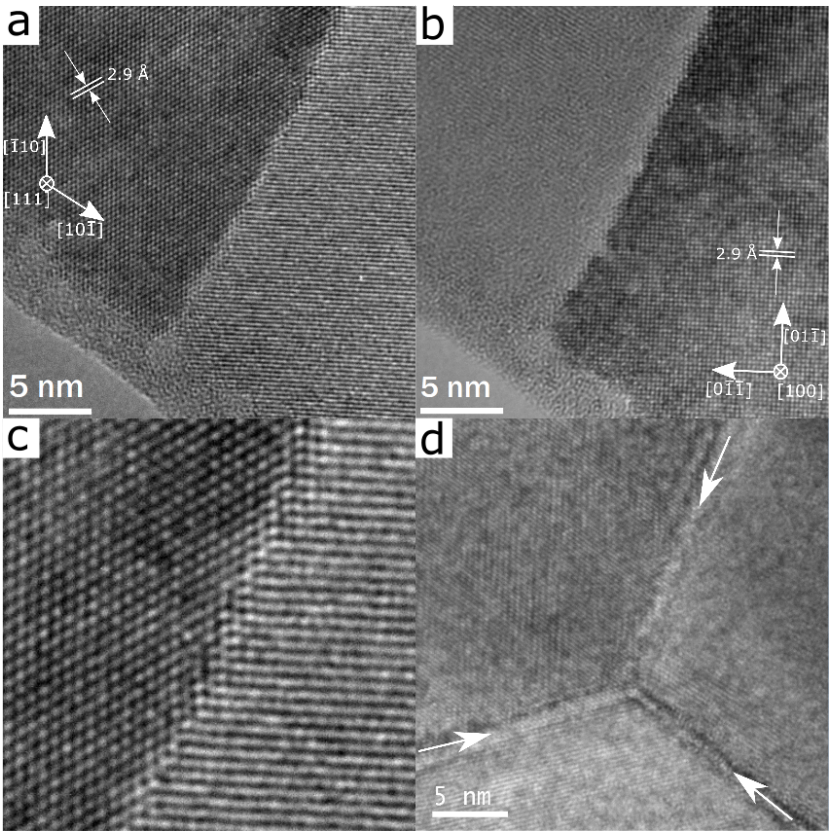

Figure 6.9: Typical interfaces in BZY10-2 obtained by HRTEM. The grains are tilted into the [111] and [100] ZA in (a) and (b), whilst (c) gives a magnification of (a). (d) shows a typical triple point.

Table 6.2: Summary of 12 different grain boundaries in BZY10-2, indicating the zone axis of grains A and B, and the corresponding goniometer tilt angle between the two zone axes.

	1	**2**	**3**	**4**	**5**	**6**	**7**	**8**	**9**	**10**	**11**	**12**
$[uvw]_1$/ $[uvw]_2$	[111]/ [001]	[001]/ [011]	[111]/ [001]	[111]/ [113]	[110]/ [133]	[112]/ [113]	[111]/ [112]	[011]/ [112]	[113]/ [112]	[113]/ [011]	[113]/ [111]	[113]/ [123]
ϕ_{net}	n/a	n/a	4.9	n/a	1.9	10.6	7.4	9.4	7.7	6.1	6.3	7.4

TEM-EDS spot analysis was performed in grains, triple points and grain boundaries. The oxygen content varies from 10-50 at.% and is therefore excluded in the quantification. Cation ratios are expressed as [Y]/([Y]+[Zr]) and [Ba]/([Y]+[Zr]), which ideally are 0.1 and 1.0, as shown in figure 6.10. Two observations which will be discussed later are:

1. The interfaces have enrichment of Y, with mean values of 0.10(3), 0.14(4) and 0.16(5) for grain, GB and TP respectively.

2. The interfaces have a lower amount of Ba with mean values 1.14(7), 0.87(1) and 0.88(6).

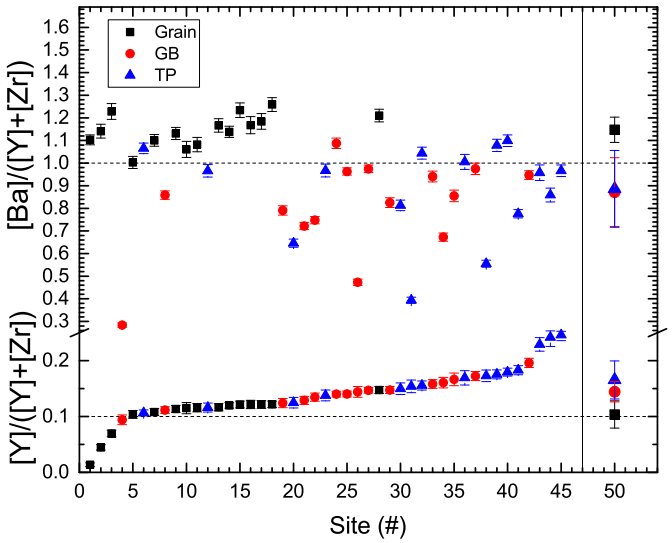

Figure 6.10: TEM-EDS on BZY10-02 from 45 unique sites, plotted in increasing order for Y. The mean and the absolute mean deviation of each region have also been added.

STEM-EDS maps showed no observable differences in the chemical composition, but linescans gave indications of Y segregation, approximately 2 nm from the grain boundary core on both sides. Figure 6.11 shows an area in which four linescans have been

conducted. There is no clear trend as the 4 different linescans show different results and scattered values. A reason for this could be overlapping grains, i.e. GB is not parallel to the electron beam. Line Data 1 shows an increase of Y and depletion of Ba. A similar trend is perhaps present in Line Data 2.

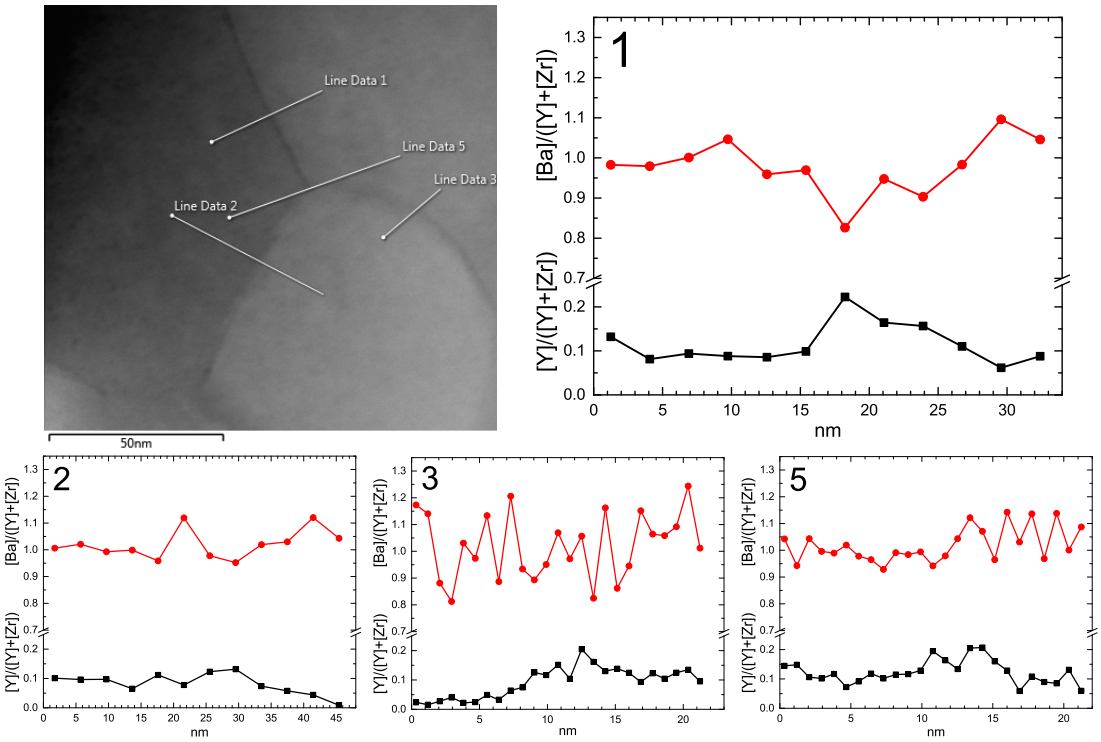

Figure 6.11: EDS linescans over interfaces in sample BZY10-2. The labels 1, 2, 3 and 5 corresponds to the lines drawn in the micrographs. The data is normalised to show the cation ratios.

Changing instrument to FEI Titan enabled resolving the oxygen columns. In figure 6.12, a grain boundary is studied using ADF and ABF (c,d), where the right grain is oriented along a $\langle 110 \rangle$ zone axis, whilst the left grain is not oriented along a defined zone axis. The grain boundary is not perfectly in focus, due to either overlapping grains or not correct defocus value. Image (e) is a HAADF image of the oriented grain and (f) the Fast Fourier Transform (FFT) of (e).

STEM-EDS mapping over the grain boundary area was also performed and showed a significant increase in Y content as opposed to the other elements. Figure 6.13 shows the EDS maps, where the intensity reflects the at.% (not counts). The quantified results from three unique positions are summarised in table 6.3. If the grains were overlapping, one would expect all the elements to increase linearly with the thickness, which is not the case here. If the observed increase in Y is related to segregation, or due to other effects, is difficult to justify.

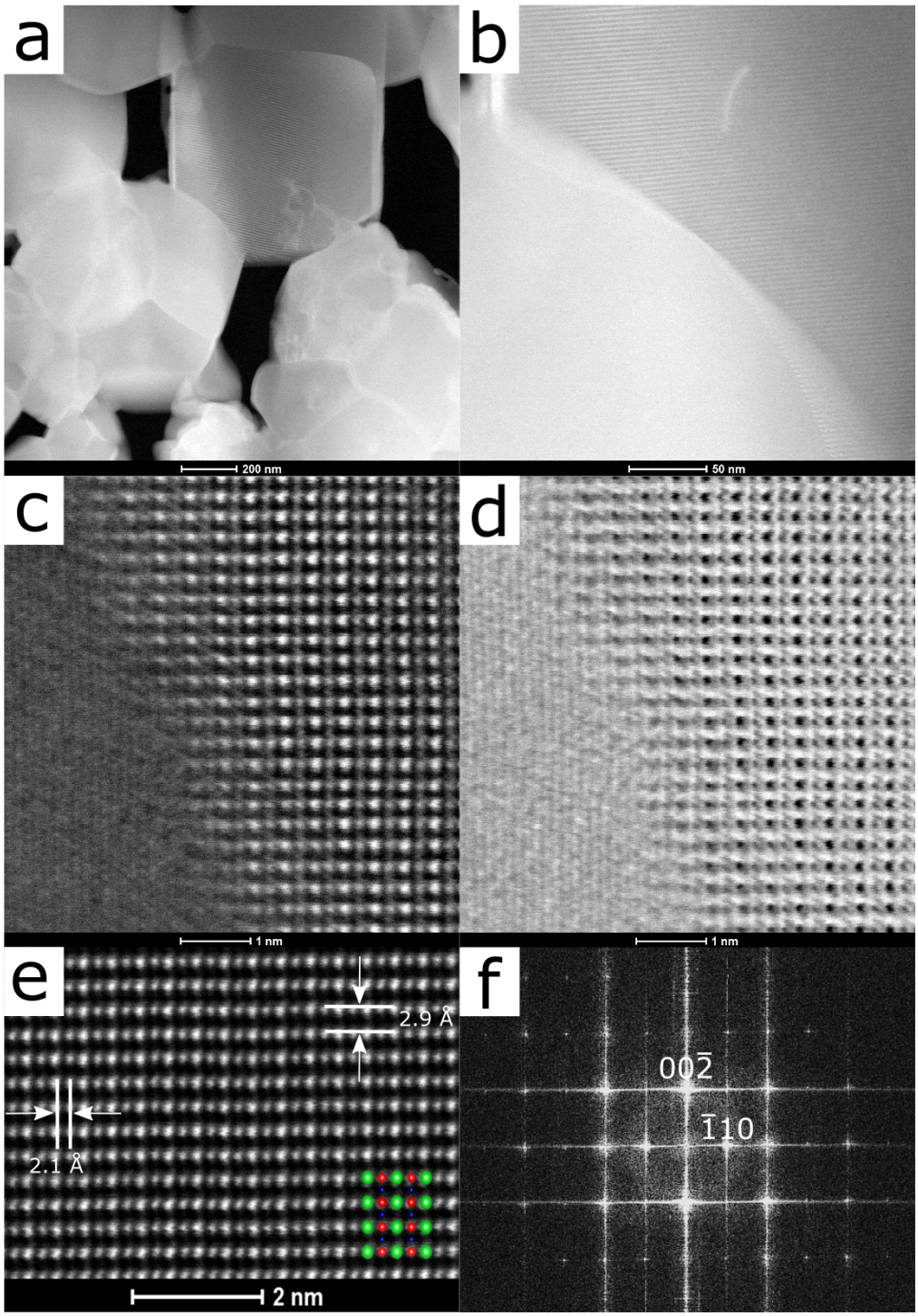

Figure 6.12: (a-b) are micrographs of the area where HR -STEM images has been acquired. (c) and (d) are ADF and ABF micrographs, respectively. In (c) the columns are of Ba, Zr/Y and O, with Ba being the most intense. Figure (e) is a HAADF image of the grain oriented along the [110] ZA and (f) is its corresponding FFT.

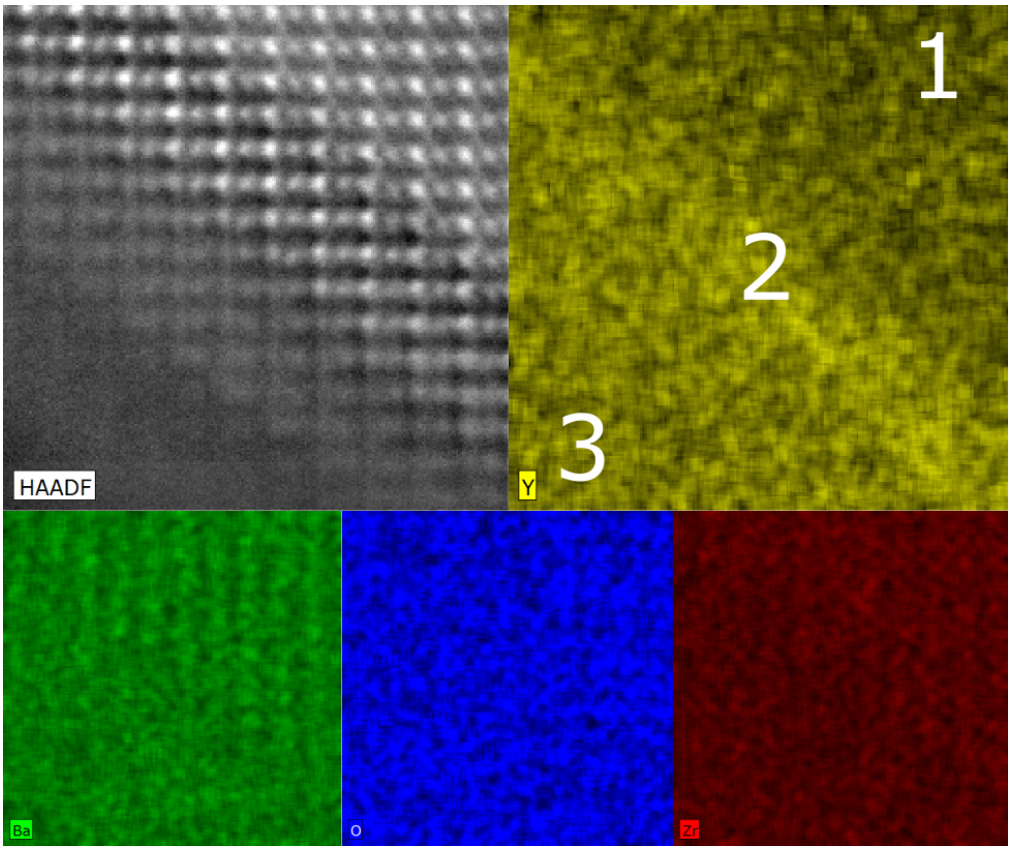

Figure 6.13: The figure shows EDS map over a GB, where the intensity profile represents at.%. The component is stated in the figure and the three numbers in the Y map represent areas in which quantification has been performed.

Table 6.3: Quantified composition from the three positions in figure 6.13. Values reported in at.%, and the cation ratios is also represented.

Site	Ba	Zr	Y	O	[Y]/([Y]+[Zr])	[Ba]/([Y]+[Zr])
1	27.30 (±1.62)	26.01 (±0.87)	2.85 (±0.15)	43.84 (±1.50)	0.10±0.00	0.95±0.06
2	27.10 (±1.63)	22.86 (±0.78)	6.84 (±0.28)	43.19 (±1.51)	0.23±0.01	0.91±0.06
3	24.88 (±1.58)	23.61 (±0.81)	5.86 (±0.26)	45.65 (±1.57)	0.20±0.01	0.84±0.06

In the grain oriented along the [110] zone axis in figure 6.12e, EDS-mapping was performed and revealed near atomic resolution EDS. These resulted in presented in figure 6.14. Although these images should be interpreted with the uttermost degree of care, they do reveal some interesting features. The intensity maxima of the Zr atoms are clearly marked with the periodic intensity maxima in the Zr chemical map. For Y the trend is not as clear; which may be due to low concentration of Y or might be since Y

is not only confined to the Zr site. The Ba atoms intensity maxima fits well in-between the Zr columns. Lastly, O is not as clear since it takes place on the Ba column and in-between Zr columns in the [110] zone axis.

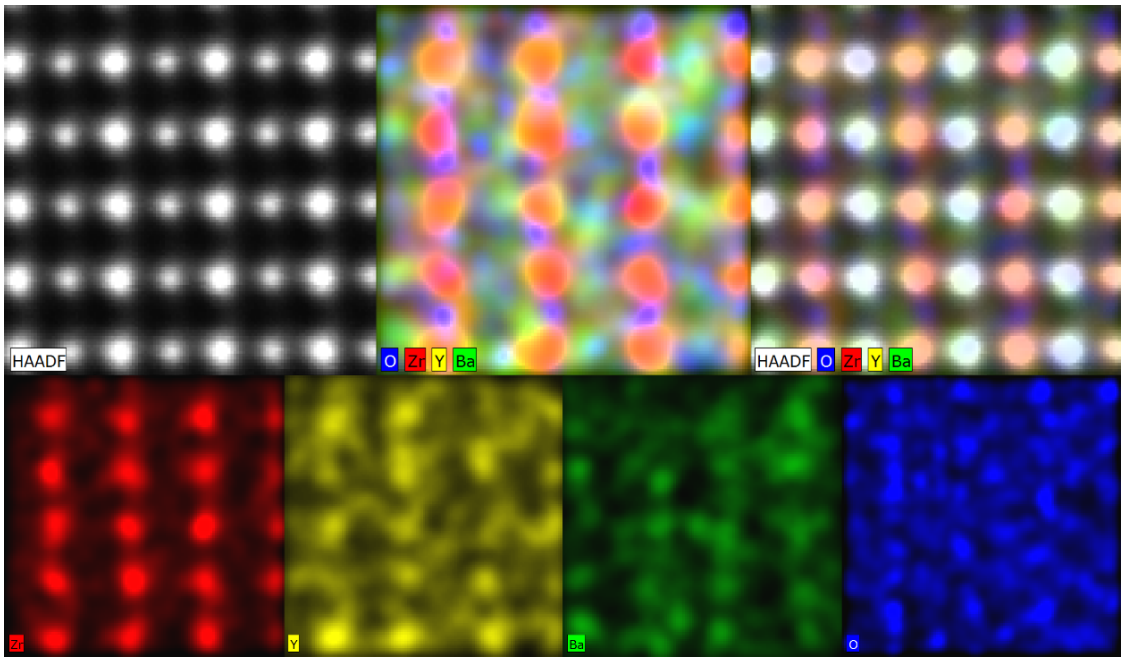

Figure 6.14: STEM-EDS maps of a grain oriented along the [110] zone axis. In the HAADF image the most intense column is of Ba/O, whilst the other belongs to Zr/Y.

Symmetric tilt boundary

A symmetric tilt grain boundary with two grains simultaneously oriented along the [110] ZA, with (111) as the GB plane, was observed as shown in figure 6.15. The tilt angle was measured to $\theta = 70.53°$, which gives the full notation $\Sigma 3[110](111)$ for this GB. EELS indicated no change in chemical composition and only showed an increase in the plasmon intensity from left to right. This may be since the area probed of approximately 4 nm is within the space-charge layer. There are some Electron Energy-Loss Near-Edge Structure (ELNES) features in the oxygen K-edge, but since these have not been thoroughly studied, the EELS spectra are presented in appendix D. Geometric Phase Analysis (GPA) was performed on the ADF micrograph indicating a slight expansion at the core. This is presented together with the computational results on the same grain boundary.

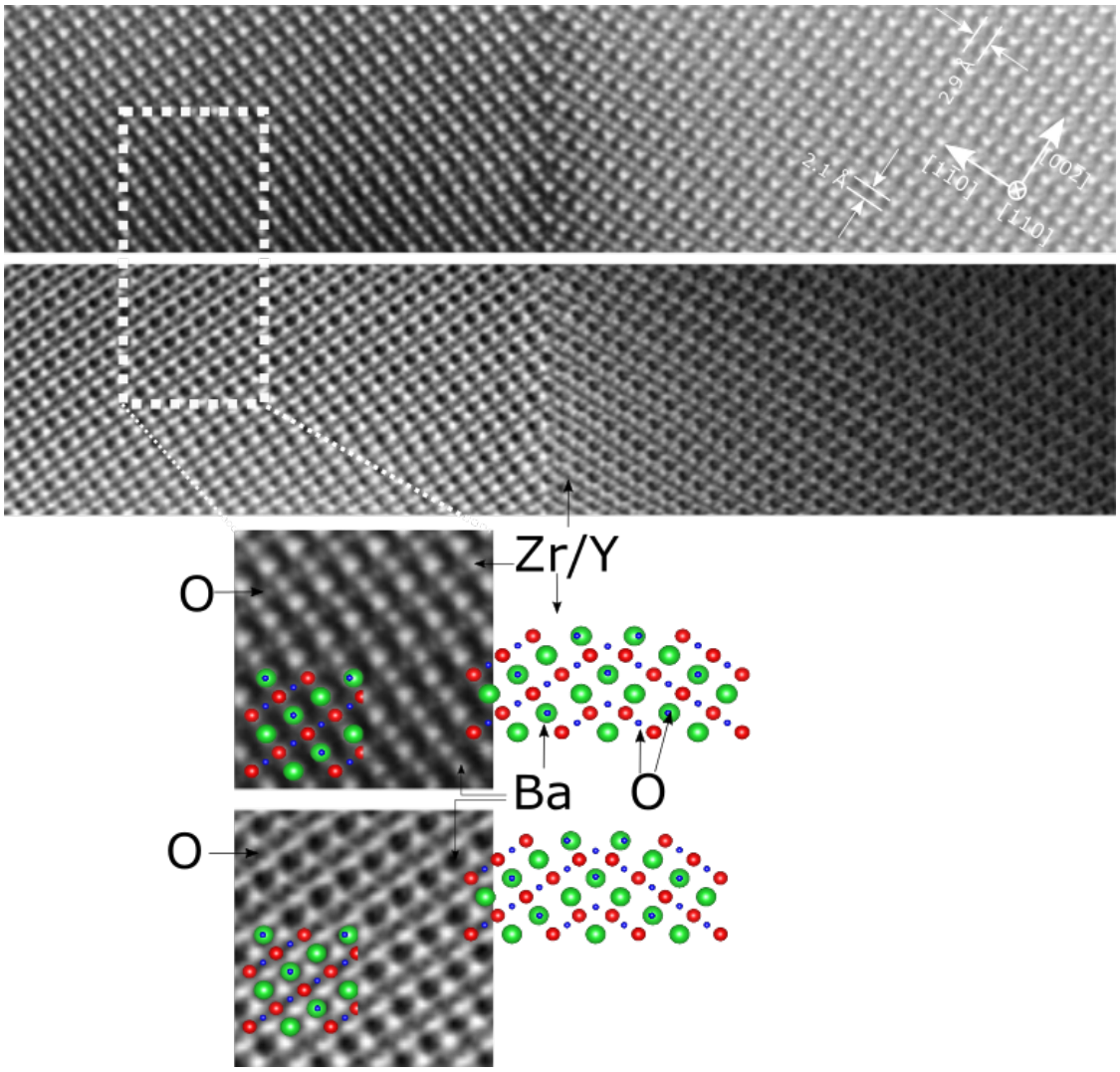

Figure 6.15: ADF (above) and ABF micrograph of the Σ3(111)[110] grain boundary. Columns are of Ba, Zr/Y and O, where Ba appears most intense in the ADF micrograph. Opposite in ABF.

6.3.2 BZY10-HT

Similar to the previous sample, no amorphous-, secondary phases or dislocations are observed in grain boundaries. The grains here appear larger and have a more homogeneous shape, when compared to BZY10-2, as may be seen in 6.16b. The orientation relationship of 12 GBs are summarized in table 6.4. Three GBs are oriented close to the same zone axis, so here the net tilt angle also represents the twist angle φ. Cation ratios from TEM-EDS are reported in figure 6.16a. Similarly to BZY10-2, a slight Y increase at the interfaces is observed, but the same degree of Ba depletion is not present.

Table 6.4: Summary of 12 different grain boundaries in BZY10-HT, indicating the zone axis of grains A and B, and the corresponding goniometer tilt angle between the two zone axes.

	1	**2**	**3**	**4**	**5**	**6**	**7**	**8**	**9**	**10**	**11**	**12**
$[uvw]_1$/ $[uvw]_2$	[311]/ [321]	[311]/ [311]	[211]/ [311]	[111]/ [210]	[210]/ [311]	[210]/ [210]	[100]/ [111]	[102]/ [115]	[102]/ [113]	[111]/ [111]	[102]/ [111]	[113]/ [111]
ϕ_{net}	4.7	4.2	2.6	5.5	5.9	4.4	0.4	0.1	3.8	2.2	4.5	7.8

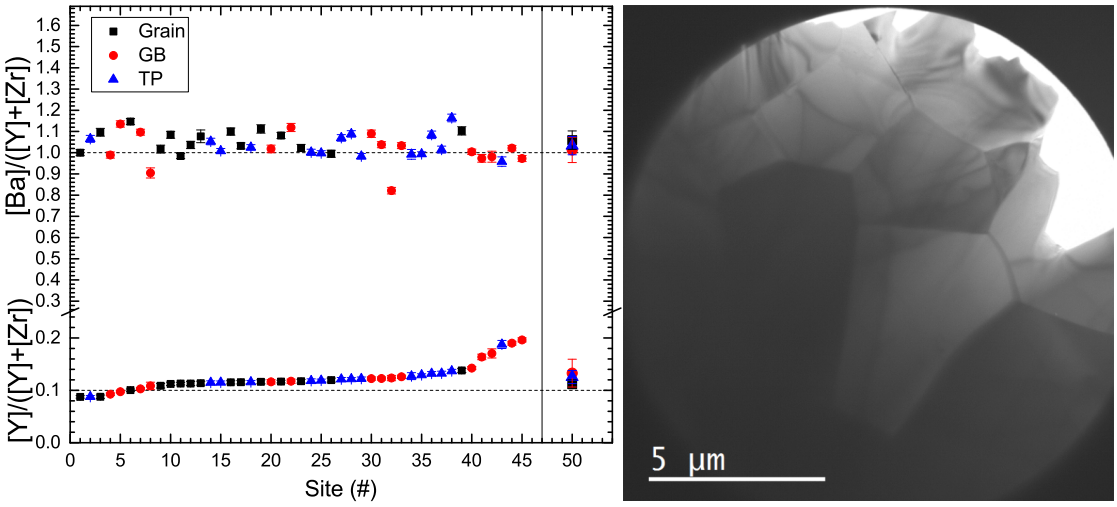

(a) **(b)**

Figure 6.16: TEM-EDS on BZY10-HT from different regions, normalized by the cation concentration and sorted in an increasing order for [Y] in (a). The mean and the absolute mean deviations is also indicated. An overview micrograph is given in (b).

6.3.3 BZY15+NiO

$Ba_{0.98}Zr_{0.85}Y_{0.15}O_{3-\delta}$ (BZY15-BaDef)

A general overview micrograph of this sample is shown in figure 6.17a. The grains appear larger and more homogenous in shape than what was presented for BZY10-2. No secondary phases from SAD or EDS experiments are observed. From TEM-EDS no indication of segregation for Y is observed, but the Ni at.% increases at the interfaces, as seen from figure 6.17c. Furthermore the cation ratios are reported in figure 6.17d. Surprisingly, the [Y]/([Y]+[Zr]) ratio is higher in the grain interior than the interfaces. Hpowever, the mean value is lower than the doping concentration of 15 mol%. The Ba concentration is higher at the GBs and triple points, than in the grain interior. If Ni defects replaces Y'_{Zr} as the charge compensating defects to the presumably positively charged GB core, is a topic for further discussion.

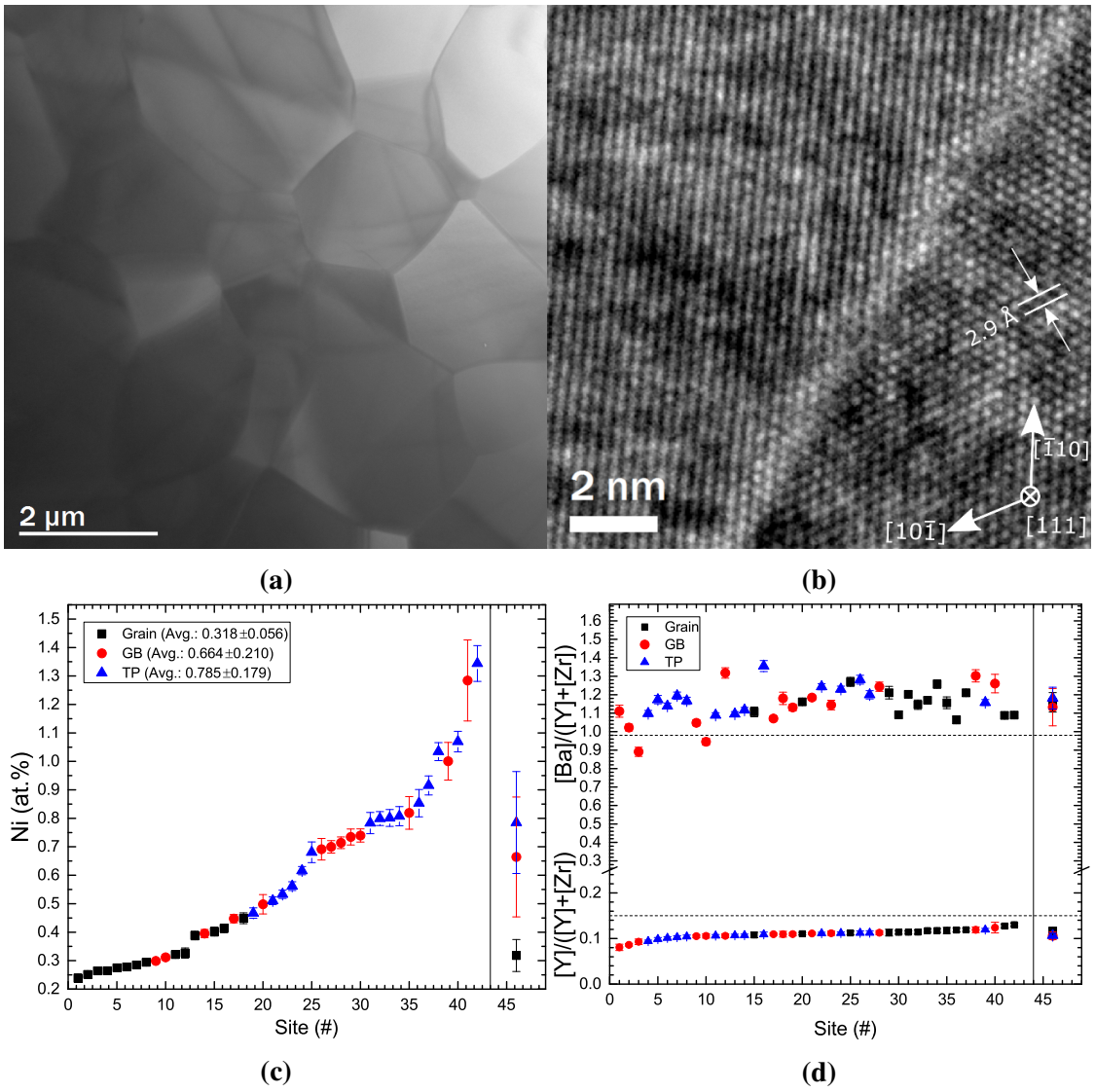

Figure 6.17: Overview micrograph showing the grain morphology and a GB where the right grain is oriented into ZA in (a) and (b), respectively. (c) gives the Ni at.% for different sites and (c) the Ba and Y cation ratios, as obtained by TEM-EDS. The mean and the absolute mean deviation of each region have also been added.

$Ba_{1.02}Zr_{0.85}Y_{0.15}O_{3-\delta}$ (BZY15-BaDef)

Similar values of Ni at.% is obtained from TEM-EDS in grain interior, but at the interfaces values ranges from approximately 1.5 at.% to 5-8 at.% and 13-14 at.%. For the two latter, the Y content is also considerably larger than the doping amount and the ratio between cations (Ba:Zr:Y:Ni) is ~54:32:8:6 and ~53:21:12:14. Whether this corresponds to one or two phases is difficult to clarify, since the GB and TP areas are small and the

signal may stem from a larger area. For the same reason diffraction could not be used to determine the phase(s).
Figure 6.18 shows 3 HAADF micrographs where (a) shows a general overview. (b) and (c) are areas in which secondary phases are observed and STEM-EDS mapping has been performed. Quantification from the indicated areas are given in table 6.5, and these results show the present of Ni rich phase(s). This is in agreement with the micrographs as phases with a lower atomic weight should appear darker.

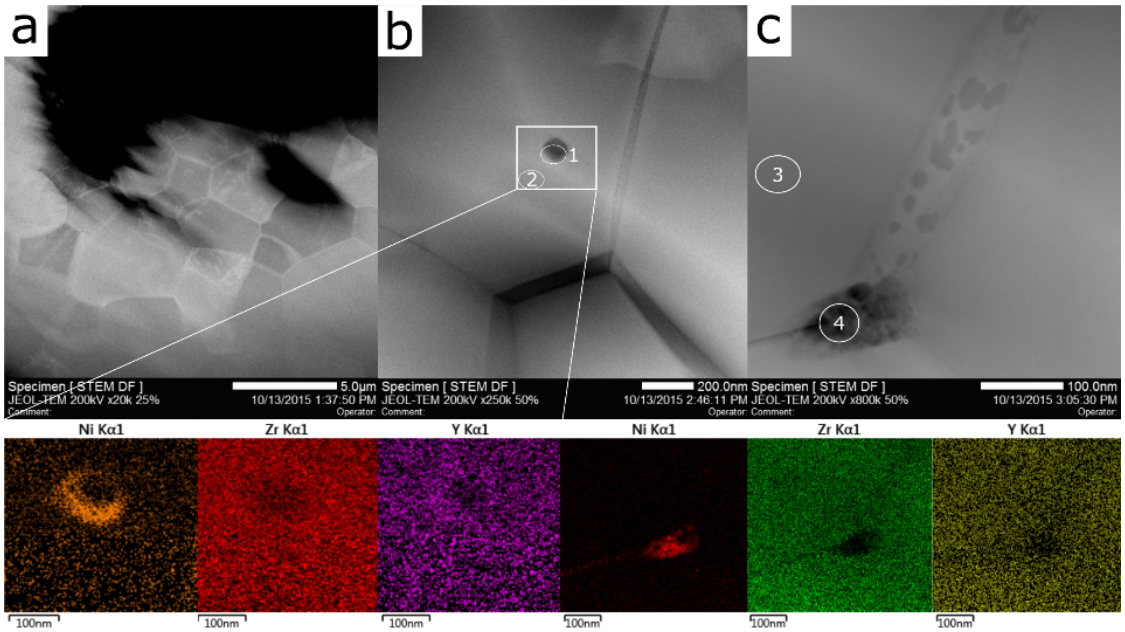

Figure 6.18: HAADF micrographs showing an overview, a particle on a grain and a triple point in (a), (b) and (c) respectively. EDS maps of Ni, Zr and Y from figures (b) and (c) is shown below.

Table 6.5: Quantified data from areas indicated in figure 6.18. Values for the chemical elements are in at.%.

Site	Ba	Zr	Y	O	Ni	[Ba]/([Y]+[Zr])	[Y]/([Y]+[Zr])
1	26.1	16.1	3.2	51.7	3.0	1.35	0.17
2	28.3	19.9	3.6	47.7	0.5	1.20	0.15
3	28.2	20.6	3.6	47.2	0.4	1.18	0.15
4	26.8	5.1	2.0	36.6	29.5	3.78	0.28

6.4 Compositional study by XPS

In Figure 6.19 the survey scan and HR scans of oxygen, yttrium and the valence band are shown. The quantification result of the HR peaks are given in table 6.6 along with the sampling depth. It was shown in section 6.2.1 that a Y-rich phase was present in the surface of the As-Rec sample (BZY10-3-1). This is the reason the Y content is higher in this sample in the XPS results, as to the two other samples. In the polished sample the ratio: [Y]/([Y]+[Zr]), is closer to the expected values. For the fractured sample a higher ratio is observed, which is expected as the fractured surface is a mixture of inter- and transgranular fracture, whilst the polished sample is thought to be dominated of transgranular, i.e. represent bulk. The reason for the low Ba content in all samples is not fully understood. The unidentified peak at 685 eV in the survey scan at is most likely due to F (686 eV).

Table 6.6: Quantification of XPS data in at.%. The IMFP and sampling depth is also indicated for each peak and valence band(VB).

	Ba (3*d*)	**Zr (3*p*)**	**Y (3*d*)**	**O (1*s*)**	**VB**	**[Y]/([Y]+[Zr])**	**[Ba]/([Y]+[Zr])**
As-Rec	7.78	16.07	17.23	58.92		0.51	0.23
Polished	9.07	17.28	3.02	70.65		0.06	0.45
Fractured	16.30	13.91	5.85	63.93		0.29	0.82
IMFP (nm)	1.85	1.01	0.66	1.40	0.00(2)		
Depth (nm)	5.55	3.03	1.98	4.20	0.00(6)		

Yttrium

In the As-Rec sample no chemical shift of the Y 3*d* peak is observed, but occur in the polished and fractured samples. In the two latter, the peak seperation between the two chemical states is ∼2.6 eV. The intensity ratio between $3d_{3/2}$ and $3d_{5/2}$ of 4/5 is used to enable deconvolution of the second chemical state, as shown in figure 6.19b. Quantification results are given in table 6.7. The larger Y 3*d* pair is most likely due Y in the $BaZrO_3$ phase, whilst the other might be an indication Y substituting the A-site, as this would change the effective oxidation state. It is not believed that Y metal (156 eV) is present here, as this would be indicated in the valence band HR spectra by giving signals all the way up to 0 eV, i.e: there would be no bandgap. For the As-Rec sample the Y-state is attributed to the secondary phase observed in the surface of the pellet by SEM and XRD.

Table 6.7: Quantification of the different Y-states. Numbers reported as ratios and values in parentheses are in at.%. State "2" corresponds to the two peaks at lowest binding energy in figure 6.19b for the polished and fractured samples.

	1		**2**	
	Y $3d_{3/2}$	Y $3d_{5/2}$	Y $3d_{3/2}$	Y $3d_{5/2}$
As-Rec	50.01 (8.61)	49.99 (8.61)		
Polished	36.39	50.35	5.79	7.47
	86.74 (2.61)		13.26 (0.40)	
Fractured	28.93	47.87	10.02	13.19
	76.71 (4.48)		23.21 (1.35)	

Oxygen

A variation in the peak intensity and position for the O 1s peak is observed in figure 6.19c. In all samples there are two peaks related to oxide- and the hydroxide oxygen, but in the polished sample another contribution is present; most likely belonging to H_2O, which was used as lube during polishing. It would be tempting to say something about the dehydration properties as to bulk (polished) and grain boundary (fractured), but this is difficult since the fracture is of both trans- and intergranular type. Since they are in turn the same pellet and the fractured scan was performed last, it may be seen that there is no presence of water in the latter, and that the ratio between O^{-1} and O^{-2} changes from 62:38 to 56:44 for the fractured sample.

Valence band

Peak fitting of the valence band maximum resulted in two distinct sets of peaks for As-Rec and the fractured sample, as shown in figure 6.19d. The intersection with the x-axis was linearly estimated in order to obtained the energy of the highest occupied state. These energies and corresponding fit functions, errors and R^2 values are given in table 6.8. For the Fractured sample a change in the VBM of $\sim$0.2 eV is observed for the two fitted peaks.

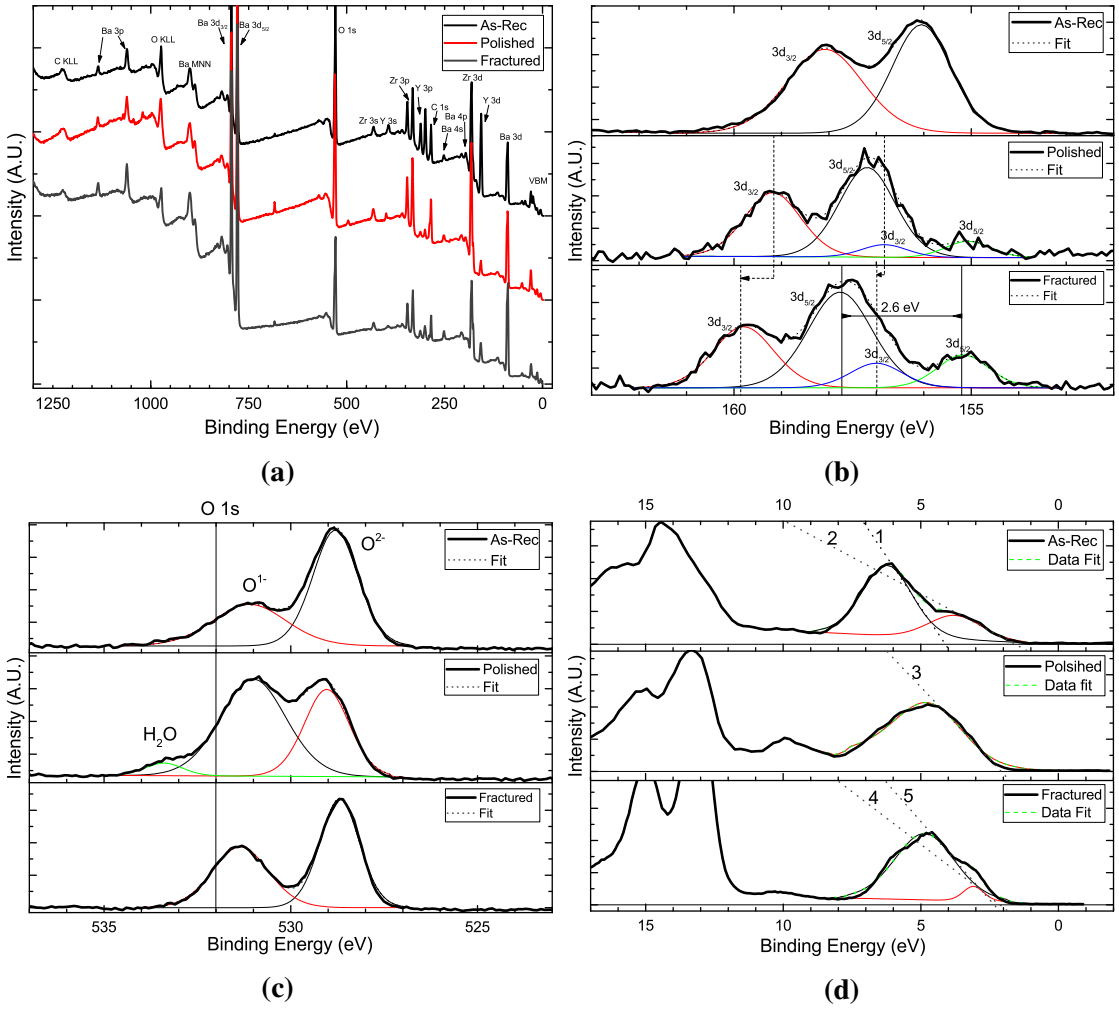

Figure 6.19: (a) shows the survey scans for all samples. (b), (c) and (d) show HR-scans for Y, O and the VBM, respectively. In (b), (c) and (d) the peak fitting and the resulting envelope function is shown. In (d) the intersect with the x-axis, as obtained by linear interpolation, is shown through the lines 1-5, with corresponding values reported in table 6.8.

Table 6.8: Fitting of valence electron peaks indicated in figure 6.19d.

Line	Function	R^2	Intersect (eV)
1	f(x) = (-616.3±40.7)+(150.0±7.3)x	0.99(5)	4.1±0.3
2	f(x) = (-84.1±4.2)+(53.7±1.4)x	0.99(8)	1.5±0.0
3	f(x) = (-298.5±8.5)+(143.5±2.3)x	0.99(9)	2.0±0.0
4	f(x) = (-181.1±7.7)+(85.1±2.8)x	0.99(7)	2.1±0.1
5	f(x) = (-295.5±18.1)+(126.4±4.3)x	0.99(5)	2.3±0.1

6.5 Conductivity

The conductivity was studied by impedance spectroscopy on the BZY10-01 sample. The measurements conducted using the first measurement setup, as described in section 4.5, proved to be difficult to deconvolute since the bulk semicircle was not observable. Even after estimating the bulk resistance by finding the intersect with the grain boundary semicircle, the resulting conductivity vs. temperature plot indicated features of which it was difficult to address the physical meaning to. These results are thus presented in appendix E for the interested reader.
The second set of measurements proved to be more reliable and is what will be further discussed. This data set was fitted using the equivalent circuit given in figure 6.20. An inductor has been added since inductance was present at higher temperatures, as may be seen in the high frequency region in figure 6.21. A value of 10^{-6} to 10^{-9} H was used attributed to the inductor, which only influenced the fitting at higher temperatures. Furthermore, the electrode (RQ) part has been removed, since the electrode contribution is not the main focus. A parasitic parallel capacitance (C_{stray}) of 5 pF, originating from the experimental setup, has been subtracted [28]. The equivalent circuit generally fits well to the experimental data and a chi squared value of 10^{-3} to 10^{-4} is obtained.

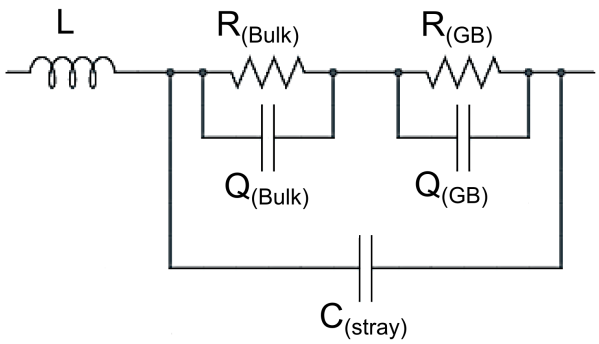

Figure 6.20: Equivalent circuit used to deconvolute the impedance spectra. R, L and Q corresponds to the passive circuit elements resistor, inductor and constant phase element, respectively.

The conductivities are obtained through equations (4.3) and (4.4), using the deconvoluted resistances. Specific conductivity versus temperature for all atmospheres is shown in figure 6.22a. Figure 6.22b is added to illustrate how the GB conductivity changes when it has been corrected for the capacitances under wet air. The capacitances, and their variation with temperature in wet air, are shown in figure 6.22c. Lastly, the Arrhenius interpolation under the same atmosphere is shown in figure 6.22d.
Both bulk conductivity and GB conductivity are independent of the atmosphere, as may be seen in figure 6.22a. However, at $\sim$300 °C the HArMix slope changes more than

under oxidizing conditions for the GB. This could perhaps mean that the conditions are so reducing that n-type (electronic) conductivity starts to contribute, in accordance with the lowest p_{O_2} area of the Brouwer diagram in figure 2.4a.
The bulk activation energy for all atmospheres is found to be 0.38 eV. For the specific grain boundary conductivity the activation energy varies from 0.64 eV under Ar to 0.89 eV for HArMix.
Under the assumption of the brick-layer model, equation (2.64) showed that the ratio between bulk- and GB capacitances should reflect the ratio between grain size and grain boundary width. From figure 6.4 the average size is around 600 nm and by assuming an effective grain boundary width of 4 nm a ratio of 0.006 is obtained. The ratios between capacitances range from 0.002-0.004, which is a close match indicating a good correlation between the sample's microstructure and the Brick-Layer model used here.

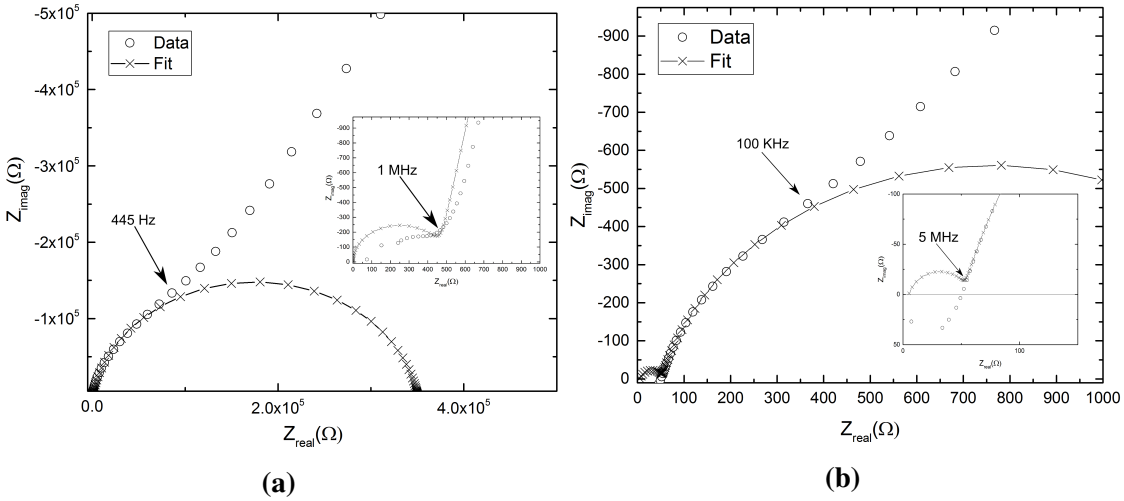

Figure 6.21: Deconvolution of impedance datasets at 200 °C (a) and 400 °C (b) in wet air. The inset figure represents the bulk semicircle.

6.5.1 Space-charge calculations

From the impedance measurement the following properties could be estimated: the bulk relative permittivity (ε_r), the Debye Length (L_D), the Schottky potential $\Delta\Phi(0)$ and the space-charge layer width ($\lambda^\star$) can be estimated from equations (2.62), (2.37), (2.42) and (2.38), respectively. It was demonstrated in section 2.4 that this could be obtained under the assumptions that the dopant concentration is constant throughout the space-charge zone (Mott-Schottky aprroximation), and that protons are the dominating positively charged compensating defect in bulk,

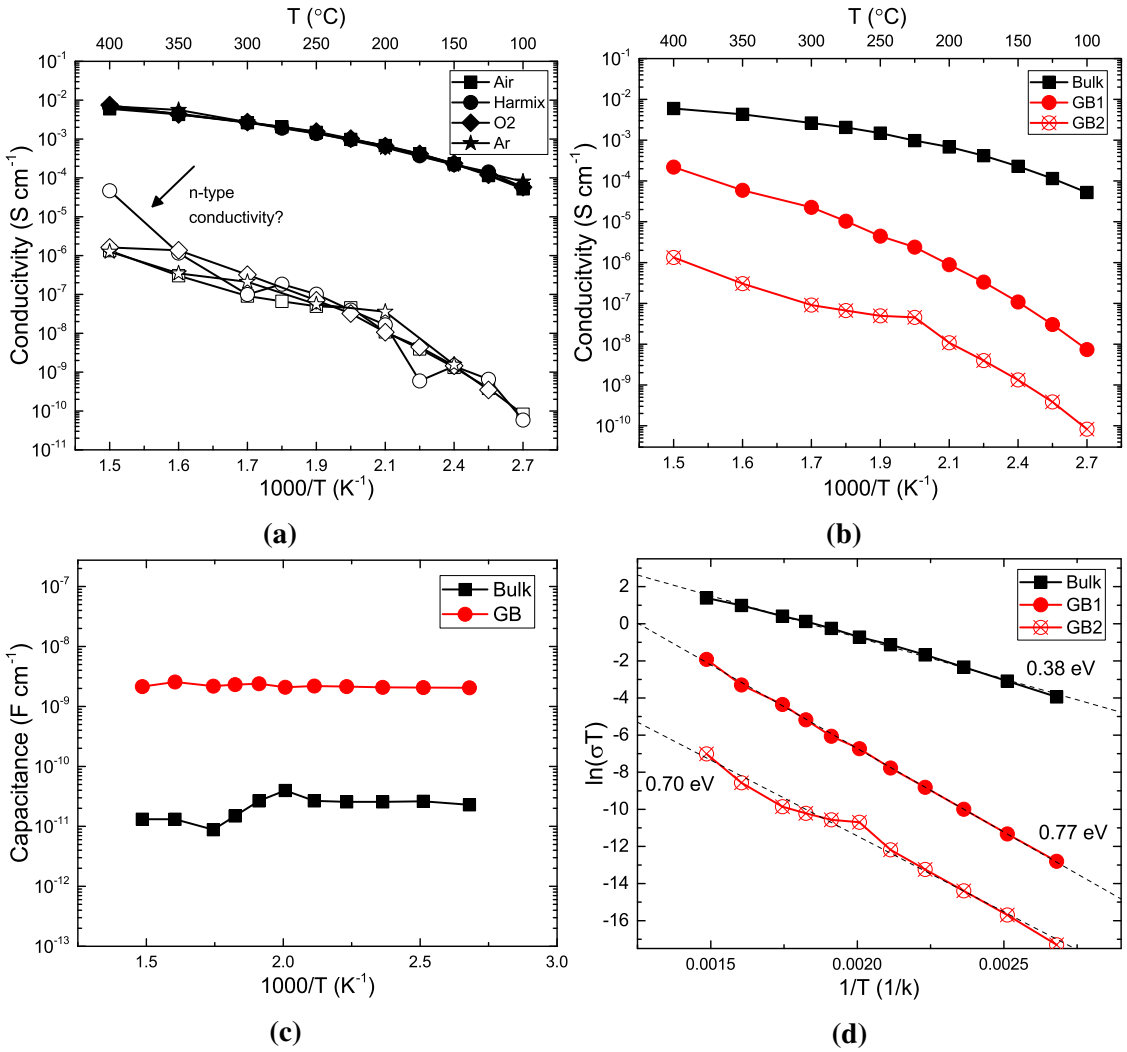

Figure 6.22: (a) Bulk and specific GB conductivity for all atmospheres. (b) Bulk, unspecific- and specific GB conductivity under wet air. (c) Capacitance values vs. temperature and (d) Arrhenius interpolation of figure (b).

For the Debye length a bulk hydrogen concentration, $C_{\mathrm{H}} = 8.29{\cdot}10^{-26}$ m^{-3} is used, similar to what Ricote *et al.* used for BZY10 in [48]. The results are summarised in table 6.9 and the Schottky barrier height under all atmospheres is plotted together vs. temperature in figure 6.23. The barrier decreases with increasing temperature.

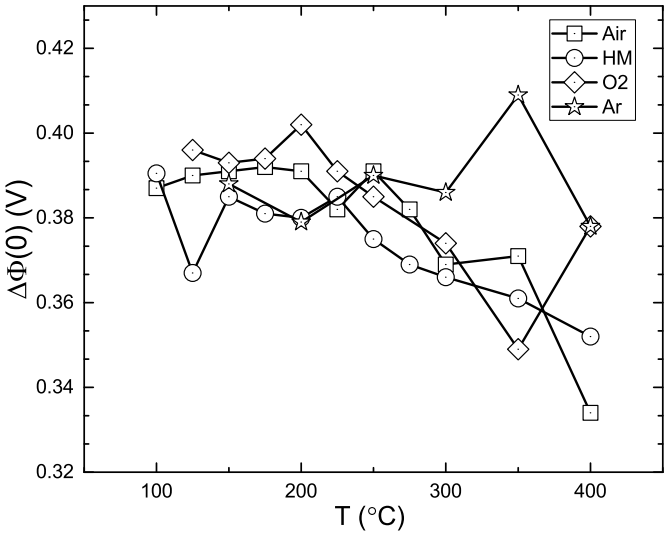

Figure 6.23: Schottky barrier height $\Delta\Phi(0)$ plotted vs. temperature. All the indicated atmospheres are also wet.

Table 6.9: Bulk and GB capacitances, bulk relative permittivity (ε_r), Debye Length (L_{D}), Schottky barrier height ($\Delta\Phi(0)$) and space-charge layer width ($\lambda^{\star}$) obtained at 200 °C in wet atmospheres.

	Air	**HArMix**	**O2**	**Ar**
C_{bulk} (F/cm)	2.66E-11	3.11E-11	3.20E-11	6.96E-11
C_{gb} (F/cm)	2.18E-9	2.12E-9	2.05E-9	1.99E-9
ε_r	76.66	74.53	72.19	69.95
L_{D} (nm)	0.80	0.79	0.78	0.77
$\Delta\Phi(0)$ (V)	0.39	0.38	0.40	0.37
$\lambda^{\star}$ (nm)	4.99	4.85	4.91	4.70

6.6 Computational results

6.6.1 Defects in $BaZrO_3$

Relaxation of the supercell resulted in a lattice parameter of 4.235 Å, which is slightly larger than experimental values, but in agreement with other computational studies [62–64, 81, 85]. The defects Y'_{Zr}, $\nu_O^{\bullet\bullet}$ and $OH_O^{\bullet}$ were studied, and for the latter three unique positions in the structure were tested. Only the configuration pointing towards the Ba atom was found to be stable with a O-H bond length of 0.980 Å, similar to what Sundell

Table 6.10: List of defects in $BaZrO_3$ with corresponding formation energy and chemical expansion coefficient. *Static* and *relaxed* correspond to if the volume of the supercell is held constant or allowed to change.

Defect	ΔE_i^f (eV)		ϵ_i
	Static	Relaxed	
Y'_{Zr}	-0.29	0.10	0.249
$\nu_O^{\bullet\bullet}$	1.45	1.43	-0.219
$OH_O^{\bullet}$	-0.05	0.32	-0.074

et al. reported [64]. An asymmetrically placed hydrogen also converged towards this site, as shown in figure 6.24

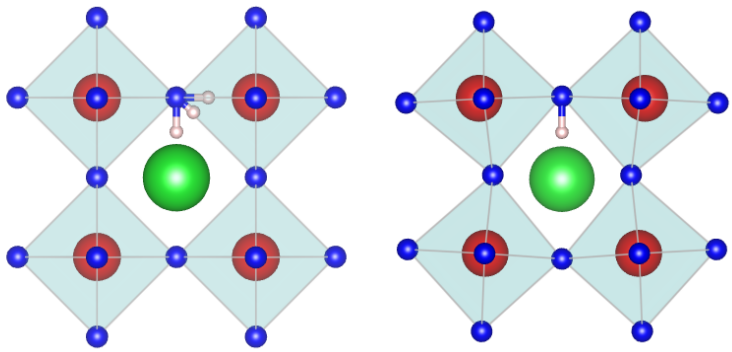

Figure 6.24: (a) shows three positions for hydrogen and (b) shows the most stable configuration. Green, blue, red and white correspond to Ba, O, Zr and H respectively.

The formation energy of all involved defects is reported in table 6.10. The obtained formation energy for $\nu_O^{\bullet\bullet}$ is slightly larger than the 1.21 eV Sundell *et al.* reported. The $OH_O^{\bullet}$ is about 1.2 eV higher [62].
Bjørheim *et al.* [81], reported chemical expansion coefficients of -0.0587 and -0.2390 for $OH_O^{\bullet}$ and $\nu_O^{\bullet\bullet}$, which is in close agreement to the findings here.
Using the values obtained the corresponding expansion and enthalpy upon hydration is 0.071 and -1.55 eV respectively, where the latter is significantly more exothermic than what other computational- and experimental studies proposes. This is related to the formation energy of $OH_O^{\bullet}$. The YO_6 octahedron has 12% more volume than ZrO_6, but the coordination number remains as 6.
Furthermore, the total DOS and the partial DOS of Y, H and the O bonded to H, were obtained and presented in figures 6.25a and 6.25b. From figure 6.25a one may see that the VBM mainly consists of O 2*p* orbitals with some contribution from Zr and Ba. The

proton introduces bound *s*-states at around -7 eV, which overlaps with the *p*-orbital of the binding oxygen atom, thus confirming that the proton is indeed bound to the oxygen as a hydroxide group. Yttrium has a bound state at -16 eV with a slightly lower binding energy than Zr of 0.45 eV, as one may see in figure 6.25b. Similarly, Y introduces electron states in the top of the VBM with a shift of ∼0.35 eV with respect to Zr.

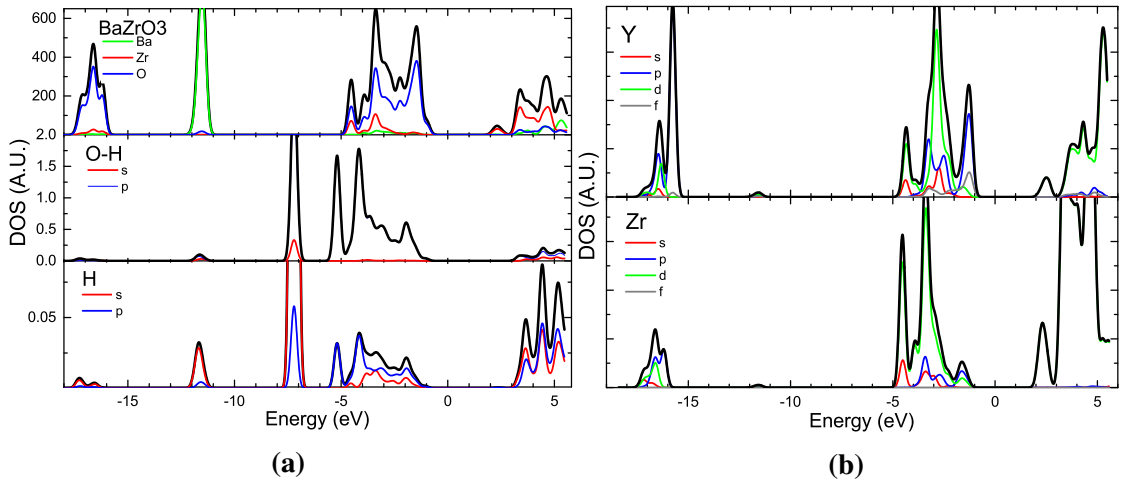

(a) **(b)**

Figure 6.25: (a) total DOS of $BaZrO_3$ and partial DOS of the O forming the O-H bond and for H. In (b) the partial DOS for a single Y and Zr atom is shown.

6.6.2 The grain boundary

Structural considerations

The grain boundary studied here is the same symmetric tilt boundary that was observed by TEM.

The *interplanar distance* is found after the structural relaxation by following the c-axis in figure 6.26c, and starting either from Ba or O in the core. The first spacing is thus Ba(core)-Zr(layer1), thereafter Zr(Layer1)-Ba(Layer2) and so on. Similar following the O-Zr row. This is directly comparable to the obtained results from TEM, and the results from both along with the variation is given in figure 6.26a. The theoretical model has an expansion in the core followed by a clear contraction in the 2^{nd} plane, which stabilizes around the 6^{th} atomic plane. In the TEM results there is an expansion around the core, but the contraction and stabilization is not as sharp. The GPA analysis, shown in figure 6.27, have similar expansion/contraction behvaiour as in the modelled structure. However, it extends much further into the structure than what theory predicts.

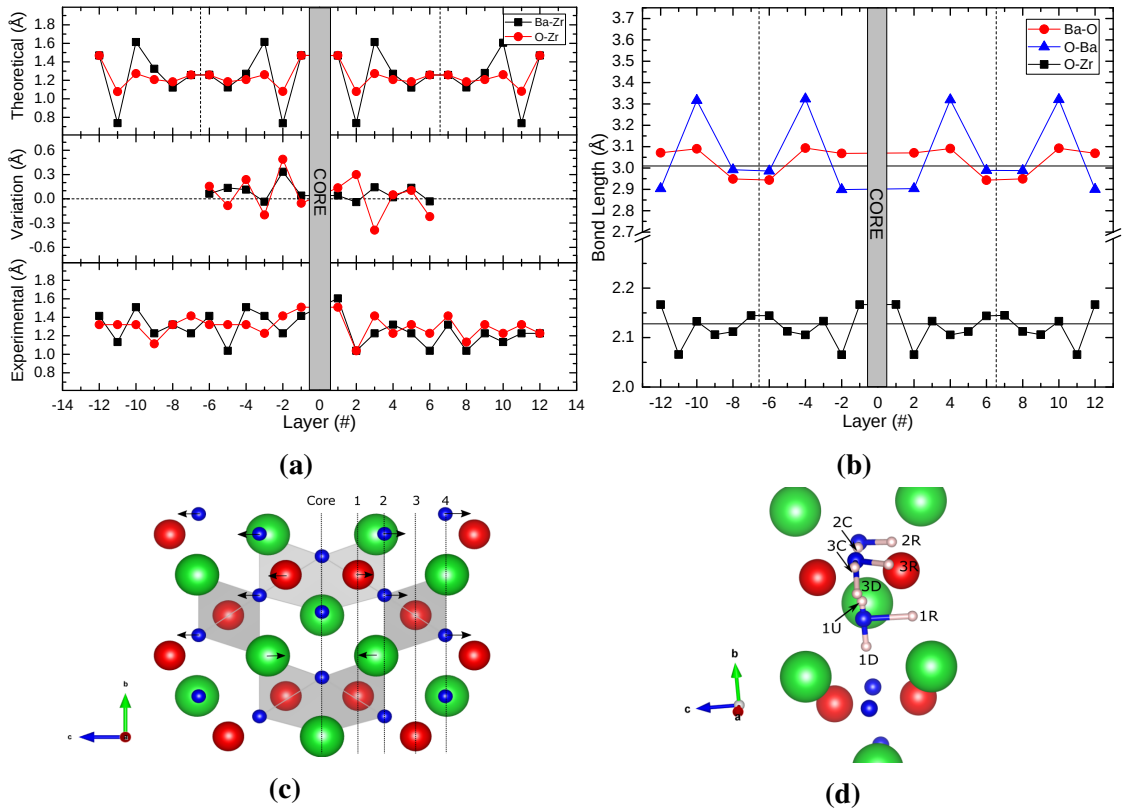

Figure 6.26: (a) is the theoretical interplanar spacing following two lines from the core and the experimental obtained values. (b) represents the bond lengths starting from either Ba or O in the core, and (c) is a schematic view of (b). (d) indicates different sites in the core where the proton stability was tested.

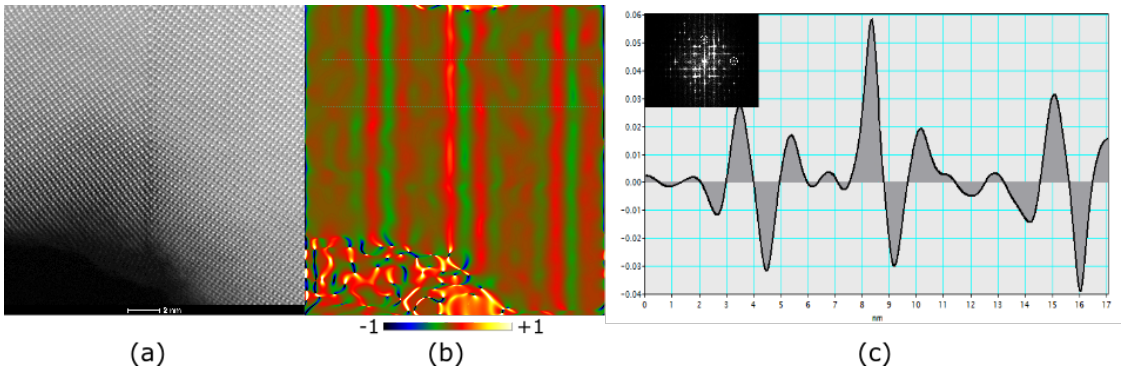

Figure 6.27: GPA analysis of the Σ3 grain boundary in (a). (b) is the resulting figure and (c) shows how it varies in the marked area in (b).

The bond lengths are also obtained and shown in figure 6.26b. One may see that there are some changes in the bond length around the core and in the closest layers, which

is illustrated in figure 6.26c. The oxide ions are most affected by the core and displays the biggest displacement from ideal position. These variations change the effective coordination number of the ZrO_6 octahedron, which is lowered to 5.87 for the octahedron closest to the core, whilst the next octahedron again has CN = 6. Introducing Y'_{Zr} further lowers the CN to 5.78 and also expands the volume by 17.8%; slightly larger than what was obtained in the bulk supercell. Oxygen vacancies have little effect on the structure, except in the core where it expands the Ba-Ba bond over the core from 4.3798 to 5.1346 Å. From a TEM perspective this means that a grain boundary with a significant concentration of oxygen vacancies might appear thicker than one with stoichiometric amounts of O. These defects may either reside on the BaO column or on the O column when the structured is viewed down the a-axis, as in figure 6.26c. Hydrogen may bind to these oxygens, but in the grain boundary core several unique sites were tested as shown in figure 6.26d. Of these, positions 1U, 1D, 2C and 3C were found to be stable.

Formation energies

The formation energy of all involved defects are reported in table 6.11. Oxygen vacancies situated on the O column are found to be about ∼0.1 eV more stable than vacancies on the BaO column. Proton also binds stronger to oxygen located on the O column.
The segregation energies are plotted in figures 6.28(a-c). Here the formation energy of the defect furthest away from the grain boundary core is used as the reference. The trend is that Y does not stabilize close to the core. Both $\nu_O^{\bullet\bullet}$ and $OH_O^{\bullet}$ one the other hand stabilizes in the grain boundary core. The findings are similar to what Polfus *et al.* and Helgee *et al.* reported, even though the absolute values are slightly different [65, 69].

Table 6.11: Formation energies, ΔE_i^{f} (eV), for all involved defects in their corresponding plane from the grain boundary core at "0". The values in parenthesis are from volume relaxed calculations.

Defect	**0**	**1**	**2**	**3**	**4**	**5**	**6**
Y'_{Zr}		0.30 (0.38)		-0.10 (-0.03)		0.07 (0.14)	
$\nu_O^{\bullet\bullet}$ (O)	0.29 (0.50)		1.23 (1.34)		1.46 (1.35)		1.42 (1.30)
$OH_O^{\bullet}$	-2.19		-1.35		-1.39		-1.45

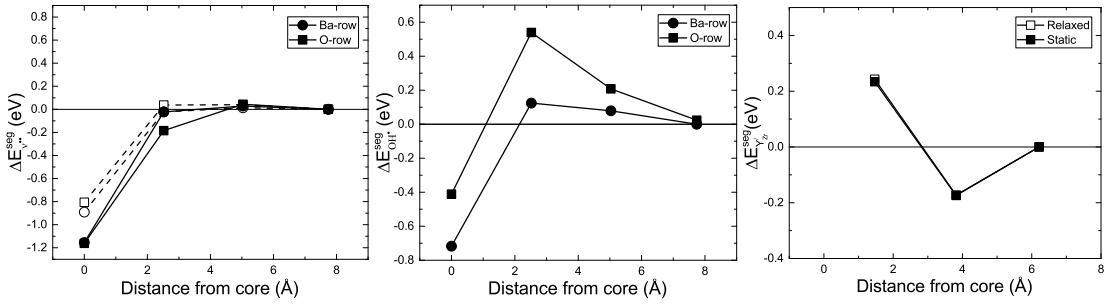

(a) **(b)** **(c)**

Figure 6.28: Segregation energies of $\nu_{O}^{\bullet\bullet}$, $OH_{O}^{\bullet}$ and Y'_{Zr} in (a), (b) and (c), respectively. Solid lines represents results from static calculations, whilst the dotted line in (a) is obtained when allowing the supercell to relax.

Density of states

The partial DOS of Y and Zr at different sites was calculated as shown in figure 6.29. Both atoms display a relative shift of ∼0.18 eV between layers 1 and 5, where layer 1 introduces states in the top of the VBM. The relative difference between Y and Zr is ∼0.28 eV, where Y introduces states in the top of the VBM. This fits to the obtained results from XPS.

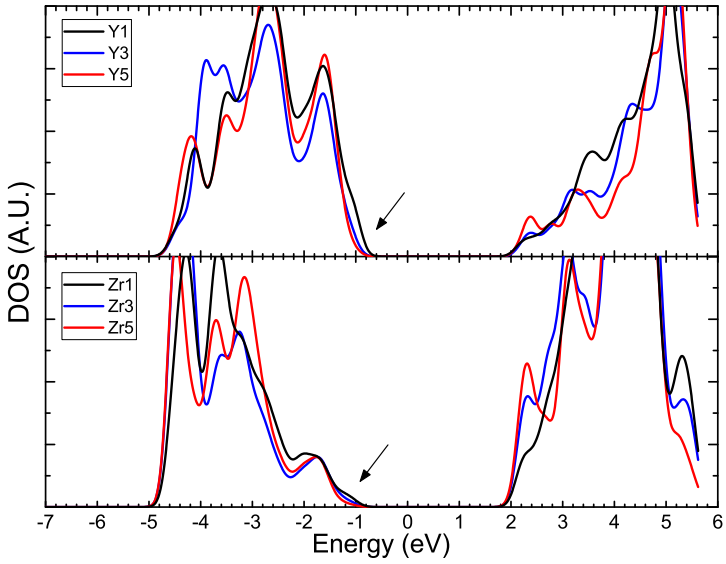

Figure 6.29: Partial DOS for Y and Zr in layers 1, 2 and 5, in the grain boundary model. The difference between layer 1 and 5 is ∼0.2 eV.

Chapter 7

Discussion

7.1 Samples prepared by SSR

The sintering behaviour of the BZY10 samples prepared fits well into literature where the grains are generally smaller than 1 μm and bulk density is $\sim$90% when prepared through the SSR route. The sample's grain boundary conductivity is 3 orders of magnitude lower than bulk in wet O_2 at 400 °C ($7.5{\cdot}10^{-3}$ vs. $1.6{\cdot}10^{-6}$ Scm^{-1}). From the obtained capacitance values the effective space-charge layer width $\lambda^{\star}$ was calculated to be $\sim$5 nm, indicating that the average space-charge region should be around 10 nm excluding the core.

Phenomena such as Ba evaporation and presence of secondary phases in the surface were also observed. From TEM-EDS it was demonstrated that the Y segregation to grain boundaries in many cases also was coupled with Ba depletion. It could then be that the Ba evaporation is accelerated close to interfaces and not only at the surface. Furthermore, both phenomena may be linked as the evaporation of Ba might lead to Y substituting on the A site as: $Y^{\bullet}_{Ba}$. Significant segregation of Y may then further result in the formation of Y-rich phases such as Y_2O_3 and/or YSZ as was observed in the surface of BZY10-3-2. These observations show the importance of controlled environment and that the addition of sacrificial powder in the synthesis alone, may not be sufficient.

In the XRD results peak broadening/splitting was present, indicating the presence of more than one phase. It was not possible to deduce the site occupancy through the Rietveldt refinement, but some interpretation may be carried out. The peak splitting was observed in every peak; an indication that a tetragonal phase is not present here, as it would not split the peaks where h=k=l. Thus the phenomena here are most likely due to two cubic phases with space group $Pm\bar{3}m$, but with slightly different lattice parameters, which is also what the refinement indicated. Then one may wonder what is causing the

change in lattice parameters. Depletion of Ba and increase of Y were observed by TEM-EDS, and from XPS two chemical states of Y were shown to exist. Thus, the splitting may then correspond to a phase in which Y partly substitutes the A site, as proposed independently by Han *et al.* and Azad *et al.* in previous studies. [21, 86]. Their results are summarised in table 7.1.

Table 7.1: Summary of phases from literature where A-site substitution is reported.

	Nominal Composition	Phase Label	Composition	Temperature Treatment	Lattice Parameter	Comment
Azad [21]	$BaZr_{0.9}Y_{0.1}O_{3-\delta}$	α	$Ba_{1.01}Zr_{0.9}Y_{0.1}O_{3-\delta}$	1500 °C (both α and β present)	4.1963	Lower proton conductivity
		β	$(Ba_{0.985}Y_{0.015})(Zr_{0.915}Y_{0.085})O_{3-\delta}$	1700 °C (only α present)	4.2053	Higher proton conductivity
Han [86]	$BaZr_{0.9}Y_{0.1}O_{3-\delta}$	H-1	$(Ba_{0.970}Y_{0.000})(Zr_{0.810}Y_{0.190})O_{3-\delta}$	1600 °C	4.2298 4.2230	Hydrated Unhydrated
	$Ba_{0.9}Zr_{0.8}Y_{0.2}O_{3-\delta}$	H-2 H-3	$(Ba_{0.900}Y_{0.000})(Zr_{0.880}Y_{0.120})O_{3-\delta}$ $(Ba_{0.851}Y_{0.149})(Zr_{0.632}Y_{0.368})O_{3-\delta}$	1600 °C	4.2109 4.2016	Major phase Minor phase

BZY10-1 has similar lattice parameters as for the two phases proposed by Azad *et al.*, whilst the other samples fit better in combination with the β phase and H-1/H-2 by Han *et al.*. The minor phase by Han *et al.* (H-3) has not been observed for the samples in this study. Knowing that there are two phases present in the sample the question remains as how they are located; as unique grains or as two phases within the same grain. The refinement indicated one peak to be broader than the other which may either be: 1) the presence of more than two phases with a range of lattice parameters or 2) two phases wherein one has smaller crystallites. A schematic representation is illustrated in figure 7.1.

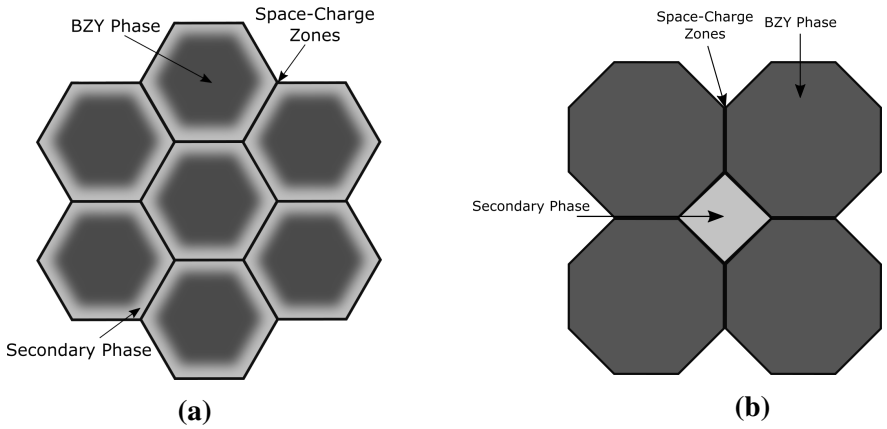

Figure 7.1: Two possible locations of the two phases. In (a) both phases are within the same grain, whilst in (b) they are present in separate grains. The shapes are schematic only and may not represent the real case.

Assuming that two phases are oriented similarly within the same grain, their corresponding diffraction spots cannot be distinguished. Using the lattice parameters obtained for BZY10-2, the relative shift in the d-values is calculated and shown in table 7.2. For the same reason two phases in two different grains are not distinguishable, as the uncertainty in the diffraction patters is in the 2nd decimal place. HRTEM micrographs did not indicate any two phase grains, but again this may not be within the resolution limit if the arrangement atoms do not give any changes in the contrast. However, such an effect might be observed in the translational Moiré patterns assuming that the phases are oriented similarly. Some calculations using the lattice parameters for BZY10-2, obtained by XRD, are summarised in table 7.2 and show that the spacing in the Moiré patterns is quite large. This was not observed, which may indicate more than two phases with a range of lattice parameters.

Table 7.2: Calculated d-values, Moiré spacing and $\Delta 2\theta$ values using the two lattice parameters for sample BZY10-2 obtained through XRD.

hkl	$\mathbf{d}_{hkl}$ **Phase 1 (Å)**	$\mathbf{d}_{hkl}$ **Phase 2 (Å)**	$\Delta\mathbf{d}_{hkl}$ **(Å)**	**Moiré spacing (nm)**	$\Delta 2\theta$ (°)
100	4.20	4.21	0.01(0)	119.79	0.07
110	2.97	2.98	0.01(0)	84.70	0.10
111	2.42	2.43	0.00(8)	69.16	0.13
200	2.10	2.10	0.00(7)	59.89	0.15
211	1.87	1.88	0.00(6)	53.57	0.18
220	1.71	1.72	0.00(6)	48.90	0.20
221	1.48	1.49	0.00(5)	42.35	0.24
310	1.40	1.40	0.00(4)	39.93	0.26

Furthermore, the EDS results showed that the grain interior generally has close to the nominal composition. Again, the result captured by the detector gives the average of an area and when the changes in composition are as little as here; it may not be observed. The EDS maps did not reveal any discrepancies either. If the grains are overlapping, the effect of both segregation and the separation of very similar phases, is not possible. To summarise: a phase such as $(Ba_{1-z}Y_x)(Zr_{0.9}Y_{0.1-x})O_{3-\delta}$ was indicated by XRD and XPS. It remains unclear to what extent Y partly substitute the A site and how the phase is distributed within the sample. *ALCHEMI* and Electron Probe Micro-Analysis (EPMA) are two possible routes for further investigating this [87].

7.2 Comparison between low- and high temperature treatment

7.2.1 Composition

The presented TEM-EDS result for BZY10-2 indicated that Y segregates to the interfaces, together with a depletion of Ba, which may correspond to an increase in the defect ν''_{Ba}. A similar observation was reported by Shirpour *et al.* from an EELS study on Sc-doped $BaZrO_3$ [61]. The values presented in this thesis appear scattered, which may be since the segregation behaviour is correlated with the misorientation angles of the interface, as suggested from DFT calculations [65]. Indications of ν''_{Ba} at the grain boundary interfaces and triple points may introduce the defect: $Y^{\bullet}_{Ba}$, although it is unclear if this would only appear in the grain boundary core or in the space-charge layers. It was recently demonstrated by Aruta *et al.* that the peak splitting for Y and Zr in the XPS spectra could be attributed to these cations partly substituting the A site [88]. The relative energy shift between the two peaks was consistent with the relative values obtained when comparing the energy shift of core binding states from the partial DOS obtained by DFT. The peak splitting was also observed in the results presented in this thesis; thus further indicating the presence of $Y^{\bullet}_{Ba}$.
Y segregation to the interfaces was similarly observed in BZY10-HT, but the same degree of Ba depletion was not present here. This is a strange observation, since this is what one would naturally expect to occur at the temperature treatment the sample had been subjected to. Their synthesis was performed under oxidation conditions (5% O_2 in Ar), at a pressure of 2 bar. This may perhaps low enough p_{O_2} to drive the equilibrium in equation (2.18) to the left, and thus prevent the formation of metal vacancies.
Polfus *et al.* has estimated from first-principle calculations that ν''_{Ba} is a strong proton trap with corresponding binding energy of -0.78 eV for the defect association $(OH^{\bullet}_{O}\nu''_{Ba})'$ [89]. This, along with the experimental results by Han *et al.*, show that Ba deficiency has a detrimental impact on the proton conductivity in Y doped $BaZrO_3$ [90]. This is in agreement with the conductivity properties measured and reported in this thesis on BZY10-1.

7.2.2 Microstructure

From the SEM micrographs and the grain size histogram there it is clear that the grains in BZY10-HT have grown abnormally large in comparison with the BZY10 samples prepared by SSR. The question which remains is why does this only occur at extremely high temperatures (2200 °C), but not after prolonged sintering at 1700 °C as Iguchi

et al. observed [44]. A possible explanation could be that the abnormal temperature treatment has introduced not only a growth process, but a *recrystallization* process, in which energetically unfavourable interfaces diminishes in favour of more energetic ones. The EBSD results presented here one BZY10-HT gave some indication that high-angle boundaries were replaced by low-angle boundaries when comparing with the Mackenzie distribution and with the results reported by Iguchi *et al.* [44]. However, since EBSD was not performed before the heat treatment it can offer no more than some qualitative indications. The TEM results did show that the frequency of near CSL structures were more frequent in BZY10-HT than in BZY10-2, and that the net tilt angle ϕ_{net} generally was lower between the ZA of the two grains. This may, however, just be a coincident as only twelve grain boundaries were studied.
It should be emphasized that the CSL obtained from EBSD is geometrical only and disregards the plane of the grain boundary and the microscopic degrees of freedom. Consequently, the macroscopic properties may not necessarily correlate with the Σn value [91].

Recrystallization

The term *recrystallization* is defined as "... formation of new grain structure in a deformed material by the formation of and migration of high angle boundaries driven by the stored energy of deformation" [91]. The mobility of a boundary is defined as:

$$m = \frac{\nu}{P}, \tag{7.1}$$

where ν is the velocity of the advancing grain boundary and *p* its driving force. Doherty *et al.* attributes the primary driving force behind recrystallization to stored deformation energy, which is most likely not the case in $BaZrO_3$ as bend contours and dislocations have not been observed in TEM. More relevant is the second contributing driving force; the grain-boundary energy, which is defined as the grain boundary energy divided on the radius of the shrinking grain $p = \sigma/a$. The migration properties follow an Arrhenius behaviour, where the corresponding activation enthalpy ΔH^{mig} and prefactor A_0 is dependant on variables such as the misorientation angle, the grain boundaries chemistry, deformation, pressure and naturally temperature.
In BZY10-HT, the activation enthalpy for grain boundary migration might have been reached during the high temperature treatment. Correspondingly, energetically unfavourable interfaces might have diminished whilst the area of more favourable ones have increased. These will most likely have different behaviour with respect to segregation and electrostatic potentials, than the randomly oriented grain boundaries.

7.2.3 Orientation of grain boundary's influence on core potentials

An explanation to the non-segregation behaviour in BZY10-HT could perhaps be attributed to the presence of more energetically favourable low angle GBs, as these generally have lower segregation concentration than unfavourable high angle grain boundaries in metals [13]. In the model ceramic perovskite $SrTiO_3$ such effects have been investigated [26, 92, 93]. Most notable is the study by Roger A. De Souza where 7 bicrystals with tilt angles around the [001] axis is summarised, and compared with the $\Sigma 3(111)[110]$ tilt boundary [26]. His results indicate that the driving force for formation of $\nu_O^{\bullet\bullet}$ is lowest for the grain boundary with the highest symmetry, i.e. the symmetric tilt boundary. However, the highest driving force were **not** observed in the grain boundary with lowest symmetries; but in the grain boundaries consisting of ordered arrays of strongly perturbed structural configurations.
The discussion by De Souza may be directly transferable to BZY since the structure is cubic in both systems and the interfaces are thus not altered to the same degree as might had occurred if the structure exhibited an orthorhombic or tetragonal symmetry. Under the assumption that the increasing concentration of $\nu_O^{\bullet\bullet}$ is the main driving force for space-charge formation, the remaining issue os to addresses how the driving force for formation of $\nu_O^{\bullet\bullet}$, as well how the segregation of charge compensating defects, changes with different defined orientation and crystallographic mismatches.

7.2.4 Validity of the Mott-Schottky approximation

In the space-charge model it is assumed that the concentration of the acceptor dopant is constant throughout the space-charge region. Generally, this assumption is only valid under low operational temperatures, since the cations are immobile in these temperature ranges.
Both the BZY10 samples studied by TEM, and the ones studied with XPS, demonstrate that segregation of Y towards the interface actually does occur, which is not in accordance with the Mott-Schottky approximation. This could be an effect of the equilibration of the core potential occurring during sintering, if the Schottky barrier height is non-zero at elevated temperatures. Polfus *et al.*, however, demonstrated that at 1500 °C equilibrating Y'_{Zr} only lowers the space-charge potential by 0.02 eV for the $\Sigma 3(111)[110]$ symmetric tilt boundary, which then would have little difference if the Gouy-Chapman approximation was applied instead [69]. This is somewhat in agreement with the fact that no segregation behaviour was observed for the same grain boundary through EELS in this thesis. The results presented by Polfus may in turn only represent the case of the low energy grain boundaries and not capture the real scenario as random, i.e. high

energy grain boundary, are more prominent in a true ceramic sample. This was demonstrated through EBSD and TEM. One does not know how the random grain boundaries act, but segregation may be higher in these at elevated temperatures.

Another aspect of the concentration profile of the dopant is on how it equilibrates with respect to formation of ν''_{Ba}. Through TEM-EDS for BZY10-2 it was shown that Ba-loss was more frequent in areas where Y segregated. The overall space-model should perhaps also include ν''_{Ba} if they are present in high enough concentration to affect the segregation driving force.

When proposing the Brouwer diagrams in section 2.3.1, a simplification was made in equation (2.18) that the B site cation vacancy forms as easy as the A site in presence of oxygen gas, which is probably not the case. Nonetheless, if the equations are correct; then the formation of ν''_{Ba} should be suppressed when sintering under low p_{O_2}. This may be the reason Ba depletion was not observed in the BZY10-HT sample, as it was sintered under a oxygen partial pressure of 0.1 bar. Thus the formation of ν''_{Ba} may be neglected and then only have to consider the dopant and the depleted charge carrier through the Gouy-Chapman approximation. The two defects in consideration are then accumulation of Y'_{Zr} and depletion of $OH^{\bullet}_{O}$, and the space-charge model one should consider then looks as what is shown in figure 7.2.

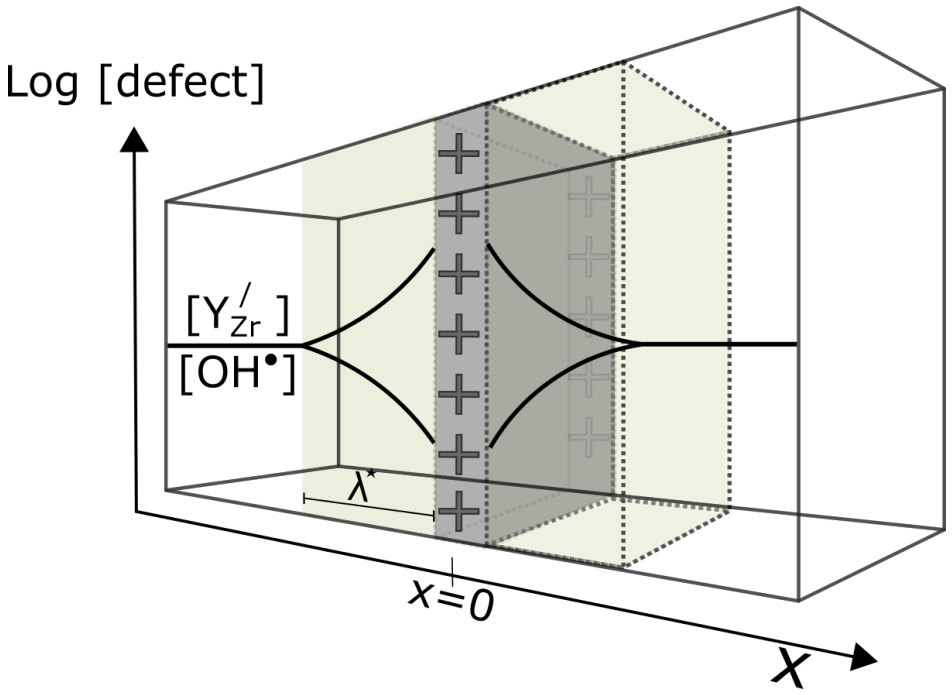

Figure 7.2: Schematic interpretation of the space-charge model, in which the dopant is not constant throughout the space-charge zone. The depleted specie is assumed to be dominated by protons.

7.3 Samples prepared with NiO additive

Results presented in section 6.3.3 demonstrated an increase in Ni at.% at the interfaces for both samples prepared with NiO. In the sample Ba-Ex the presence of secondary(s) were also observed.

Tong *et al.* studied the sintering mechanism behind SSRS on BZY20 with the addition of NiO [47]. From the precursor materials a peak emerges at around 785 °C belonging to the hexagonal $BaNiO_x$ ($2 < x < 3$). This peak is completely replaced by BaY_2NiO_5 at 900 °C, which is found in all XRD diffractograms between 900-1500 °C. Two defect mechanisms were proposed as possible diffusion processes of Ba, Y and Ni into the perovskite phase.

$$\frac{1}{3}BaY_2NiO_5 \xrightarrow{BaZr_{0.8}Y_{0.2}O_{3-\delta}} \frac{1}{3}Ba_{Ba}^{x} + \frac{2}{3}\nu_{Ba}'' + \frac{1}{3}Ni_{Zr}'' + \frac{2}{3}Y_{Zr}' + \frac{5}{3}O_{O}^{x} + \frac{4}{3}\nu_{O}^{\bullet\bullet} \tag{7.2}$$

$$\frac{1}{2}BaY_2NiO_5 \xrightarrow{BaZr_{0.8}Y_{0.2}O_{3-\delta}} \frac{1}{2}Ba_{Ba}^{x} + \frac{1}{2}\nu_{Ba}'' + \frac{1}{2}Ni_{i}^{\bullet\bullet} + Y_{Zr}' + \frac{5}{2}O_{O}^{x} + \frac{1}{2}\nu_{O}^{\bullet\bullet} \tag{7.3}$$

From the presented EDS results on the Ba-Deficent sample in figures 6.17c and d, one cannot determine whether Ni prefers the Zr- or and interstitial site. However, only the one wherein Ni occupies interstitial positions seem to be true according to more recent reports [89, 90]. First-principle calculations by Polfus *et al.* show that the Ni resides interstitially, and is more stable with increasing ν_{Ba}'' concentration as the association energy between ν_{Ba}'' and $Ni_i^{\bullet\bullet}$ is ~8.5 times more stable than between $Ni_i^{\bullet\bullet}$ and Y_{Zr}'.

Min Chen has studied the SSRS method and found the use of as little as 0.2 wt.% NiO is sufficient to promote densification and grain growth [94]. This is less than the 1 wt.% used here and it is perhaps not so strange that Ni rich phases were observed at the interfaces as shown in figure 6.18, as the solubility of Ni in BZY was estimated to be extremely small by CoorsTek [95]. The fact that the phases are present may be due to an equilibrium between the two phases and that further decomposition of BaY_2NiO_5 does not occur, in accordance with the sintering mechanism, proposed to be partial liquid-phase sintering by Tong *et al.* [47]. However, it is not clear whether the segregating phase is BaY_2NiO_5, variations of this phase or just simply metallic Ni due its low solubility in BZY.

In the Ba-deficient sample containing Ni, EDS showed that Ni was more present at grain boundaries and triple points, but the assumed charge compensating defect Y_{Zr}' did not

show any clear segregation behaviour. Actually, Y was found in higher ratios within the grains. Ba depletion was not readily observed either. A question unanswered is then: what is occurring in the space charge regions in these samples, as the grain boundaries are still assumed to be positively charged and thus still need to be charge compensated by some defect.

7.4 Further work

From the discussed topics it should be clear that a more fundamental study of grain boundaries, with defined orientation relationships in combination with functional properties, should be conducted. If the hypothesis that relationship between the orientation and segregation behaviour correlates, one should further find ways of preparation with some degree of preferential orientation relationship to overcome the high grain boundary resistance.
Some interesting experiments for TEM have been lifted throughout this study and are encouraged to be part of a further work.

7.4.1 Electron Energy Loss Spectroscopy (EELS)

EELS showed some interesting properties related to the O *K*-edge, as shown in Appendix D. A more thorough study of the O *K*-edge including calculations, in combination with the ratios of Ba *M*-edges as well as Y- and Zr edges, could be of interest.
Once one is able to distinguish all the futures in the EELS spectra one should further go into studying different types of grain boundaries either by finding these using EBSD in combination with Focused Ion Beam (FIB) or by preparing bicrystals with defined orientations and also subject them to heat/gasses.

7.4.2 Electron holography

Electron Holography in a TEM is a method to record both the amplitude and the phase of the complex electron wavefunction. Inside the sample, local magnetic- and electrostatic potentials result in a phase shift between two points $\mathbf{r}$ and $\mathbf{r}_0$. The relative phase shift purely due to an electrostatic potential may be written as:

$$\Delta\Phi(\mathbf{r}) = \Phi(\mathbf{r}) - \Phi(\mathbf{r}_0) = C(E) \int_z [U(\mathbf{r}) - U(\mathbf{r}_0)] dz. \tag{7.4}$$

where the integral is over the electron's path, i.e. the sample thickness *z*, and *C(E)* is the electron interaction constant given as:

$$C(E) = \frac{2\pi}{\lambda} \frac{m_0c^2 + E}{E(2m_0c^2 + E)}, \tag{7.5}$$

where *E* is the kinetic energy of the electrons.
After a reconstruction procedure one may thus obtain the electrostatic potential from distinct regions in the sample. This has been done for transistors before by Wang *et al.* [96], but also been applied to grain boundaries $SrTiO_3$ where one has been able to determine the Schottky potential at the interface [97–102].
Using holography on the grain boundaries in BZY may give insight into how the Schottky potential varies with different types of interfaces, sintering conditions and doping concentrations.

7.4.3 Enviromental TEM experiments

Based on the HR-STEM micrographs obtained in section 6.3.1, an experiment involving using ETEM/Temperature holder might enable the observation of hydration/dehydration of the material according to equation (2.23). Since the proton cannot be directly observed the change in oxygen intensity in the core and space-charge layers should be studied by both imaging and with EELS. Hydration could be performed by introducing H_2O or hydrogen rich gasses.
This experiment was attempted by the author, but unfortunately; a symmetric tilt boundary was not encountered on the experiment day.

Chapter 8

Conclusion

In this thesis the properties of BZY10, a material which has been studied and reported many times in literature, has been studied to gain more understanding of the factors limiting proton transport. Two main topics are investigated, addressing: 1) why the unconventional sample prepared by Sophie Duval do not show the same grain boundary resistivity as conventional samples, and 2) a study on the effect of NiO as sintering aid in the SSRS method.

Characterization of additive free samples

- Sample prepared in house exhibited grain boundary conductivity 3 orders of magnitude lower than that of bulk. The average grain size is ∼600 nm, which is what to be expected from this synthesis method.
- XRD indicated the presence of two phases in the same sample, with a Ba deficient A site.
  - This may be an indication of Y substituting A site, as the XPS analysis showed Y situated in two different chemical states.
- TEM-EDS indicated both segregation of Y and depletion of Ba at the grain boundaries in the conventional sample. Duval's sample only showed Y segregation.
  - The presence of ν''_{Ba} may be a factor preventing proton migration, since it is reported that this defect act as a strong proton trap; even stronger than Y'_{Zr}.
  - The above statement is in agreement with respect to the low conductivity values measured in this thesis (10^{-6} Scm^{-1} at 400 °C in wet O_2).

- The high temperature sample have grains grown significantly larger than what was observed for the samples prepared in this thesis. This may be a results of a recrystallization procedure which have been thermally activated by the high temperature treatment.
  - TEM indicated grain boundaries with corresponding grains orientation simultaneously close to the same ZA, indicating a possibly of higher frequency of near CSL type grain boundaries.
- The grain boundaries in both samples showed no presence of secondary- and amorphous phases.

Samples prepared with NiO as additive

- Sample prepared with Ba deficiency (Ba = 0.98) showed Ni dissolved within the BZY grains. The amounted of Ni is twice as high at grain boundaries and triple points, but no secondary phases were observed.
- Sample prepared with Ba excess (Ba = 1.02) precipitated Ni rich phases at the grain boundaries and triple points.
- The same degree of Y segregation to the interfaces was not observed in the Ni containing samples, as to the Ni free ones.

Many questions remain unanswered and a more fundamental understanding of grain boundaries in oxide ceramics materials is required. The thought that the grain boundary structure has a strong influence on the segregation, and thus the proton conductivity, have been lifted. tudying grain boundaries with defined structure, known segregation behaviour (EDS/EELS) while also knowing the Schottky Potential (holography), may give new insights into fundamental understandings of grain boundary related limiting factors. It may also provide opportunities to find pathways to resolve them, and as the final result: *develop new routes for optimizing BZY as a more effective proton-conducting electrolyte for electrochemical applications in the intermediate temperature range*.

List of References

1. U.S. Energy Information Administration. *Annual Energy Outlook* <http://www.eia.gov/forecasts/aeo/pdf/0383(2015).pdf> (2015).
2. International Energy Agency. *Tracking Clean Energy Progress* <http://www.iea.org/etp/tracking2015> (2015).
3. Duval, S. *Y-Substituted Barium Zirconate, a Proton Conducting Electrolyte for Applications at Intermediate Temperatures* PhD thesis (Technischen Universitat München, 2008).
4. Fabbri, E., Pergolesi, D. & Traversa, T. Materials challenges toward proton-conducting oxide fuel cells: a critical review. *Chemical Society Reviews* **39,** 4355–4369 (2010).
5. Norby, T. in *Perovskite Oxide for Solid Oxide Fuel Cells* (ed Ishihara, T.) (Springer US, 2009). ISBN: 9780387777085.
6. Norby, T. *Materials for Electrochemical Energy: Conversion and Storage* 2013.
7. Kreuer, K.-D. Proton-Conducting Oxides. *Annual Review of Materials Research* **33,** 333–359 (2003).
8. Iwahara, H., Esaka, T., Uchida, H. & Maeda, N. Proton conduction in sintered oxides and its application to steam electrolysis for hydrogen production. *Solid State Ionics* **3–4,** 359–363 (1981).
9. Norby, T. & Larring, Y. Concentration and transport of protons in oxides. *Current Opinion in Solid State and Materials Science* **2,** 593–599 (1997).
10. Duval, S., Holtappels, P., Vogt, U., Pomjakushina, E., Conder, K., Stimming, U. & Graule, T. Electrical conductivity of the proton conductor $BaZr_{0.9}Y_{0.1}O_{3-\delta}$ obtained by high temperature annealing. *Solid State Ionics* **178,** 1437–1441 (2007).

11. Momma, K. & Izumi, F. *VESTA3* for three-dimensional visualization of crystal, volumetric and morphology data. *Journal of Applied Crystallography* **44,** 1272–1276 (2011).

12. Giannici, F., Shirpour, M., Longo, A., Martorana, A., Merkle, R. & Maier, J. Long-Range and Short-Range Structure of Proton-Conducting Y:$BaZrO_3$. *Chemistry of Materials* **23,** 2994–3002 (2011).

13. Lejcek, P. *Grain Boundary Segregation in Metals* ISBN: 9783642125058 (Springer -Verlag Berlin Heidelberg, 2010).

14. Wolf, D. & Lutsko, J. F. On the geometrical relationship between tilt and twist grain-boundaries. *Zeitschrift für Kristallographie* **189,** 239–262 (1989).

15. Kronberg, M. L. & Wilson, F. H. Secondary recrystallization in copper. *Metals Transaction* **185,** 501–514 (1949).

16. Fultz, B. & Howe, J. M. *Transmission Electron Microscopy and Diffractometry of Materials* 4th ed. ISBN: 9783642297601 (Springer-Verlag Berlin Heidelberg, 2013).

17. Williams, D. & Carter, C. *Transmission Electron Microscopy: A Textbook for Materials Science* 2nd ed. ISBN: 9780387765006 (Springer US, 2009).

18. Norby, T. *Defect and Transport in Crystalline Solids* 2015.

19. Kröger, F. A. & Vink, H. J. Relations between the Concentrations of Imperfections in Crystalline Solids. *Solid State Physics* **3-4,** 307–435 (1956).

20. Yamazaki, Y., Yang, C.-K. Y. & Haile, S. M. Unraveling the defect chemistry and proton uptake of yttrium-doped barium zirconate. *Scripta Materialia* **65,** 102–107 (2011).

21. Azad, A., Savaniu, C., Tao, S., Duval, S., Holtappels, P., Ibberson, R. M. & Irvine, J. T. S. Structural origins of the differing grain conductivity values in $BaZr_{0.9}Y_{0.1}O_{2.95}$ and indication of novel approach to counter defect association. *J. Mater. Chem.* **18,** 3414–3418 (2008).

22. Magrez, A. & Schober, T. Preparation, sintering, and water incorporation of proton conducting $Ba_{0.99}Zr_{0.8}Y_{0.2}O_3$: comparison between three different synthesis techniques. *Solid State Ionics* **175,** 585–588 (2004).

23. Babilo, P., Uda, T. & Haile, S. Processing of yttrium-doped barium zirconate for high proton conductivity. *Journal of Materials Research* **22,** 1322–1330 (2007).

24. Kjølseth, C., Fjeld, H., Prytz, Ø., Dahl, P. I., Estournès, C., Haugsrud, R. & Norby, T. Space–charge theory applied to the grain boundary impedance of proton conducting $BaZr_{0.9}Y_{0.1}O_{3-\delta}$. *Solid State Ionics* **181,** 268–275 (2010).

25. Guo, X. & Waser, R. Electrical properties of the grain boundaries of oxygen ion conductors: Acceptor-doped zirconia and ceria. *Progress in Materials Science* **51,** 151–210 (2006).

26. De Souza, R. A. The formation of equilibrium space-charge zones at grain boundaries in the perovskite oxide $SrTiO_3$. *Phys. Chem. Chem. Phys.* **11,** 9939–9969 (2009).

27. Kim, S., Fleig, J. & Maier, J. Space charge conduction: Simple analytical solutions for ionic and mixed conductors and application to nanocrystalline ceria. *Phys. Chem. Chem. Phys.* **5,** 2268–2273 (2003).

28. Barsoukov, E. & Macdonald, J. R. *Impedance Spectroscopy* 2nd ed. ISBN: 0471647497 (John Wiley and Sons, Inc., 2005).

29. Haile, S. M., West, D. L. & Campbell, J. The role of microstructure and processing on the proton conducting properties of gadolinium-doped barium cerate. *Journal of Materials Research,* 1576–1595 (1998).

30. Kresse, G. & Furthmüller, J. Efficient iterative schemes for *ab initio* total-energy calculations using a plane-wave basis set. *Phys. Rev. B* **54,** 11169–11186 (1996).

31. Kresse, G. & Joubert, D. From ultrasoft pseudopotentials to the projector augmented-wave method. *Phys. Rev. B* **59,** 1758–1775 (1999).

32. Sholl, D. & Steckel, J. *Density Functional Theory: A Practical Introduction* ISBN: 9780470373170 (John Wiley & Sons, Inc., 2009).

33. Giustino, F. *Materials Modelling using Density Functional Theory: Properties and Predictions* ISBN: 9780199662449 (Oxford University Press, 2014).

34. Engel, E. & Dreizler, R. M. *Density Functional Theory: An advanced Course* ISBN: 9783642140907 (Springer Berlin Heidelberg, 2011).

35. Hohenberg, P. & Kohn, W. Inhomogeneous Electron Gas. *Phys. Rev.* **136,** B864–B871 (1964).

36. Kohn, W. & Sham, L. J. Self-Consistent Equations Including Exchange and Correlation Effects. *Phys. Rev.* **140,** A1133–A1138 (1965).

37. Perdew, J. P., Burke, K. & Ernzerhof, M. Generalized Gradient Approximation Made Simple. *Phys. Rev. Lett.* **77,** 3865–3868 (1996).

38. Haugsrud, R. & Norby, T. Proton conduction in rare-earth ortho-niobates and ortho-tantalates. *Nature Materials* **5,** 193–196 (2006).

39. Kawasaki, Y., Okada, S., Ito, N., Matsumoto, H. & Ishihara, T. Proton conduction and chemical stability of $(La_{0.5}Sr_{0.5})$ $(Mg_{0.5+y}Nb_{0.5-y})O_{3-\delta}$. *Materials Research Bulletin* **44,** 457–461 (2009).

40. Iwahara, H. in *Perovskite Oxide for Solid Oxide Fuel Cells* (ed Ishihara, T.) (Springer US, 2009). ISBN: 9780387777085.

41. Fabbri, E., Pergolesi, D., D Epifanio, A., Di Bartolomeo, E., Balestrino, G., Licoccia, S. & Traversa, E. Design and fabrication of a chemically-stable proton conductor bilayer electrolyte for intermediate temperature solid oxide fuel cells (IT-SOFCs). *Energy Environ. Sci.* **1** (2008).

42. Bi, L. & Traversa, E. Synthesis strategies for improving the performance of doped-$BaZrO_3$ materials in solid oxide fuel cell applications. *Journal of Materials Research* **29,** 1–15 (2014).

43. Katahira, K., Kohchi, Y., Shimura, T. & Iwahara, H. Protonic conduction in Zr-substituted $BaCeO_3$. *Solid State Ionics* **138,** 91–98 (2000).

44. Iguchi, F., Yamada, T., Sata, N., Tsurui, T. & Yugami, H. The influence of grain structures on the electrical conductivity of a $BaZr_{0.95}Y_{0.05}O_3$ proton conductor. *Solid State Ionics* **177,** 2381–2384 (2006).

45. Dahl, P., Lein, H. L., Yu, Y., Tolchard, J., Grande, T., Einarsrud, M.-A., Kjolseth, C., Norby, T. & Haugsrud, R. Microstructural characterization and electrical properties of spray pyrolyzed conventionally sintered or hot-pressed $BaZrO_3$ and $BaZr_{0.9}Y_{0.1}O_{3-\delta}$. *Solid State Ionics* **182,** 32–40 (2011).

46. Ricote, S., Bonanos, N., Manerbino, A. & Coors, W. G. Conductivity study of dense $BaCexZr_{0.9-x}Y_{0.1}O_{3-\delta}$ by solid state reactive sintering at 1500 °C. *International Journal of Hydrogen Energy* **37,** 7954–7961 (2012).

47. Tong, J., Clark, D., Bernau, L., Sanders, M. & O'Hayre, R. Solid-state reactive sintering mechanism for large-grained yttrium-doped barium zirconate proton conducting ceramics. *J. Mater. Chem.* **20,** 6333–6341 (30 2010).

48. Ricote, S., Bonanos, N., Manerbino, A., Sullivan, N. P. & Coors, W. G. Effects of the fabrication process on the grain-boundary resistance in $BaZr_{0.9}Y_{0.1}O_{3-\delta}$. *J. Mater. Chem. A* **2,** 16107–16115 (2014).

49. Malavasi, L., Fisher, C. A. J. & Islam, M. S. Oxide-ion and proton conducting electrolyte materials for clean energy applications: structural and mechanistic features. *Chem. Soc. Rev.* **39,** 4370–4387 (11 2010).

50. Duval, S., Holtappels, P., Stimming, U. & Graule, T. Effect of minor element addition on the electrical properties of $BaZr_{0.9}Y_{0.1}O_{3-\delta}$. *Solid State Ionics* **179,** 1112–1115 (2008).

51. Babilo, P. & Haile, S. M. Enhanced Sintering of Yttrium-Doped Barium Zirconate by Addition of ZnO. *Journal of the American Ceramic Society* **88,** 2362–2368 (2005).

52. Sun, Z., Fabbri, E., Bi, L. & Traversa, E. Lowering grain boundary resistance of $BaZr_{0.8}Y_{0.2}O_{3-\delta}$ with $LiNO_3$ sintering-aid improves proton conductivity for fuel cell operation. *Phys. Chem. Chem. Phys.* **13,** 7692–7700 (2011).

53. Guo, X. & Waser, R. Space charge concept for acceptor-doped zirconia and ceria and experimental evidences. *Solid State Ionics* **173,** 63–67 (2004).

54. Theunissen, G. S. A. M., Winnubst, A. J. A. & Burggraaf, A. J. Surface and grain boundary analysis of doped zirconia ceramics studied by AES and XPS. *Journal of Materials Science* **27,** 5057–5066 (1992).

55. Stemmer, S., Vleugels, J. & Biest, O. V. D. Grain boundary segregation in high-purity, yttria-stabilized tetragonal zirconia polycrystals (Y-TZP). *Journal of the European Ceramic Society* **18,** 1565–1570 (1998).

56. L. Gremillard, J. C. T. Epicier & Fantozzi, G. Microstructural study of silica-doped zirconia ceramics. *Acta Materialia* **48,** 4647–4652 (2000).

57. Matsui, K., Yoshida, H. & Ikuhara, Y. Grain-boundary structure and microstructure development mechanism in 2–8 mol yttria-stabilized zirconia polycrystals. *Acta Materialia* **56,** 1315–1325 (2008).

58. Iguchi, F., Tsurui, T., Sata, N., Nagao, Y. & Yugami, H. The relationship between chemical composition distributions and specific grain boundary conductivity in Y-doped BaZrO3 proton conductors. *Solid State Ionics* **180,** 563–568 (2009).

59. Iguchi, F., Sata, N., Tsurui, T. & Yugami, H. Microstructures and grain boundary conductivity of $BaZr_{1-x}Y_xO_3$ (x= 0.05, 0.10, 0.15) ceramics. *Solid State Ionics* **178,** 691–695 (2007).

60. Shirpour, M., Rahmati, B., Sigle, W., van Aken, P. A., Merkle, R. & Maier, J. Dopant Segregation and Space Charge Effects in Proton-Conducting $BaZrO_3$ Perovskites. *The Journal of Physical Chemistry C* **116,** 2453–2461 (2012).

61. Shirpour, M., Gregori, G., Houben, L., Merkle, R. & Maier, J. High spatially resolved cation concentration profile at the grain boundaries of Sc-doped BaZrO3. *Solid State Ionics* **262,** 860–864 (2014).

62. Sundell, P. G., Björketun, M. E. & Wahnström, G. Thermodynamics of doping and vacancy formation in $BaZrO_3$ perovskite oxide from density functional calculations. *Phys. Rev. B* **73,** 104112 (2006).

63. Björketun, M. E., Sundell, P. G. & Wahnström, G. Effect of acceptor dopants on the proton mobility in $BaZrO_3$: A density functional investigation. *Phys. Rev. B* **76,** 054307 (2007).

64. Sundell, P. G., Björketun, M. E. & Wahnström, G. Density-functional calculations of prefactors and activation energies for H diffusion in $BaZrO_3$. *Phys. Rev. B* **76,** 094301 (2007).

65. Helgee, E. E., Lindman, A. & Wahnström, G. Origin of Space Charge in Grain Boundaries of Proton-Conducting $BaZrO_3$. *Fuel Cells* **13,** 19–28 (2013).

66. Joakim Nyman, B., Helgee, E. E. & Wahnström, G. Oxygen vacancy segregation and space-charge effects in grain boundaries of dry and hydrated $BaZrO_3$. *Applied Physics Letters* **100** (2012).

67. Lindman, A., Helgee, E. E., Nyman, B. J. & Wahnström, G. Oxygen vacancy segregation in grain boundaries of $BaZrO_3$ using interatomic potentials. *Solid State Ionics* **230,** 27–31 (2013).

68. Lindman, A., Helgee, E. E. & Wahnström, G. Theoretical modeling of defect segregation and space-charge formation in the BaZrO3 (210)[001] tilt grain boundary. *Solid State Ionics* **252,** 121–125 (2013).

69. Polfus, J. M., Toyoura, K., Oba, F., Tanaka, I. & Haugsrud, R. Defect chemistry of a $BaZrO_3$ $\Sigma 3$ (111) grain boundary by first principles calculations and space-charge theory. *Phys. Chem. Chem. Phys.* **14,** 12339–12346 (2012).

70. Yang, J.-H., Kim, B.-K. & Kim, Y.-C. Calculation of proton conductivity at the tilt grain boundary of barium zirconate using density functional theory. *Solid State Ionics* **279,** 60–65 (2015).

71. Carcases, N. M. Unpublished work.

72. *Electron Backscatter Diffraction in Materials Science* (eds Schwartz, A. J., Kumar, M. & Adams, B. L.) ISBN: 030646487X (Kluwer Academic / Plenum Publisher, 2000).

73. Adams, B. L., Wright, S. I. & Kunze, K. Orientation imaging: The emergence of a new microscopy. *Metallurgical Transactions A* **24,** 819–831 (1993).

74. Meister, S. *Linecut: grain and particle analysis with the line intersection method* version 2.April 2012. <http://www.mathworks.com/matlabcentral/fileexchange/35203-grain-and-particle-analysis-with-line-intersection-method>.

75. MENDELSON, M. I. Average Grain Size in Polycrystalline Ceramics. *Journal of the American Ceramic Society* **52,** 443–446 (1969).

76. Olsen, A. *The Theory and Practice of Analytical Electron Microscopy in Material Science* (Dep. Physics, UiO, Norway, 2008).

77. NorECs AS. *ProboStat* <http://www.norecs.com/index.php?page=ProboStat> (2016).

78. Casa Software Ltd. *CasaXPS version 2.3.16* <http://www.casaxps.com> (2015).

79. Sven Tougaard. *QUASES-IMFP-TPP2M* <http://www.quases.com/products/quases-imfp-tpp2m> (2015).

80. Blöchl, P. E. Projector augmented-wave method. *Phys. Rev. B* **50,** 17953–17979 (1994).

81. Bjørheim, T. S., Løken, A. & Haugsrud, R. On the relationship between chemical expansion and hydration thermodynamics of proton conducting perovskites. *J. Mater. Chem. A* **4,** 5917–5924 (16 2016).

82. Mackenzie, J. K. Second Paper on Statistics Associated with the Random Disorientation of Cubes. *Biometrika* **45,** 229–240 (1958).

83. Mason, J. & Schuh, C. The generalized Mackenzie distribution: Disorientation angle distributions for arbitrary textures. *Acta Materialia* **57,** 4186–4197 (2009).

84. Structure and Composition of Grain Boundaries in Ceramics. *Journal of the European Ceramic Society* **19,** 665–673 (1999).

85. Jedvik, E., Lindman, A., Benediktsson, M. & Wahnström, G. Size and shape of oxygen vacancies and protons in acceptor-doped barium zirconate. *Solid State Ionics* **275.** 17th International Conference on Solid State Protonic Conductors, Seoul, Korea, 14-19 September 2014, 2–8 (2015).

86. Han, D., Kishida, K., Shinoda, K., Inui, H. & Uda, T. A comprehensive understanding of structure and site occupancy of Y in Y-doped $BaZrO_3$. *J. Mater. Chem. A* **1,** 3027–3033 (2013).

87. Spence, J. C. H. & Taftø, J. ALCHEMI: a new technique for locating atoms in small crystals. *Journal of Microscopy* **130,** 147–154 (1983).

88. Aruta, C., Han, C., Zhou, S., Cantoni, C., Yang, N., Tebano, A., Lee, T.-L., Schlueter, C. & Bongiorno, A. A-Site Cation Substitutions in Strained Y-Doped BaZrO3 Multilayer Films Leading to Fast Proton Transport Pathways. *The Journal of Physical Chemistry C* **120,** 8387–8391 (2016).

89. Polfus, J. M., Fontaine, M.-L., Thøgersen, A., Riktor, M., Norby, T. & Bredesen, R. Solubility of transition metal interstitials in proton conducting $BaZrO_3$ and similar perovskite oxides. *J. Mater. Chem. A* (2016).

90. Han, D., Shinoda, K., Tsukimoto, S., Takeuchi, H., Hiraiwa, C., Majima, M. & Uda, T. Origins of structural and electrochemical influence on Y-doped BaZrO3 heat-treated with NiO additive. *J. Mater. Chem. A* **2,** 12552–12560 (2014).

91. Doherty, R., Hughes, D., Humphreys, F., Jonas, J., Jensen, D., Kassner, M., King, W., McNelley, T., McQueen, H. & Rollett, A. Current issues in recrystallization: a review. *Materials Science and Engineering: A* **238,** 219–274 (1997).

92. Shih, S.-J., Dudeck, K., Choi, S.-Y., Baeurer, M., Hoffmann, M. & Cockayne, D. Studies of grain orientations and grain boundaries in polycrystalline $SrTiO_3$. *Journal of Physics: Conference Series* **94,** 012008 (2008).

93. Ernst, F., Mulvihill, M. L., Kienzle, O. & Rühle, M. Preferred Grain Orientation Relationships in Sintered Perovskite Ceramics. *Journal of the American Ceramic Society* **84,** 1885–1890 (2001).

94. Chen, M. Unpublished work.

95. Coors, W. & Menzer, S. Protonic ceramics of the solid solution $BaCe_{(x)}Zr_{(0.8-x)}Y_{0.2}O_{3-\delta}$ prepared by NiO-reactive sintering. Part I: fabrication and microstructure. *CoorsTek report* (2010).

96. Wang, Z., Hirayama, T., Sasaki, K., Saka, H. & Kato, N. Electron holographic characterization of electrostatic potential distributions in a transistor sample fabricated by focused ion beam. *Applied Physics Letters* **80,** 246–248 (2002).

97. Wang, Y. G. & Dravid, V. P. Determination of electrostatic characteristics at a 24°, [001] tilt grain boundary in a $SrTiO_3$ bicrystal by electron holography. *Philosophical Magazine Letters* **82,** 425–432 (2002).

98. Ravikumar, V., Rodrigues, R. P. & Dravid, V. P. Direct Imaging of Spatially Varying Potential and Charge across Internal Interfaces in Solids. *Phys. Rev. Lett.* **75,** 4063–4066 (1995).

99. Johnson, K. D. & Dravid, V. P. Static and Dynamic Electron Holography of Electrically Active Grain Boundaries in SrTiO3. *Interface Science* **8,** 189–198.

100. Ravikumar, V., Rodrigues, R. P. & Dravid, V. P. Space-Charge Distribution across Internal Interfaces in Electroceramics Using Electron Holography: I, Pristine Grain Boundaries. *Journal of the American Ceramic Society* **80,** 1117–1130 (1997).

101. Ravikumar, V., Rodrigues, R. P. & Dravid, V. P. Space-Charge Distribution across Internal Interfaces in Electroceramics Using Electron Holography: II, Doped Grain Boundaries. *Journal of the American Ceramic Society* **80,** 1131–1138 (1997).

102. Von Alfthan, S., Benedek, N. A., Chen, C. Lin, Chua, A., Cockayne, D., Dudeck, K. J., Elsässer, C., Finnis, M. W., Koch, C. T., Rahmati, B., Rühle, M., Shih, S.-J. & Sutton, A. P. The Structure of Grain Boundaries in Strontium Titanate: Theory, Simulation, and Electron Microscopy. *Annual Review of Materials Research* **40,** 557–599 (2010).

Appendix A

Brouwer diagrams

A.1 Defect concentration vs. pO_2

The starting point for the derivation is based on reaction A.1, with its corresponding equilibrium expression A.2. The minority defects equilibrium constants are given in equations A.3 to A.5, where the latter is due to the intrinsic ionisation of electrons.

$$O_O^x = \nu_O^{\bullet\bullet} + 2e' + \frac{1}{2}O_{2(g)} \tag{A.1}$$

$$K_{\nu_O^{\bullet\bullet}} = \frac{[\nu_O^{\bullet\bullet}]n^2 pO_2^{1/2}}{[O_O^x]} \tag{A.2}$$

$$K_{\nu_M'''} = \frac{[\nu_{Ba}''][\nu_{Zr}'''']h^6[O_O^x]^3}{pO_2^{3/2}} = \frac{[\nu_M''']^2 h^6[O_O^x]^3}{pO_2^{3/2}} \tag{A.3}$$

$$K_{hyd} = \frac{[OH_O^{\bullet}]^2}{[\nu_O^{\bullet\bullet}][O_O^x]pH_2O} \tag{A.4}$$

$$K_i = np \tag{A.5}$$

At low oxygen partial pressures, reaction A.1 is driven towards the product site. The dominated vacancies in this case is the oxygen vacancies and electrons, giving the simplified electroneutrality condition with its boundary conditions:
$p, [OH_O^{\bullet}] \ll 2[\nu_O^{\bullet\bullet}] = n \gg [Y_{Zr}']$. Concentration of metal vacancies are in this regime insignificant.
Solving equation A.1 yields the electron and oxygen vacancy concentration. Inserting the result into equations A.4 and A.5 yields the proton and hole concentration respec-

tively.

$$n = 2[\nu_O^{\bullet\bullet}] = (2K_{v_O^{\bullet\bullet}}[O_O^x])^{1/3} pO_2^{-1/6} \tag{A.6}$$

$$p = K_i(2K_{v_O^{\bullet\bullet}}[O_O^x])^{-1/3} pO_2^{1/6} \tag{A.7}$$

$$[OH_O^{\bullet}] = (\frac{1}{4}K_{v_O^{\bullet\bullet}}[O_O^x])^{1/6}(H_{hyd}[O_O^x]pH_2O)^{1/2} pO_2^{-1/12} \tag{A.8}$$

As pO_2 increases, we enter a new regime where $[Y'_{Zr}]$ is the dominating negative defect, and oxygen vacancies still the dominating positive. Metal vacancies are not contributing in this regime either, and the concentration of acceptor dopant is a fixed value. The electroneutrality condition along with the boundary conditions is now: $p, [OH_O^{\bullet}] \ll 2[\nu_O^{\bullet\bullet}] = [Y'_{Zr}] \gg n$. From the electroneutrality condition it is given that the concentration of oxygen vacancies is independent of pO_2 equation A.9. This is used to further solve for electrons, holes and proton concentration and the results are given below.

$$2[\nu_O^{\bullet\bullet}] = [Y'_{Zr}] \tag{A.9}$$

$$n = (2K_{v_O^{\bullet\bullet}}[O_O^x])^{1/2}[Y'_{Zr}]^{-1/2} pO_2^{-1/4} \tag{A.10}$$

$$p = K_i(2K_{v_O^{\bullet\bullet}}[O_O^x])^{-1/2}[Y'_{Zr}]^{1/2} pO_2^{1/4} \tag{A.11}$$

$$[OH_O^{\bullet}] = (K_{hyd}[O_O^x]pH_2O[Y'_{Zr}])^{1/2} \tag{A.12}$$

As pO_2 increases further, holes becomes the dominating negative compensating defect. In this region, metal vacancies also start to form. The electroneutrality condition along with the boundary conditions now becomes:
$[OH_O^{\bullet}], 2[\nu_O^{\bullet\bullet}] \ll p = [Y'_{Zr}] \gg 3[\nu'''_M], n$. Solving the equilibrium equations gives:

$$p = [Y'_{Zr}] \tag{A.13}$$

$$n = K_i[Y'_{Zr}]^{-1} \tag{A.14}$$

$$[\nu_O^{\bullet\bullet}] = K_{v_O^{\bullet\bullet}} K_i^{-2}[O_O^x][Y'_{Zr}]^2 pO_2^{-1/2} \tag{A.15}$$

$$[\nu_M^{'''}] = K_{\nu_M^{'''}}([Y'_{Zr}]^2[O_O^x])^{-3} pO_2^{3/2} \tag{A.16}$$

$$[OH_O^\bullet] = (K_{hyd}K_{v_O^{\bullet\bullet}})^{1/2}K_i^{-1}[O_O^x][Y'_{Zr}]pH_2O^{1/2}pO_2^{-1/4} \tag{A.17}$$

In the final region, the pO_2 value is so high that metal vacancies and holes becomes the dominating defects. The electroneutrality conditions and boundary conditions become: $[OH_O^\bullet], 2[\nu_O^{\bullet\bullet}] \ll p = 3[\nu_M'''] \gg [Y'_{Zr}], n$. Starting from equation A.3, we may find the pO_2 dependencies on the concentrations of the various defects as following:

$$p = 3[\nu_M'''] = (9K_{\nu_M'''}[O_O^x]^{-3})^{1/8}pO_2^{3/16} \tag{A.18}$$

$$n = K_i(9K_{\nu_M'''}[O_O^x]^{-3})^{-1/8}pO_2^{-3/16} \tag{A.19}$$

$$[\nu_O^{\bullet\bullet}] = K_{v_O^{\bullet\bullet}}[O_O^x]K_i^{-2}(9K_{\nu_M'''}[O_O^x]^{-3})^{1/4}pO_2^{-1/8} \tag{A.20}$$

$$[OH_O^\bullet] = (K_{hyd}K_{v_O^{\bullet\bullet}})^{1/2}K_i^{-1}[O_O^x](9K_{\nu_M'''}[O_O^x]^{-3})^{1/8}pH_2O^{1/2}pO_2^{-1/16} \tag{A.21}$$

The pO_2 dependencies are summarised in table A.1.

Table A.1: p_{O_2} dependencies for defects in Y doped $BaZrO_3$ under different electroneutrality conditions.

Electroneutrality Condition	p_{O_2}-dependencies for defects				
	$h^\bullet$	e'	$OH_O^\bullet$	$\nu_O^{\bullet\bullet}$	ν_M'''
$2[\nu_O^{\bullet\bullet}] = n$	$p_{O_2}^{1/6}$	$p_{O_2}^{-1/6}$	$p_{O_2}^{-1/12}$	$p_{O_2}^{-1/6}$	-
$2[\nu_O^{\bullet\bullet}] = [Y'_{Zr}]$	$p_{O_2}^{1/4}$	$p_{O_2}^{-1/4}$	Constant	Constant	-
$p = [Y'_{Zr}]$	Constant	Constant	$p_{O_2}^{-1/2}$	$p_{O_2}^{-1/4}$	$p_{O_2}^{3/2}$
$p = 3[\nu_M''']$	$p_{O_2}^{3/16}$	$p_{O_2}^{-3/16}$	$p_{O_2}^{-1/8}$	$p_{O_2}^{-1/16}$	$p_{O_2}^{3/16}$

A.2 Defect concentration vs $p\mathrm{H_2O}$

The concentration of defects will also vary with the pH_2O, and the basis for this derivation is equation A.24. Under low pO_2 and dry conditions the following electroneutrality condition and boundary condition apply:
$[OH_O^\bullet], p \ll 2[\nu_O^{\bullet\bullet}] = [Y'_{Zr}] \gg, n$. This gives the following dependency:

$$[OH_O^\bullet] = \frac{1}{4}\left(K_{hyd}[Y'_{Zr}][O_O^x]\right)^{1/2} p_{H_2O}^{1/2} \tag{A.22}$$

The concentration of the other defects remains constant as they are independent of pH_2O, and their solutions are given in the previous section A.1. As pH_2O increases, $OH_O^\bullet$ will eventually become the charge compensating defect, meaning: $[OH_O^\bullet] = [Y'_{Zr}]$. Solving the equations gives the following relations:

$$[v_O^{\bullet\bullet}] = (K_{hyd}[O_O^x])^{-1}[Y'_{Zr}]^2 p_{H_2O}^{-1} \tag{A.23}$$

$$n = (K_{hyd}K_{v_O^{\bullet\bullet}})^{1/2}[O_O^x][Y'_{Zr}]^{-1} p_{O_2}^{-1/4} p_{H_2O}^{1/2} \tag{A.24}$$

$$p = K_i(K_{hyd}K_{v_O^{\bullet\bullet}})^{-1/2}[O_O^x]^{-1}[Y'_{Zr}] p_{O_2}^{1/4} p_{H_2O}^{-1/2} \tag{A.25}$$

The pH_2O dependencies are summarised in table A.2.

Table A.2: p_{H_2O} dependencies for defects in Y doped $BaZrO_3$ under different electroneutrality conditions.

Electroneutrality Condition	p_{H_2O}-dependencies for defects			
	$h^\bullet$	e'	$OH_O^\bullet$	$\nu_O^{\bullet\bullet}$
$2[\nu_O^{\bullet\bullet}] = [Y'_{Zr}]$	Constant	Constant	$p_{H_2O}^{1/2}$	Constant
$[OH_O^\bullet] = [Y'_{Zr}]$	$p_{H_2O}^{-1/2}$	$p_{H_2O}^{1/2}$	$p_{H_2O}^{1}$	Constant

Appendix B

EDS quantification

The EDS analysis was performed using AZtecEnergy software by Oxford Instrument. Here a general EDS spectrum is presented before and after it has been peak fitted to quantify the desired peaks. It should be noted that the Y- and Zr *L*-edges are NOT used for quantification even though it is indicated here. The Cu peak originates from the Cu ring the sample is glued to, whilst the Fe and Au peak may be from the TEM chassie.

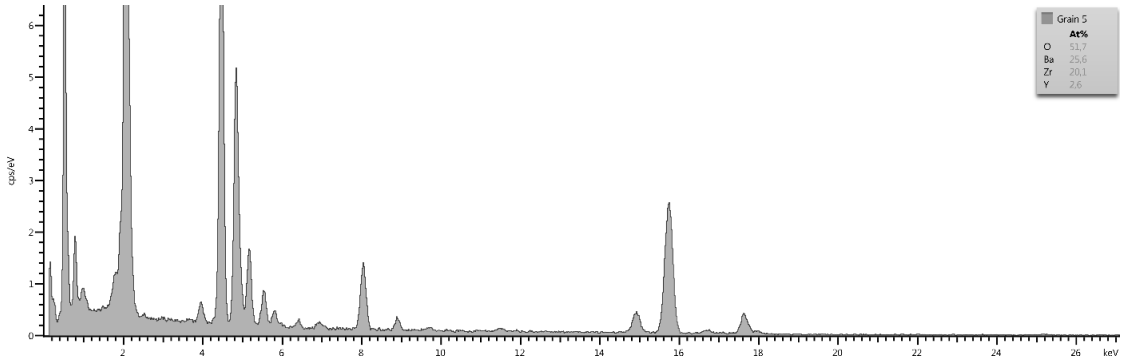

(a)

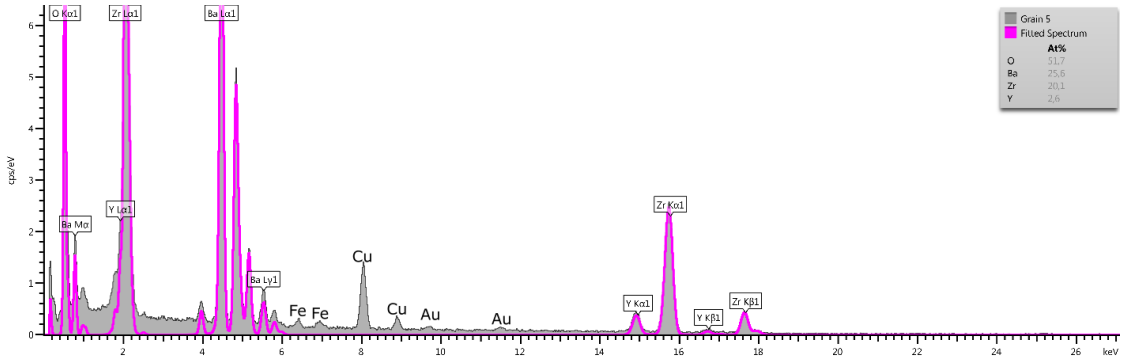

(b)

Figure B.1: Quantification of a general EDS peak. (a) is before peak identification and (b) is after fitting.

Appendix C

Rietveld refinement

Rietveld refinement was performed on the XRD diffractograms presented earlier. They were fitted using two cubic phases with space group $Pm\bar{3}m$. The Y and Zr sites was not allowed to refine since they are difficult to separate based on intensity. However, the Ba occupancy and the lattice parameter was allowed to be refined. This allowed the deconvolution of the spectrum, resulting in two phases with different lattice parameters. The phase with lower lattice parameter also has a broader peak, meaning that it perhaps also has a smaller extent than the other phase. The refined diffractogram is shown for BZY10-3-2 (where the broadening/splitting effect was most clear) in figure C.1.

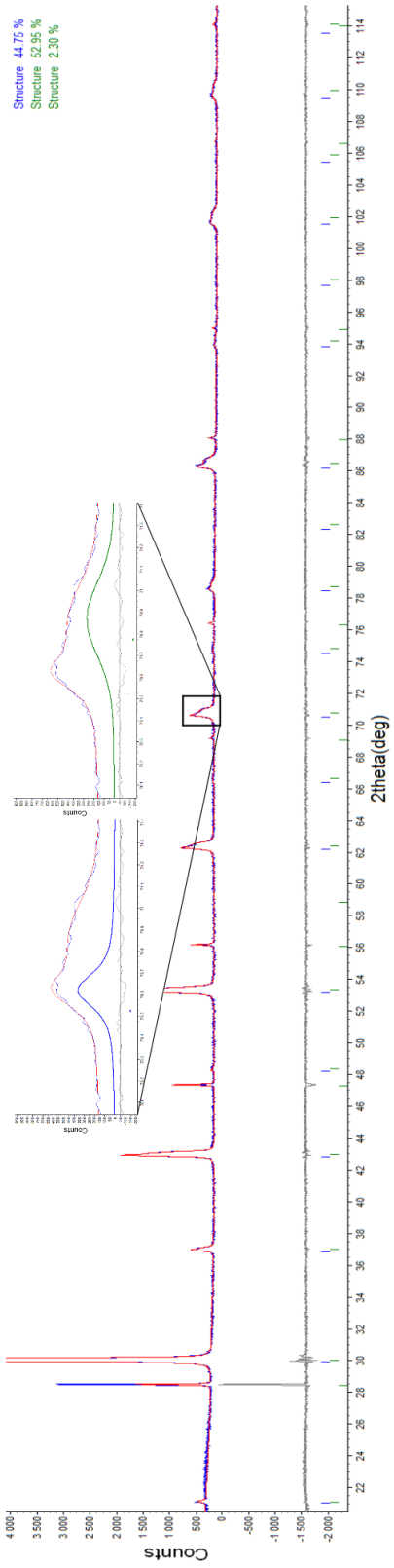

Figure C.1: Rietveld refinementfor sample BZY10-3-2. Structures with 44.75 and 52.95% corresponds to BZY cubic phases, and the last structure corresponds to Si standard (Nist 640D) which was used.

Appendix D

EELS spectra

EELS was performed over the $\Sigma 3$ grain boundary presented in chapter 6.3.1 and the results are reported here as it has not been thoroughly studied.
The low loss area consist of several overlapping peaks making it difficult to deconvolute and designate the ELNES areas to different peaks. Slicing the spectrum image at various distances from the grain boundary core only gives a change in the plasmon intensity i.e. thickness increases from left to right. The area labeled ”onset” in figure D.1 is a similar feature observed in a BaO standard by Gatan (Gatan, *BaO particles on holey C film*, 200 KeV, 0 - 180 eV, http://www.eels.info/atlas/barium, read: 19.04.16). Its physical meaning is not clear.
The core loss area shows the O-K and Ba-M edges. If the futures in the O-K edge only are found in the grain boundary was an initial thought, however scanning further away from a grain boundary revealed similar features.

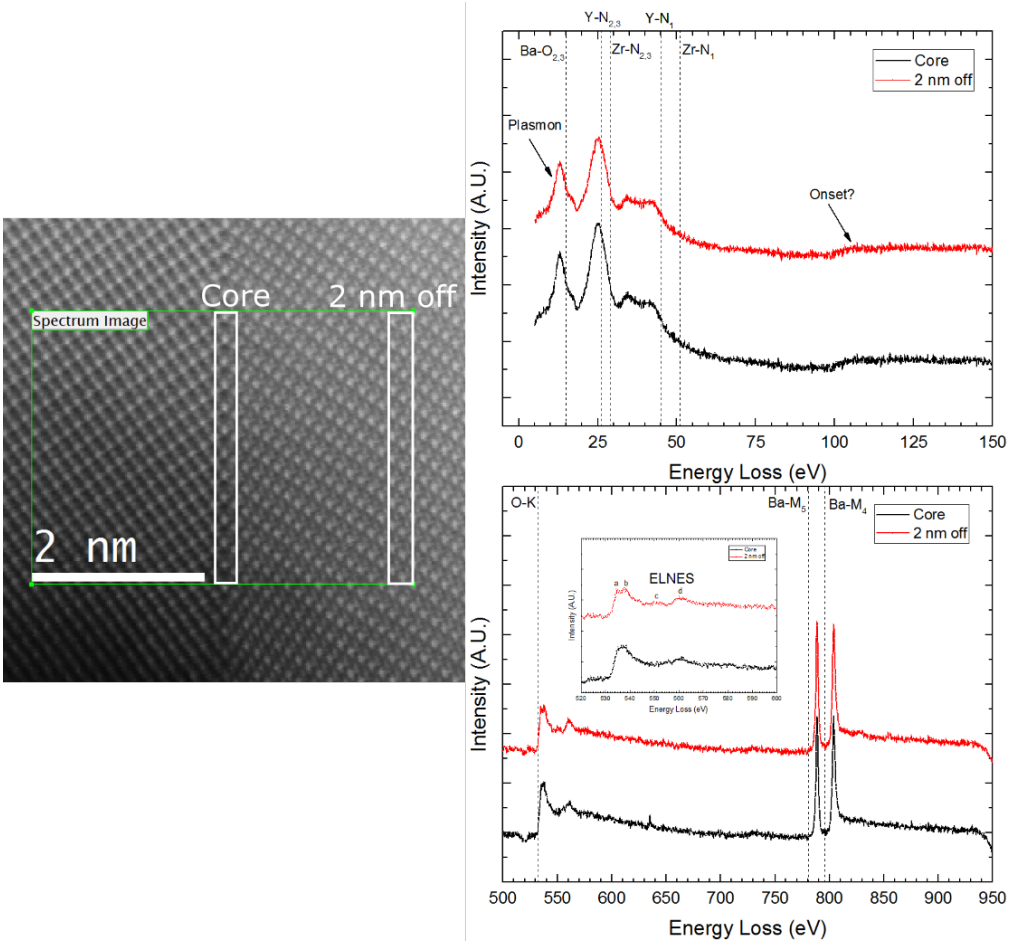

Figure D.1: Overview micrograph and stacked low- and core loss spectrums, normalized by the background area and offsetted.

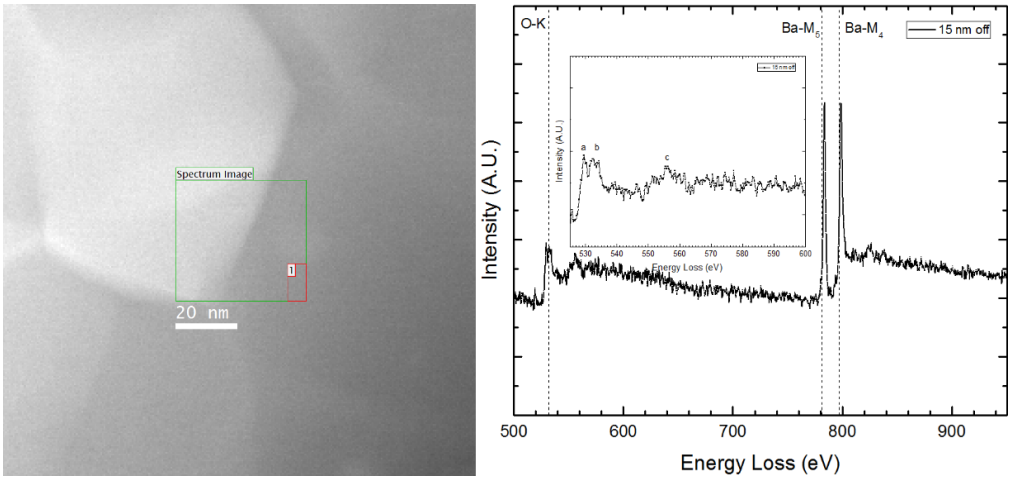

Figure D.2: Overview micrograph and core loss spectrum corresponding to area marked 1.

Appendix E

Initial impedance results

The initial measurements were deconvoluted with three (RQ) circuit in series describing the bulk, grain boundary and electrode contribution as described in section 2.6. A difficulty with this dataset is that the bulk semicircle is not observable as seen in E.1b. This makes obtaining accurate values for the capacitances required to report the specific GB conductivity, impossible. The resistance may, however, be estimated and this is what has been done to report the uncorrected conductivities in wet air in figure E.1a.

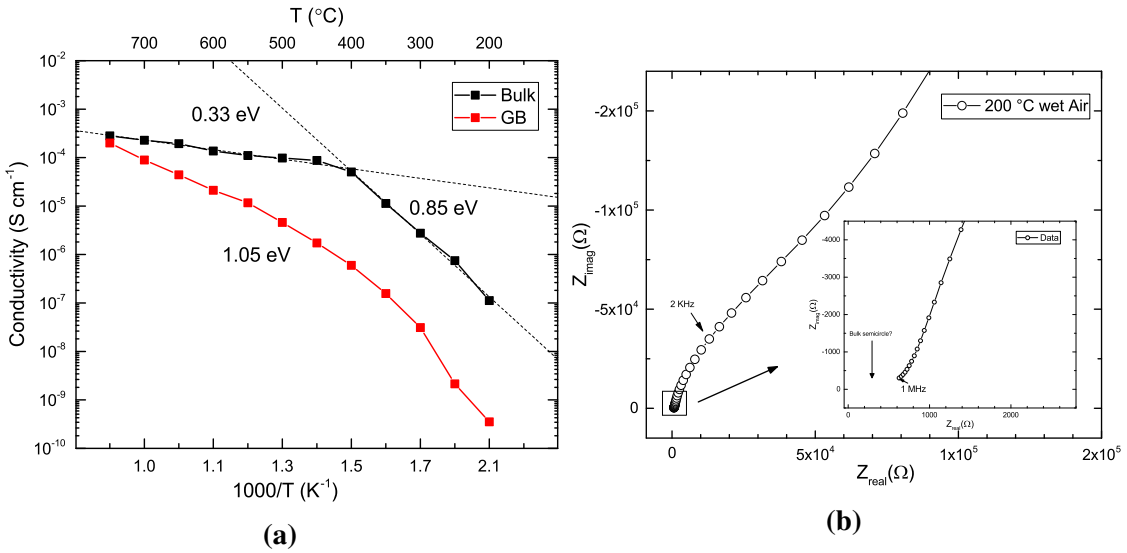

Figure E.1: Bulk and GB conductivity vs. temperature in wet air in (a). The activation energy determined from Arrhenius interpolation, is also indicated. (b) shows the raw impedance spectrum at 200 °C.

The bulk conductivity fits somewhat into litterature the abrupt change in conductivity at ∼450 °C has to the author's knowledge never been observed. The bulk acitvation

energy of 0.85 eV is twice the reported values, and the other value $\sim$0.4 eV lower. The grain boundary activity is no far of from literature, but the magnitude of the conductivity here is not correct as it has not been corrected for the capacitances. To verify if this is a material property, or if it is an artefact due to the instrument or deconvolution procedure, a new set of measurements with another test interface were conducted.